EXPLORING TRANSPORT AND PHASE BEHAVIOR IN NANOPOROUS CARBON MATERIALS

by

STEVEN SHIMIZU

B.S., UC San Diego (2009)

Submitted to the Department of Chemical Engineering

in Partial Fulfillment of the Requirements for the Degree of

Doctor of Philosophy in Chemical Engineering

at the

MASSACHUSETTS INSTITUTE OF TECHNOLOGY

June 2015

Signature redacted

Author.....

Department of Chemical Engineering
February 11, 2015

Signature redacted

Certified by.....

Michael S. Strano
Carbon P. Dubbs Professor of Chemical Engineering
Thesis Supervisor

Signature redacted

Accepted by... .....

Richard D. Braatz
Edwin R. Gilliland Professor of Chemical Engineering
Chairman, Committee for Graduate Students

EXPLORING TRANSPORT AND PHASE BEHAVIOR IN NANOPOROUS CARBON MATERIALS

by

STEVEN SHIMIZU

Submitted to the Department of Chemical Engineering

in Partial Fulfillment of the Requirements for the Degree of

Doctor of Philosophy in Chemical Engineering

ABSTRACT

Understanding transport and phase behavior in nanopores has a substantial impact on applications involving membrane fabrication, single-molecule detection, oil reservoir modeling, and drug delivery. While transport and phase behavior in larger nanopores (>50 nm) approach bulk or are well-described by continuum models, much less is known about much smaller nanopores where the diameter of the pore is on the order of the molecular size of the internal fluid.

This thesis provides experimental insight into the diameter dependence of ionic transport and fluid phase transitions inside carbon nanotube (CNT) nanopores (1-2 nm). For substances confined inside slightly larger pore sizes (roughly 4-25 nm in diameter), methods are presented for predicting the diameter-dependent freezing point changes. This work also demonstrates the use of patch clamp for generating and studying soft polymer-based nanopores.

Thesis Supervisor: Michael S. Strano

Title: Professor of Chemical Engineering

Acknowledgements

First and foremost, I would like to thank my advisor, Professor Michael Strano, for his vision and guidance during my research and teaching me how to be a better scientist. I would also like to thank Professor Martin Bazant, Professor Narendra Maheshri, and Professor Evelyn Wang for their valuable advice while serving on my thesis committee. Throughout my research, I have been fortunate to have been provided funding and access to facilities by the MIT Energy Initiative Fellows Program, the U.S. Army Research Office through the Institute of Soldier Nanotechnologies, MIT Microsystems Technology Laboratories, Siemens, DuPont, BP, and Shell.

Day-to-day research would not have been possible without the camaraderie and assistance of my fellow lab members, undergraduates, collaborators, and friends. I will always cherish our times together.

I want to express gratitude to my family for their care, support, and for raising me to become the person I am today. And finally, I would like to thank my loving wife, Jen, for being so supportive and encouraging during the good and bad times—I couldn't have done it without you.

Table of Contents

1. Overview

The objective of this thesis is to describe and understand processes of transport and phase behavior in nanomaterials, especially carbon nanotubes. Transport in nanopores is of tremendous interest for desalination and single-molecule detection. Chapter 2 describes the fabrication and testing of devices containing an individual single-walled carbon nanotube (SWNT) of a very specific diameter. Previous experiments demonstrated the mechanism of pore-blocking in pores, whereby an ion blocks an otherwise stable proton current through the pore. Carrying out these same experiments with well-characterized diameters allowed us to show a highly non-monotonic trend of pore-blocking currents with diameter.

While single-SWNT devices are very interesting, they are also difficult to prepare. In order to study nanopore transport more easily, a patch clamp setup was built and used to patch a small micropipette onto a grooved PDMS surface, which is described in Chapter 3. The grooves and the surface of the pipette tip were sized to form two nanochannels whose size could be controlled by the amount of force exerted on the micropipette. Significantly, stochastic changes in conductance of the pore were observed, but these were dissimilar to that of the SWNT stochastic pore-blocking, as the "blocker" appears to be uncharged. We attribute this behavior to ionic vapor-liquid phase transitions occurring inside the pore.

Having observed potential deviations in phase behavior from the bulk, we set out to directly study the phase of fluids confined inside more well-defined nanopores. There have not been many experimental studies on the phase behavior of fluids inside small nanopores, yet there are direct applications in oil and gas recovery and drug delivery using nanocontainers. In very small nanopores (<2 nm), it has been predicted that freezing points are strong, non-monotonic functions of pore diameter. Chapter 4 discusses the development of a new method for spectroscopically probing phase transitions inside of individual carbon nanotubes. Raman spectroscopy can probe the vibrational modes of carbon nanotubes, and this makes it an indirect probe for filling and phase transitions inside of the tube. Evidence of temperature-induced phase transitions of water inside a single, well-defined carbon nanotube is clearly observed.

Above about 4 nm, the freezing points of fluids inside nanopores appear to follow the Gibbs-Thomson equation, which predicts freezing point depressions to be linearly related to the inverse pore radius, with the slope being a function of fusion enthalpy and solid-liquid surface energy. Chapter 5 discusses methods of predicting the freezing point depression of a fluid inside of a nanopore of a given size, which is complicated by the fact that fusion enthalpy and surface energy are also very size-dependent for pore sizes <25 nm.

In summary, this thesis is a theoretical and experimental investigation into interior transport and phase behavior inside of carbon nanotubes and other nanoporous materials. The fundamental insights gained will be important in membrane development, single molecule detection, nanopore modeling, and drug delivery.

2. Introduction

The transport and phase behavior of fluids inside of nanopores is a topic of tremendous interest due to the implications regarding efficient membranes, oil and gas recovery, nanoreactors and nano-delivery of molecules. Figure 1 illustrates the significant, growing interest in the study of nanopores over the past 15 years. There is a large diversity in the types of nanopores studied, including biological, solid-state, and carbon-based nanopores. While any pore < 1 μm in diameter is technically called a nanopore, very different physical behavior is observed across that diameter range.

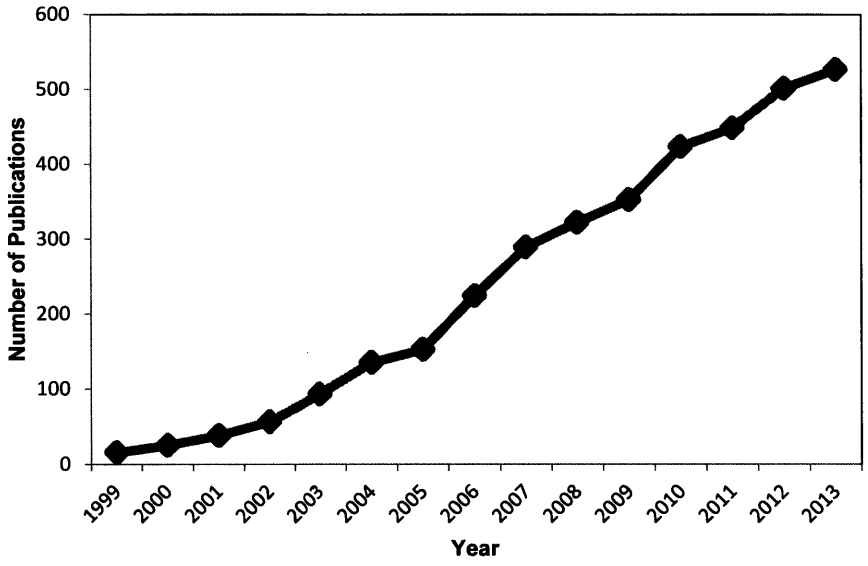

Figure 1. Number of publications each year with 'nanopore' as a keyword.

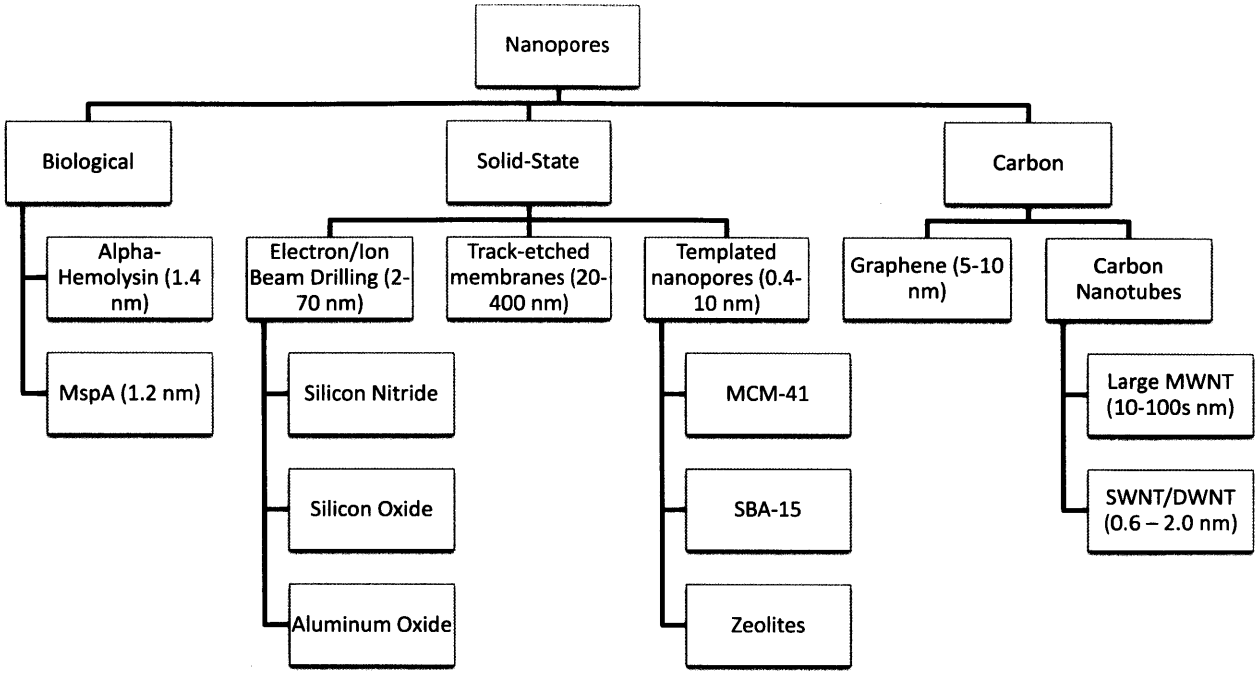

Figure 2. A diagram showing the major areas of nanopore research.

2.1 Overview of Nanoporous Materials

Biological nanopores, specifically alpha-hemolysin and MspA protein pores, have been studied extensively in an attempt to sequence the base pairs of DNA.[1] Because of their biological origin, these pores have a specific diameter (1.4 nm for alpha-hemolysin and 1.2 nm for MspA) that is consistently reproducible.[2-3] Genetic modifications can even be introduced to improve performance and change the chemical groups of the inner pore region.[4] Measurement of current through single pore channels can be monitored by embedding a single pore in a lipid bilayer and applying a voltage across the layer. The extent of deviations in the baseline current as molecules pass through and block an otherwise stable ion current can provide an indication to the identity of the molecule.

Solid-state nanopores can be divided into the following categories: single nanopores prepared through electron or ion-beam sculpting, track-etched polymer membranes, and templated, silica-based nanopores. For electron or ion-beam sculpting, a cavity or larger hole is initially prepared in a

thin membrane of Si_3N_4 or SiO_2, typically, and an electron or ion-beam is used to decrease the size of the opening to just several nanometers in size. The beam induces flow of the membrane material, which shrinks the existing hole due to surface tension effects.[5-6] By varying the irradiation level and time of exposure, the pore size can be fine-tuned between 2 to 70 nm. Similar to biological nanopores, there have been significant efforts in using these pores for DNA sequencing.

While these beam-sculpted nanopores can make precise, single nanopores, track-etched membranes can potentially have up to a billion pores per cm^2. Track-etched membranes are prepared by exposing a polymer membrane to high energy ions which create cylindrical tracks through the membrane. Further etching can open up the pores to be anywhere above 10-20 nm.[7] Studies of these pores have shown tunable ion rectification dependent on pore shape and pore wall chemistry.[8] Biosensors have been made by bio-functionalizing the inner pore walls which attach to specific analytes and subsequently block ionic current.[9]

While templated nanoporous materials like MCM-41, SBA-15 and zeolites also have many nanopores, they differ by being micron-sized particles (as opposed to a flat membrane material) composed of small nanopores between 0.4 – 10 nm in diameter. Materials like MCM-41 are formed by using surfactant micelles of a specific size as templates for amorphous silica; subsequent calcination removes the surfactant and leaves well-defined pores.[10] Zeolites, while not all are synthesized using a templating method, form crystalline structures with very small nanopores (typically < 1 nm).[11] These materials have been studied as molecular sieves and as systems for controlled drug delivery.[12]

The recent discoveries of graphene and carbon nanotubes have sparked interest in using these materials as nanopores. Graphene is a conductive, atomically-thin (0.3 nm), single sheet of carbon made by exfoliation technique or chemical vapor deposition.[13] Nanopores can be formed in the graphene sheet by drilling with a TEM electron beam. Graphene has been explored as a better alternative to Si_3N_4 or SiO_2 nanopores; these solid-state nanopores are ~30 nm thick (~100 base pairs) which reduce the ability to distinguish individual DNA base pairs that move through the pores. Being atomically thin, a graphene pore has the potential to have much higher base pair resolution.[14] Since graphene is also conductive, simultaneous measurement of the transverse electrical current can also aid in single-molecule detection through the pore.[15]

Finally, carbon nanotube nanopores are unique in that they can form constant diameter (0.6 nm to 100s of nm), straight-line pores, with lengths ranging from a couple hundred nanometers to centimeters. Besides their interesting nanopore qualities, CNTs have exceptional mechanical and electrical properties, and they can be grown as single-, double-, or multi-walled tubes. Unlike other pore materials described, the interior of CNTs are atomically smooth and have been shown experimentally to have enhanced viscous flow due to slip at the pore walls.[16-17] Because CNTs are made of carbon, end-group functionalization is relatively straightforward and can be used to impart ion rectification and molecular detection.[18] CNTs can be grown on a substrate as individual nanopores[19] or as large arrays of aligned nanotubes in which the interstitial volume can be filled in to create a membrane.[16-17] These systems have been studied both experimentally and theoretically for applications in desalination membranes, single molecule detection, and drug delivery.

2.2 Nanopore Transport Overview

2.2.1 Viscous Flow

In continuum fluid mechanics, pressure-driven Poiseuille flow through a pore assumes no-slip at the pore walls, meaning that the fluid has zero velocity at the pore walls. One argument for the no-slip condition, which is generally observed experimentally, is that surface roughness and the resulting viscous dissipation causes the fluid to essentially be at rest. Zhu and Granick experimentally verified that a surface roughness of 6 nm rms was sufficient for the no-slip condition to hold.[20] Thus, as a pore becomes smaller and surface roughness decreases, significant flow enhancement can occur. Carbon nanotubes, which have an atomically smooth surface, have experimentally exhibited large hydrodynamic flow enhancements attributed to the slip at the pore walls.[16] This interesting property has stimulated work on using carbon nanotube nanopores for desalination membranes[18, 21] and for studying enhanced permeabilities in geological media.[22]

2.2.2 Ion Conductivity

The conductivity of a channel containing ions can typically be calculated using bulk ion concentrations and conductivities. However, if the channel walls are charged, there is an electrical double layer that forms at the interface consisting mostly of oppositely-charged ions. The characteristic thickness of the electrical double layer is the Debye length; for a 0.1M 1:1 electrolyte in water at room temperature, this thickness is 0.96 nm. Thus, for large channels with low surface-to-volume ratio, this double-layer may have negligible effect on overall channel conduction. However, as the channel decreases in size, the surface term for ion conduction begins to predominate in nanopores.

At even smaller pore diameters, the conductivity of ions is heavily dependent on the structure of water inside the pore. For example, MD simulations have shown one-dimensional water alignment inside carbon nanotubes which enhances proton transport through the nanotube compared to bulk.[23]

2.2.3 The Coulter Effect

The Coulter Effect is a phenomenon discovered by Wallace Coulter in 1949 that occurs when a particle causes a change in impedance when passing through an opening carrying a stable ion current.[24] Figure 3 illustrates the effect of a charged particle moving through an opening of a similar size. The ionic current through the opening shows a sudden decrease when the particle passes through. This effect has been utilized for single-molecule or single-particle detection in pores of nanometer to millimeter-sized diameters. Nanoparticle sizing and counting has been demonstrated for single MWNT Coulter counters (132 nm diameter),[25] as well as other larger nanopore systems. At even smaller diameters (<2 nm), the Coulter effect can even be used to distinguish between individual molecules. For example, different nucleotides passing through an α-hemolysin pore block ion current to significantly different extents.[4]

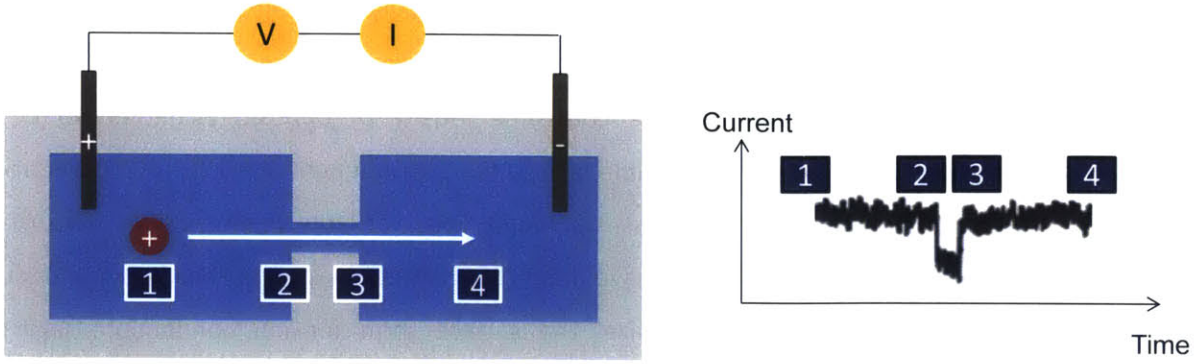

Figure 3. Diagram of the Coulter Effect. As a larger, charged particle passes through an orifice, there is a change in impedance of the pore, manifested through a drop in current. The magnitude of the current drop is proportional to the volume of the blocking particle.

2.3 Nanopore Phase Behavior Overview

For a bulk material, the thermodynamic state of a fluid has two degrees of freedom (e.g. temperature and pressure). Furthermore, if it is known that the bulk fluid is at a phase transition, then there is only a single degree of freedom. For example, bulk water at its freezing point requires knowledge of only a single intensive parameter, such as temperature, and this specifies all other intensive thermodynamic variables.

For fluid confined inside a nanopore, more than two degrees of freedom may be required to specify the state of the system due to the fluid-wall interactions. For example, Mansoori and co-workers reported an analytic model showing that the thermodynamic state of a fluid confined to a constant-diameter nanopore was dependent on three degrees of freedom: temperature (T), molar volume (v) and a parameter accounting for fluid-wall effects (y).[26] Experimentally as well, confinement has shown to dramatically affect the phase transition of fluids inside of nanopores, with the phase transition likely dependent on pore material, pore shape and pore diameter.[27]

Knowledge of how nanopore confinement affects the thermodynamic state of fluids will have significant application in the fields of oil and gas recovery from nanoporous geological media,[28] delivery and storage of materials inside nanopores,[29] and phase change materials[30].

2.4 Outline of Thesis

This thesis focuses on fundamental studies of transport and phase behavior in individual nanopores between 1.0 and 25 nm. The following questions regarding the study of nanopores have been addressed in this thesis:

- What is influence of diameter on proton transport inside single-walled carbon nanotube nanopores (1-2 nm)?
- Many nanopore systems require significant fabrication efforts. Can nanopores be easily generated and studied?
- How does the phase behavior of fluids change when confined inside carbon nanotube nanopores (1-2 nm), and how can filling and phase transitions be measured?
- How can one predict freezing points in larger nanopores >4 nm in diameter?

In Chapter 3, we study the dependence of carbon nanotube diameter on proton transport. Raman spectroscopy is used to precisely determine carbon nanotube diameters, and devices are constructed containing a single, isolated carbon nanotube. Subsequent voltage clamp measurements on single, characterized nanotube devices show stochastic blocking of current through the nanotube, which is attributed to single ions blocking the otherwise stable proton current. Twenty individual nanotubes are studied to give the diameter-dependent trend of blockade currents which reveal a maximum around 1.6 nm. This result demonstrates the need for producing or synthesizing nanotubes of the same chirality, as even sub-Angstrom changes in diameter have a disproportionate effect on transport properties.

While these individual nanotube studies are very informative, the device fabrication process is labor-intensive. Similarly, studying any single nanopore (e.g. electron-beam sculpted solid-state nanopores) is difficult from a fabrication standpoint and requires cleanroom and TEM facilities. Chapter 4 discusses the use of patch clamp to study nanopore transport in a novel way. Typically, patch clamp uses a small glass micropipette to patch onto a cell membrane and study stochastic gate switching of ion channels. Here, instead, the glass micropipette is simply patched to the surface of a nano-grooved PDMS layer, resulting in the formation of 2 nanopores with tunable diameter (1-

15 nm). Stochastic current fluctuations are attributed to ionic vapor-liquid phase transitions that have been predicted in literature.

Given that ionic phase transitions were indirectly observed in these hydrophobic PDMS nanopores, which do not exist in bulk at room temperature, there is the possibility of significant departures of the phase transition from bulk behavior for fluids confined inside nanopores. While phase transition measurements have been performed on bulk quantities of nanopores, there have been no experiments measuring phase transitions inside a single nanopore of a well-defined diameter. Chapter 5 describes the novel application of Raman spectroscopy to probe interior water filling states (vapor, liquid and solid) in single- and double-walled carbon nanotubes of varying diameters. Discrete shifts in the radial breathing modes (vibrational modes of the carbon atoms) are correlated with filling and phase transitions, and dramatic shifts in freezing points are observed. Furthermore, the effects of laser heating on the local tube temperature are quantified.

From the Raman phase transition experiments, it is clear that the confinement effect on the temperature of phase transitions is highly non-linear and non-monotonic, owing to the significant effect the pore walls have on the structure and energy of the fluid below 2 nm. Bulk thermodynamics, however, predicts that the freezing point change varies as $1/r_{pore}$ according to the Gibbs-Thomson relationship. Typically, this Gibbs-Thomson relationship assumes a constant ΔH_f of the fluid confined inside the pore despite being significantly diameter-dependent for small nanopores (4-25 nm diameter). Chapter 6 explores this intermediate nanopore diameter regime and provides an empirical model for predicting freezing points of pure substances confined to intermediate-sized nanopores.

3. Ion Transport Through Single Carbon Nanotube Nanopores of Specific Diameters

3.1 Introduction

The study of nanopore transport is of tremendous interest. Specifically, we are interested in the model pores formed by single-walled carbon nanotubes, which one can think of as a single, 2D sheet of carbon atoms (graphene) rolled up into a cylinder, forming an atomically-smooth nanopore that is typically 0.7-2 nm in diameter. In the literature, these nanotube nanopores have been studied for their unique transport properties, including high rates of pressure-driven flow due to increased slip length at the smooth pore walls,[16-17, 31] selectivity due to end-group functionalization,[18, 32] and enhanced proton transport through the tube due to more favorable proton-hopping mechanism.[19, 23, 33-34] Potential applications lie in the fields of desalination membranes, chemical separations, and molecular recognition sensors.

Our own group has previously discovered the phenomenon of stochastic pore-blocking, where cations block an otherwise stable proton current inside carbon nanotubes.[19, 34] In these previous studies, arrays of horizontally-aligned nanotubes (around 10-40) were grown on silicon, and reservoirs were placed over the nanotubes. Subsequent plasma etching removed the ends of the nanotubes up to the barrier, leaving a small number of opened carbon nanotubes spanning the barrier. Upon filling the reservoirs with an electrolyte solution, voltage clamp measurements were performed whereupon a constant voltage is applied across the reservoirs while monitoring the instantaneous current required to maintain that voltage. An example current trace indicating the relevant properties is depicted in Figure 4.

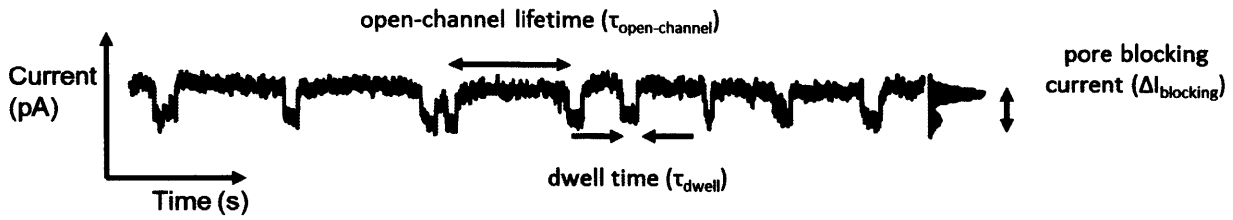

Figure 4. Example voltage clamp trace showing stochastic changes in current through the nanotube as a function of time. The pore-blocking current is the magnitude of the current change, the dwell time is the time residing in the blocked state (lower current), and the open-channel lifetime is the time between blocked states.

These initial studies, however, were unable to measure the exact diameter of nanopore that was accounting for these stochastic changes in current due to the fact that many nanotubes of different diameters were present in the device. However, the literature has predicted a wide range of behavior inside of tubes depending on their diameters,[35] so it is of fundamental importance to understand the effect diameter plays in transport through these pores.

3.2 Experimental

In order to probe transport through a single, isolated SWNT, we developed a new fabrication procedure as described in Figure 5. Raman spectroscopy is a technique that detects the inelastic scattering of monochromatic incident light, with the Raman spectrum plotting the intensity of the inelastically-scattered light versus the change in frequency from the incident light. Peaks in this spectrum correspond to Raman-active vibrational modes of the molecule. Normally, Raman signals are very weak, but because of singularities in the density of states for carbon nanotubes, one can actually observe an intense Raman signal from a single carbon nanotube if the incident light energy coincides with the electronic transition between these singularities, known as resonance Raman spectroscopy.[36] Peak positions and shapes can be used to determine nanotube diameter and metallicity, as depicted in Figure 6.

In order to locate individual single-walled carbon nanotubes (SWNT), optically-observable markers were placed on the substrate and imaged in a scanning electron microscope (SEM), which can be

used to image carbon nanotubes. SEM measurements were performed on a JEOL 6060 SEM at 1.2 kV accelerating voltage and 100x magnification. The relative distance between the marker and SWNT were used to locate the SWNT in the Raman's optical microscope. A 633nm laser excitation source was predominantly used to identify the SWNT, although a 532nm laser excitation source was used in some cases. The choice of laser wavelength does not affect the peak positions of the RBMs.

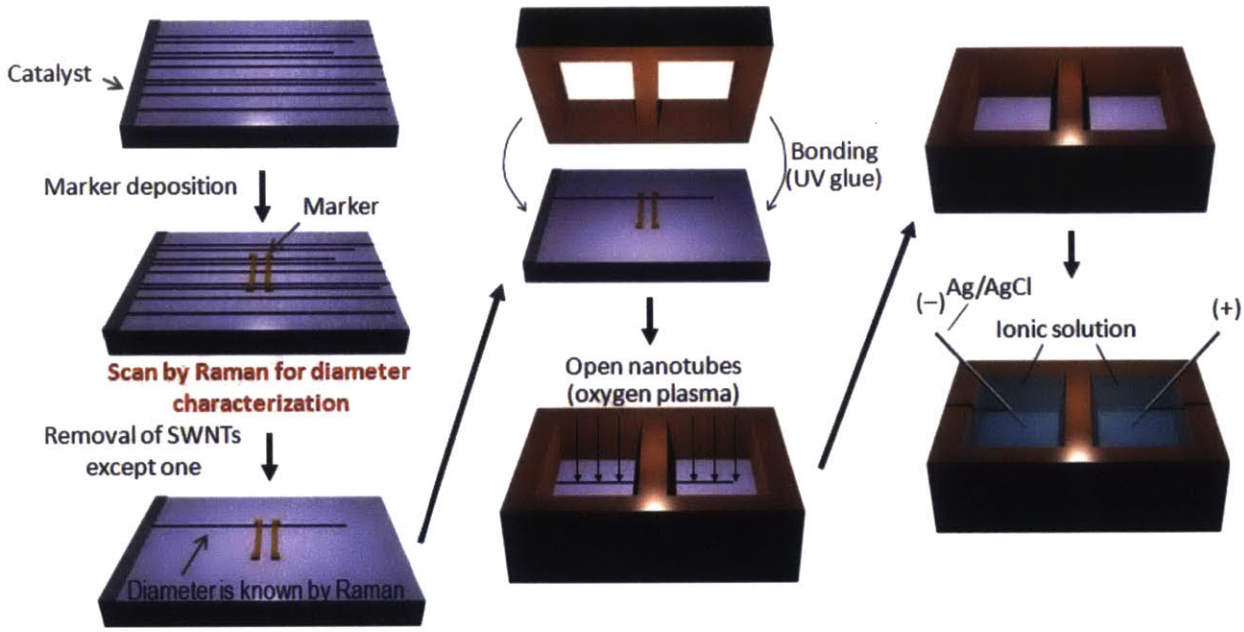

Figure 5. Experimental method for manufacturing single-SWNT devices with known diameter. First, horizontally-aligned SWNT are grown on a silicon wafer using a chemical vapor deposition growth methods. Fiducial markers are then placed on the chip to aid in alignment between scanning-electron micrographs (SWNT can be seen) and optical micrographs (SWNT cannot be seen). Raman spectroscopy is then employed to determine the diameter of a SWNT of interest, and the remaining SWNT are etched away. Epoxy reservoirs are then placed onto the SWNT through UV glue bonding, and oxygen plasma is used to remove exposed SWNT regions and open up the ends of the SWNT. Electrolyte solutions are then placed in the reservoirs, followed by voltage clamp measurements.

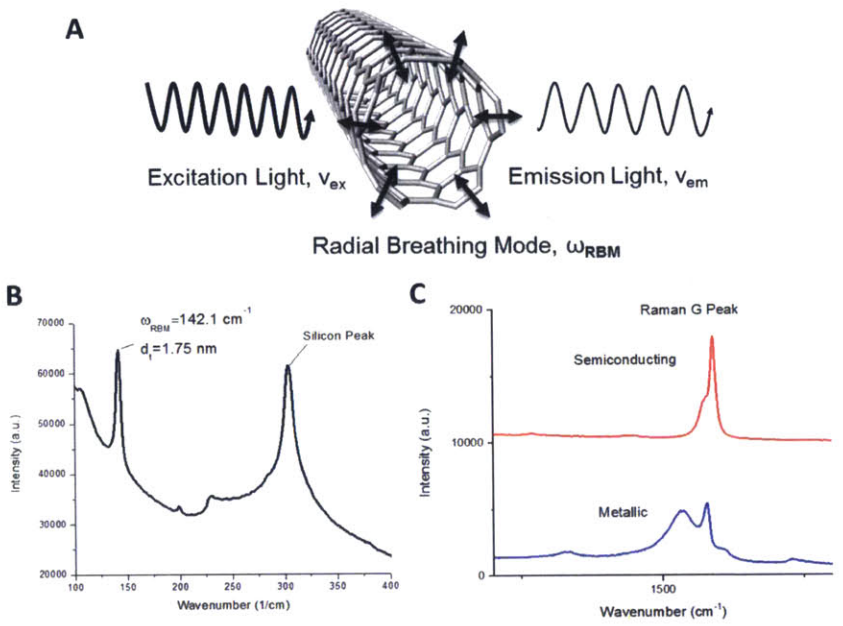

Figure 6. Raman spectroscopy overview of carbon nantoubes. (A) In Raman spectroscopy, a monochromatic excitation source is inelastically scattered, typically to a lower frequency. The frequency change of light corresponds to a phonon or vibrational mode in the nanotube. One of the vibrational modes shown here is the radial breathing mode (RBM), which corresponds to vibrations of the carbon atoms in a radial direction. (B) Sample spectrum showing an RBM peak, whose wavenumber position is inversely proportional to the nanotube diameter. (C) Sample spectra showing the G-peak of the nanotube, the shape of which provides information on the metallicity of the tube (semiconducting or metallic).

Voltage clamp measurements were performed using the Axopatch 200B amplifier and Digidata 1440A digitizer from Molecular Devices, LLC. Silver/silver chloride (Ag/AgCl) electrodes were prepared by chloriding silver wire in bleach for 5-10 minutes. Ag/AgCl electrodes are used because the redox reactions do not form any gaseous species, utilize chloride ions already present in the solution, and they are fairly stable:

(1) $$Ag^0(s) + Cl^-(aq) \Leftrightarrow AgCl(s) + e^-$$

These electrodes were immersed in the device reservoirs and connected to the amplifier, which applies a fixed, specified voltage between the electrodes and measures the instantaneous current required to maintain that voltage. The current is amplified and sent to the digitizer, which converts the voltage and current into a digital signal for storage on the computer.

As the currents being measured are very small (picoamp range), it is imperative to carefully shield all electronic components using a Faraday cage and float all the components on an air table to reduce vibrational noise. High frequency noise was filtered by applying a 5 kHz low-pass analog filter, and the sampling rate was set at 20 kHz.

3.3 Results and Discussion

3.3.1 Experimental Evidence for Stochastic Ion Transport

As evidence for the mechanism of stochastic blocking of proton current by larger cations, the dwell time and pore-blocking current were measured after varying the voltage across the nanotube. For the stochastic ion transport mechanism, the dwell time is the length of time that a single ion resides inside the nanotube. The dwell time can be estimated as:

$$(2)\quad \tau_{dwell,ion} = \frac{L^2}{\mu_{ion} \cdot (V - V_{threshold})} \propto \frac{1}{(V - V_{threshold})}$$

where L is the length of the tube [m], μ_{ion} is the mobility of the ion [m^2/V-s], V is the applied voltage [V], and $V_{threshold}$ is a threshold voltage [V] below which no ions enter the tube. The dwell time is thus proportional to $1/(V-V_{threshold})$, which fits the data trend in Figure 7A.

Likewise, the magnitude of pore-blocking current can be estimated to be

$$(3)\quad \Delta I_{blocking} = \frac{q \cdot \mu_{H^+} \cdot n_{H^+} \cdot A_{blocked} \cdot (V - V_{threshold})}{L} \propto V$$

where q is the charge of a proton [C], μ_{H^+} is the proton mobility inside unblocked nanotube [m^2/V-s], n_{H+} is the number density of protons inside the nanotube [#/m^3], and $A_{blocked}$ is the area occluded by the blocking ion inside the nanotube [m^2]. This relationship shows that the pore-blocking current is linearly related to the applied voltage.

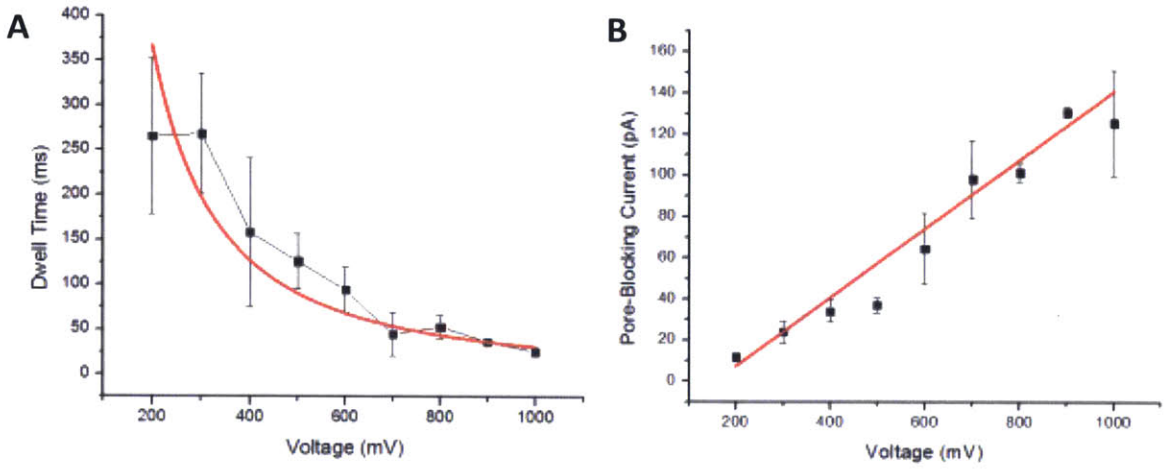

Figure 7. Evidence for stochastic ion transport. (A) The dwell time of fluctuations as a function of applied voltage showing a $1/(V-V_{threshold})$ dependence, as predicted by electrophoretic transport of ions through the nanotube. (B) The magnitude of pore-blocking current as a function of applied voltage showing a linear dependence, as predicted by electrophoretic transport of protons through the nanotube.

Table 1 provides a summary of experimental evidence pointing toward the mechanism of stochastic ion transport.[19, 37]

Table 1. Summary of experimental evidence for stochastic pore blocking of protons by cations

Proposed Characteristics of Stochastic Pore Blocking in SWNT	Experimental Evidence
Protons are the main charge carriers	1. Conductivity decreases with addition of salt
	2. Increasing pH decreases the pore blocking current
	3. Using D_2O decreases the pore blocking current
	4. Pore-blocking current increases linearly with applied voltage
Cations are blockers	1. Conductivity decreases with addition of salt
	2. Large cation salts (tetramethylammonium chloride) do not result in pore blocking events
	3. Experiments with just water or HCl do not yield pore blocking events
	4. The dwell times are inversely proportional to applied voltage

3.3.2 Raman Analysis

We fabricated roughly 100 devices containing primarily single SWNT, although a few devices had two or three characterized SWNT. From the Raman spectrum, the radial breathing mode (RBM) peak position was measured, and the nanotube diameter was calculated using the following relation: $d_t = 248/\omega_{RBM}$, which is valid for isolated SWNT sitting on a silicon oxide substrate[38]. The Raman RBM spectra for all 20 different nanotube diameters are shown in Figure 8. It should be made aware that one device actually contained a double-walled carbon nanotube (DWNT), as indicated by the presence of two RBM peaks; in this case, the smaller, inner tube's diameter was used.

The G band of the carbon nanotube corresponds to tangential vibrations of the carbon atoms in the carbon nanotube, and it is observed at higher wavenumber shifts (~1550-1600 cm^{-1}) in the Raman spectrum. The G band contains two peaks, the G^- and G^+ peaks, where the G^+ peak stays mostly constant around 1591 cm^{-1} and the G^- peak is at lower wavenumber shifts and changes more dramatically. The shape of the G^- peak gives evidence of the metallicity of the tube. Metallic tubes have broader G^- peaks that are softened compared to those of semiconducting tubes. Metallic G^- peaks can also be fitted to a Breit-Wigner-Fano (BWF) lineshape, compared with a Lorentzian lineshape for those of semiconducting tubes.[39] The deconvoluted Raman G band spectra for all 20 different nanotube diameters are shown in Figure 9, with the G^- peak fitted to a BWF or Lorentzian (depending on whether the nanotube was determined to be metallic or semiconducting), and the G^+ peak fitted to a Lorentzian. In several cases, an additional peak was observed, which was thought to be due to amorphous carbon around the SWNT from the growth process.

The criteria used to determine the metallicity of the tube was by first looking for distinctly broad or sharp G^- peaks, which would indicate that the nanotube was metallic or semiconducting, respectively. For tubes whose assignment was still ambiguous, the position of the G^- peak was used to determine the metallicity, as metallic tubes have softened G^- phonon modes relative to semiconducting tubes. The empirical fits from Jorio et al. were used to assign metallicity to the ambiguous tubes, as shown in Figure 10.[40] The diameters and metallicity of all the nanotubes are summarized in Table 2.

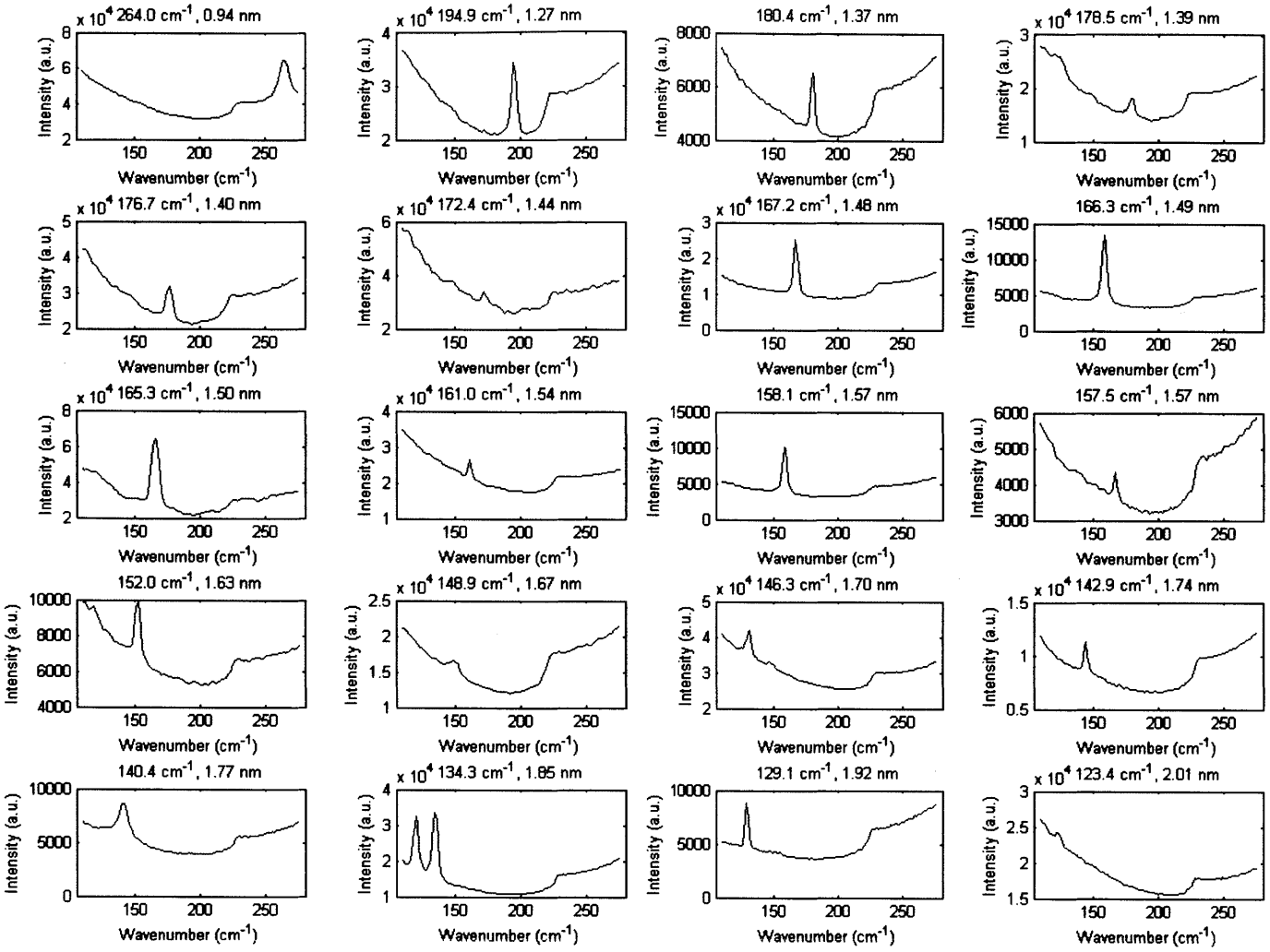

Figure 8. Plots of Raman spectra showing the radial breathing mode (RBM) feature for all carbon nanotubes from devices used in the diameter study, sorted in order of increasing diameter. The position of the RBM and corresponding tube diameter are listed above each plot. The sample at 1.85 nm actually has 2 RBMs observed, indicating the presence of DWNT; the corresponding diameter was calculated using the inner tube RBM.

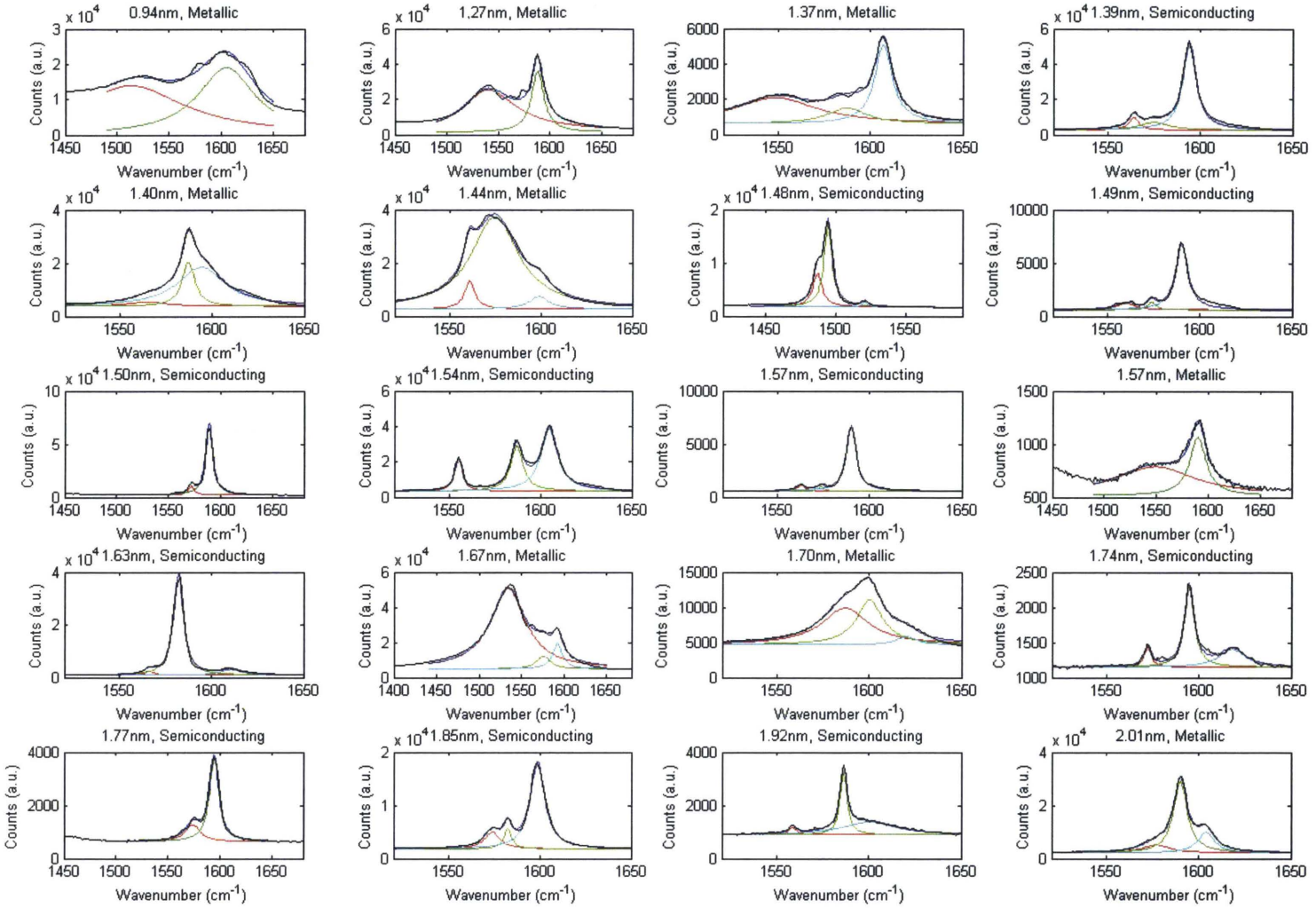

Figure 9. Plots of Raman spectra showing G peak features for all carbon nanotubes from devices used in the diameter study, sorted in order of increasing diameter. The diameter and metallicity of each tube are listed above each plot.

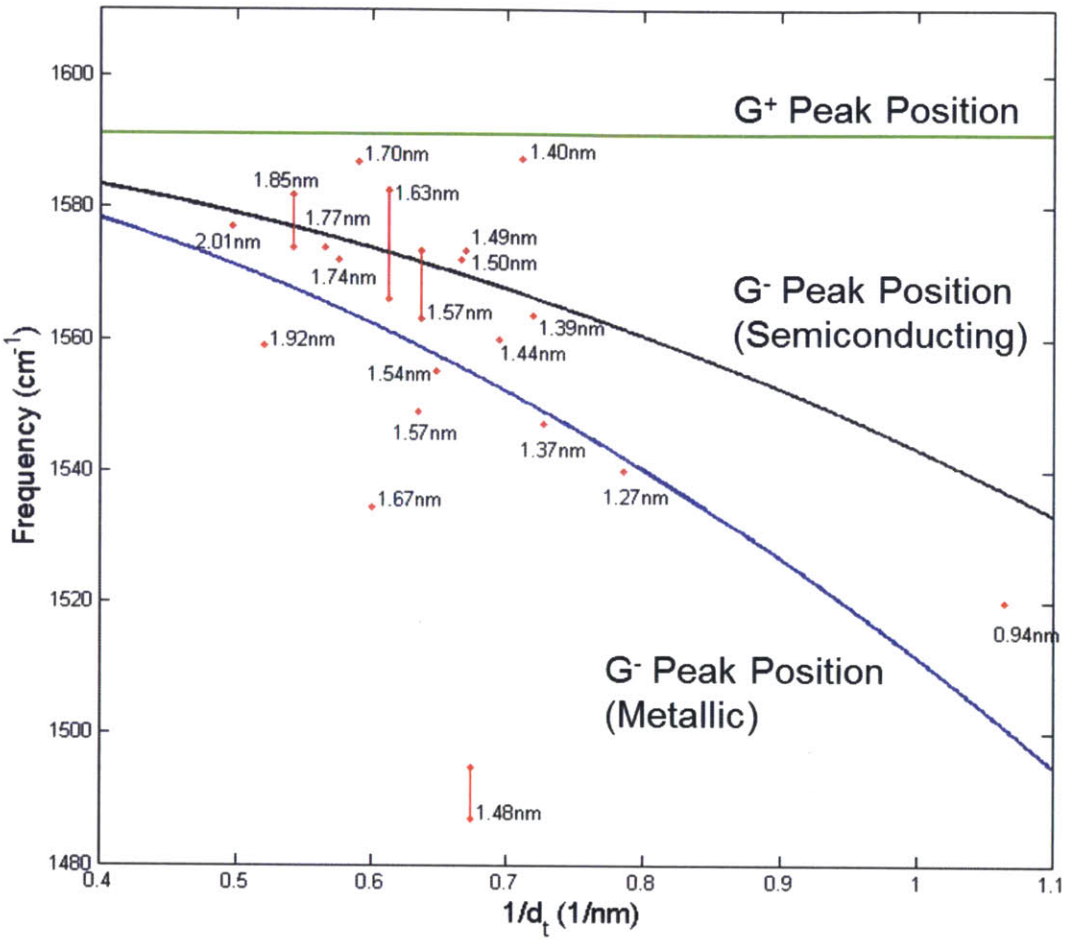

Figure 10. G^- **peak positions are plotted against inverse tube diameter. The lines are plotted according to the empirical fit found by Jorio et al.[40] The lines indicate the position of the G^- peaks for metallic and semiconducting tubes. For reference, the constant G^+ peak position is also shown. Each red point corresponds with a single nanotube used in the diameter study. Vertical red lines connecting two points are for samples which had two possible G^- peaks.**

Table 2. Calculated diameters and corresponding metallicity assignment

Diameter (nm)	Nanotube Metallicity (M = metallic, S = semiconducting)
0.94	M
1.27	M
1.37	M
1.39	S
1.4	M
1.44	M
1.48	S
1.49	S
1.50	S
1.54	S
1.569	S
1.575	M
1.63	S
1.67	M
1.7	M
1.74	S
1.77	S
1.85*	S
1.92	S
2.01	M

*Diameter and metallicity are for the inner tube of this DWNT

3.3.3 Voltage Clamp Analysis

Subsequently, we characterized the devices using voltage clamp measurements and measured the dwell time, pore-blocking current, and open-channel lifetime. Data was analyzed using the pClamp software (v. 10.3). First, a section of data exhibiting pore-blocking events at constant voltage was found, and the current was baseline subtracted manually. Typically, there will be a non-zero

baseline current from leakage current through the epoxy barrier, as well as baseline current traveling through the nanotube. In cases where the noise level of the current trace was commensurate with the pore-blocking magnitude, the current trace was de-noised using boxcar averaging using 20 points. The events were analyzed using the single-channel analysis feature in the software, where the open- and closed-states are defined by the user. The states are found automatically by the program using the half-amplitude threshold method; essentially, a state is assigned if the current value crosses a certain threshold defined by the magnitude of the current difference between states. The resulting data was analyzed in Matlab to compute the dwell times and pore-blocking currents.

Interestingly, a peak in the pore-blocking currents around 1.57 – 1.63 nm was observed, with lower pore-blocking currents at both lower and higher diameters. To explain this phenomenon, our group put forth a model where the applied electric field drives proton flux through the tube, and the dissipated energy is transferred to the surrounding fluid inside the tube causing convective flow.[41] By parameterizing simulation data in the literature for the slip-length, proton mobility and water viscosity as a function of nanotube diameter, the expected pore-blocking current and dwell times could be calculated and compared with the experimental results as shown in Figure 11.

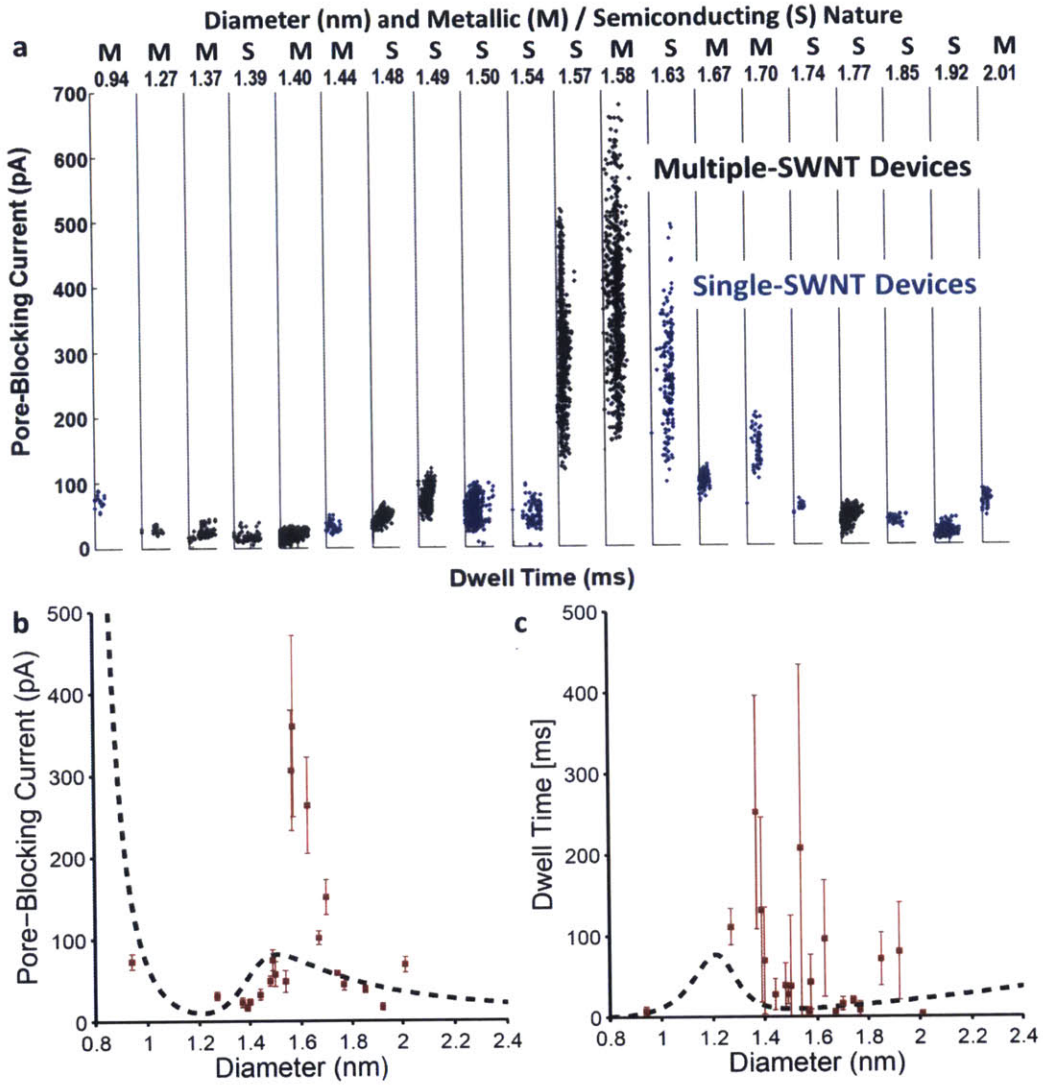

Figure 11. Diameter-dependent voltage clamp measurement results. (A) Scatter plots of pore-blocking current and associated dwell times for each nanotube diameter probed, along with the associated tube metallicity. Single-SWNT devices are plotted in blue, and this distribution was used to assign the diameters to the data from multi-SWNT devices. (B) and (C) Plots of pore-blocking currents and dwell times versus diameter, with associated fits from the proposed model.

3.4 Conclusions

In conclusion, we carried out fundamental experiments measuring the pore-blocking characteristics of individual single-walled carbon nanotubes. Each nanotube was carefully characterized using Raman spectroscopy, which allows the precise determination of diameter and metallicity. The

magnitude of proton current passing through the nanotube was measured using a voltage clamp apparatus. As the proton current becomes blocked by larger cations, stochastic and discrete fluctuations in current are recorded. The pore-blocking currents appear to match a trend found in MD simulations showing a non-monotonic trend in slip lengths as a diameter increases.

4. Stochastic Pore Blocking and Gating in PDMS-Nanopores from Vapor-Liquid Phase Transitions

4.1 Introduction

There is significant interest in the use of isolated, synthetic nanopores for separation and analytical applications.[5, 25, 42-43] It is of particular interest to study the voltage-driven transport properties of these nanopores through a voltage-clamp apparatus, as this allows high-fidelity electronic readout corresponding to the current moving through the pore. These measurements have demonstrated several interesting transport properties and regimes found inside nanopores, including stochastic ion pore-blocking,[19, 34, 44] nanoprecipitation, and electric field-induced wetting/dewetting.[45] Nearly all of these isolated, synthetic nanopores consist of the following materials systems: carbon nanotubes,[44] SiN or SiO_2 nanopores,[46] and track-etched polymer membranes.[47]

Patch clamp is a widely used technique in electrophysiology to monitor ionic currents and the kinetics of channel opening through biological ion channels in cell membranes. In this technique, a micropipette is patched onto a very small section of the cell membrane under voltage clamp conditions.[48] However, its application to synthetic nanopores has been investigated only in a few cases.[49-50] The stochastic nature of biological ion channel gating has been studied extensively in the literature and is usually attributed to a conformational change in the protein ion channel; various ion channels can be activated by transmembrane potentials, ligands binding to receptors on ion channels, and other stimuli. Recent developments involving patch clamp have included very precise electrochemical imaging[51] and high throughput planar patch clamp methods.[52]

Because the gating described previously for biological ion channels is only thought to exist due to conformational changes, only a few studies have performed patch clamp on synthetic membranes, since no stochastic behavior would be expected for passive pores. These studies have shown anomalous fluctuations when patching onto tracked-etched membranes or flat PDMS surfaces, but the cause of these fluctuations in the absence of well-defined blocker molecules has not been satisfactorily addressed.[49-50, 53-54] Proposed mechanisms for these fluctuations have included changes

in surface charge at the pore wall,[53] thermal fluctuations that pinch off thin strands of water between the glass tip and PDMS,[49] and internal adsorption of ions which can result in chaotic behavior of ion concentration over time.[50]

In this work, we apply the patch clamp technique to study and understand ion transport through nanopores specifically patterned or otherwise in PDMS allowing for their characterization. Anomalous events can occur in new situations that are entirely unexpected, so very thorough control experiments are necessary before making conclusions in any new platform. The observed fluctuations studied in this work are shown to be distinct from our recent observations[19, 34] in single-walled carbon nanotube pores. In our recent carbon nanotube work, the duration of the fluctuations in the off state (the dwell time) is inversely related to the applied potential and varies with the type of cation in the system, indicating a well-defined, charged blocking event. In contrast, this work studies a mechanism that appears to be invariant with the applied electric field.

4.2 Experimental Methods

We set up a patch clamp system using a Multiclamp 700B amplifier and Digidata 1440A digitizer from Molecular Devices. Glass pipettes were freshly pulled before experiments using a Sutter pipette puller (Sutter P-1000) using 1.5mm OD and 1.1mm ID fire-polished borosilicate glass capillary tubing such that the inner tip diameter was 1.2μm and a wall width of 170nm, as verified by scanning electron microscopy (SEM). The tip and bath were filled with electrolyte solutions, and subsequent solutions were perfused through shielded polyethylene tubing using a syringe pump for infusion and an aspirator for withdrawal. The electrolyte solutions of a wide concentration range were prepared through serial dilution using Mill-Q deionized water. The entire setup was housed in a grounded Faraday cage.

The PDMS surfaces were prepared using Sylgard 184 from Dow Corning. The base and curing agent were mixed in a ratio of 10:1 by mass, followed by 30 minutes of degassing under vacuum. The PDMS was then drop-cast onto a silicon chip and heat cured on a hot plate at 180°C for 15 minutes. Grooved PDMS surfaces were made using unwritten CD-R and DVD-R discs as templates using a

procedure described in detail elsewhere.[55] AFM images showed CD-R templated PDMS had a groove depth of 73.1 ± 6.3 nm, with a groove spacing of 1.48 ± 0.03 μm; DVD-R templated PDMS had a groove depth of 75.8 ± 2.7 nm, with a grooved spacing of 0.73 ± 0.02 μm.

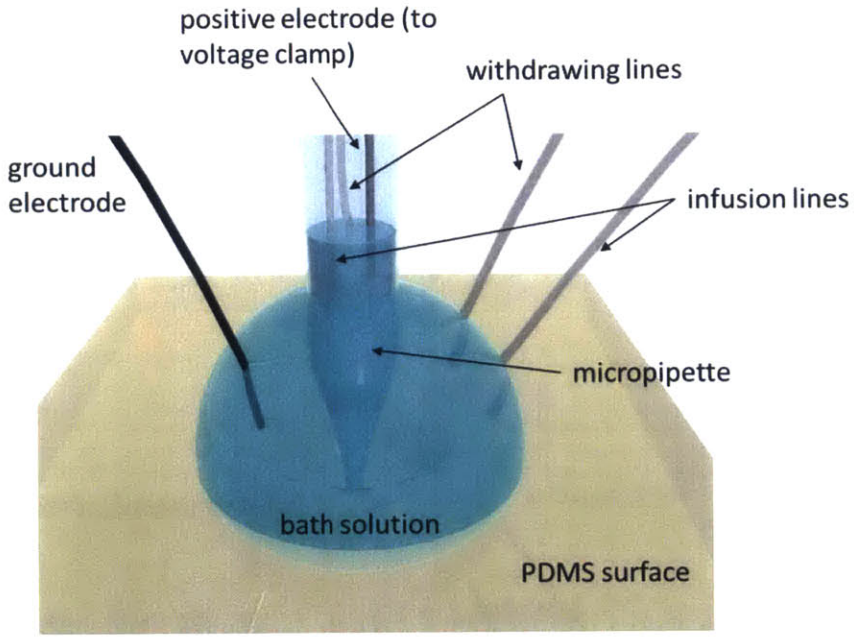

Figure 12. Schematic of patch clamp experiment on PDMS surface. The glass micropipette is pressed into the PDMS to form a seal between the solution in the tip and the bath. Infusion and withdrawing lines in the pipette tip and bath allow solution exchange on the same patched spot without affecting the seal.

4.3 Results and Discussion

Patch clamp experiments on both grooved and flat PDMS surfaces yielded stochastic current fluctuations, as shown in Figure 13. Current fluctuations were observed with solutions of LiCl, NaCl, KCl, CsCl, and $CaCl_2$ of concentrations ranging from $1x10^{-3}$M to 3M. Persistent experimental artifacts were ruled out as the cause, because these stochastic current fluctuations were observed in <30% of the flat PDMS samples, and <50% of the grooved PDMS samples. PDMS samples were rinsed thoroughly with DI water and dried with nitrogen gas before patching onto them. AFM images generally showed a clean, flat surface so contamination is not thought to be an issue. Furthermore,

the fluctuations disappear as the seal is tightened significantly past the point of a reasonable seal, indicating that electrical or grounding artifacts are not the cause. There are also no fluctuations observed when the pipette is just immersed in the bath solution, indicating that the patch itself is contributing to these fluctuations.

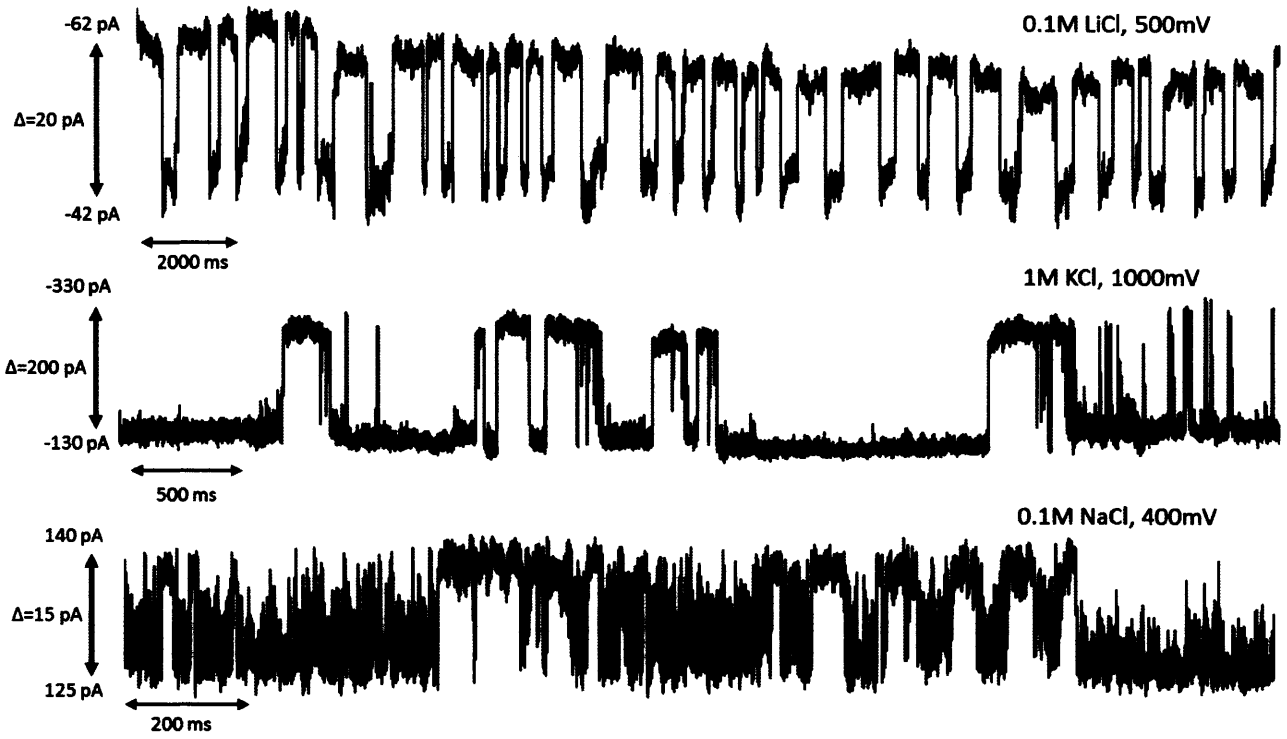

Figure 13. Representative current traces showing discrete stochastic current fluctuations when patch clamping onto flat PDMS surfaces. Negative currents imply a negative polarity being applied (the electrode inside the micropipette is at a negative bias with respect to the bath solution).

After patching onto the surface of flat PDMS samples and observing these fluctuations, many of them indicated the presence of a single pore (two Coulter states). To confirm that the conduction path in these cases exists within the PDMS itself, grooved PDMS surfaces were made by templating PDMS using unwritten CD-R and DVD-R disks, which have tracks spaced 1.6 μm and 740 nm, respectively. Figure 14 shows an AFM image of a grooved PDMS surface made using a CD-R template, and outlines showing possible random placements of the tip onto the PDMS surface. Patching onto a grooved PDMS surface forms 0, 1 or 2 nanopores on the surface as shown. Overall,

16 out of 33 (48%) of grooved PDMS samples produced stochastic current fluctuations. In cases where no stochastic current fluctuations were observed, it is difficult to know whether a pore was formed or not since it is possible that the nanopore remains in a high conducting state or a low conducting state; this experiment can only distinguish the nanopore current from leakage current when there are fluctuations between the two conductivity states.

For example, two pores that switch conductivity states independently result in 3 or 4 current states. Three current states are observed when two independent pores are formed that have the same conductivity change when switching from an open to a closed state. Thus, the current state associated with a single pore being open is degenerate. Four current states are observed when two independent pores are formed which each have different conductivity changes when switching between open and closed states. Thus, there are two non-degenerate current states when a single pore is open and the other closed.

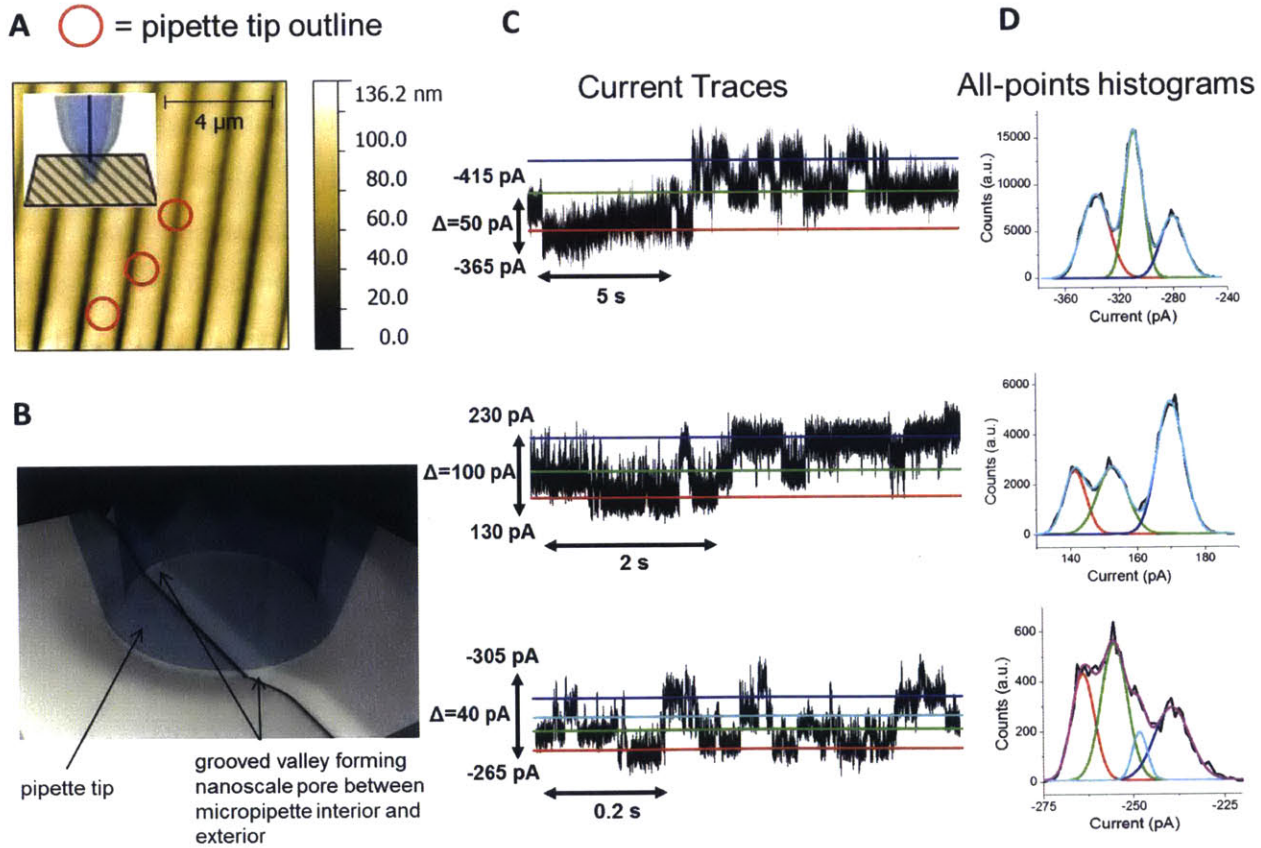

Figure 14. Patch clamp on grooved PDMS surfaces. (A) An AFM image of PDMS grooves formed using a CD-R disk as a master. The red circle depicts the outline of a 1.2 um diameter pipette tip, and random placements on the surface will yield preferentially 0-2 expected channels between the glass tip and PDMS surface. (B) A schematic of patching onto a grooved PDMS surface preferentially forming 2 nanopores. (C) Current traces from patching onto grooved surfaces using 0.1M NaCl demonstrate that 3 or 4 Coulter states appear indicating the presence of two channels. (D) The all-points histograms verify the presence of multiple states.

To further confirm that the pore was due to nanochannels made by the interface of PDMS and glass, the baseline and magnitude of stochastic current fluctuations were monitored as a function of tip penetration depth into the PDMS surface, as depicted in Figure 15. It should be noted that the distance of penetration was recorded from the stage micromanipulator, which is not an accurate measure of actual penetration depth since the pipette tip can be pushed back into its pipette holder. However, it is clear that the pore that is causing fluctuations can be compressed and made smaller, resulting in lower blockade currents. The baseline current is seen to go toward an asymptote around 25 pA, which may represent the inherent porosity of the PDMS substrate. This experiment confirms that the pore is due mainly to channels at the PDMS-glass interface rather than through defects in the glass, for example. Defects right at the pipette tip could possibly contribute to forming part of the channel at the PDMS-glass interface, although SEM images of the tip show a surface smoother than that of the grooved PDMS samples (see Figure S1), making this possibility unlikely. While PDMS is known to be an inherently porous material for gases and liquids, [56-57] which would contribute slightly to the leakage current, the diffusive transport of electrolyte through the free volume of the polymer is not expected to give rise to clear, discrete current states. On the other hand, pores formed at the grooved PDMS-glass interface have a much likelier possibility of forming discrete, straight-line pores that could be individually blocked.

Unlike previous work in our group studying stochastic pore-blocking from ions in single-walled carbon nanotubes (SWNT), where the majority charge carriers were found to be protons,[19, 34] concentration experiments confirmed that the majority carriers in these PDMS nanochannels were the electrolyte cations and anions (see Figure 15c-d).

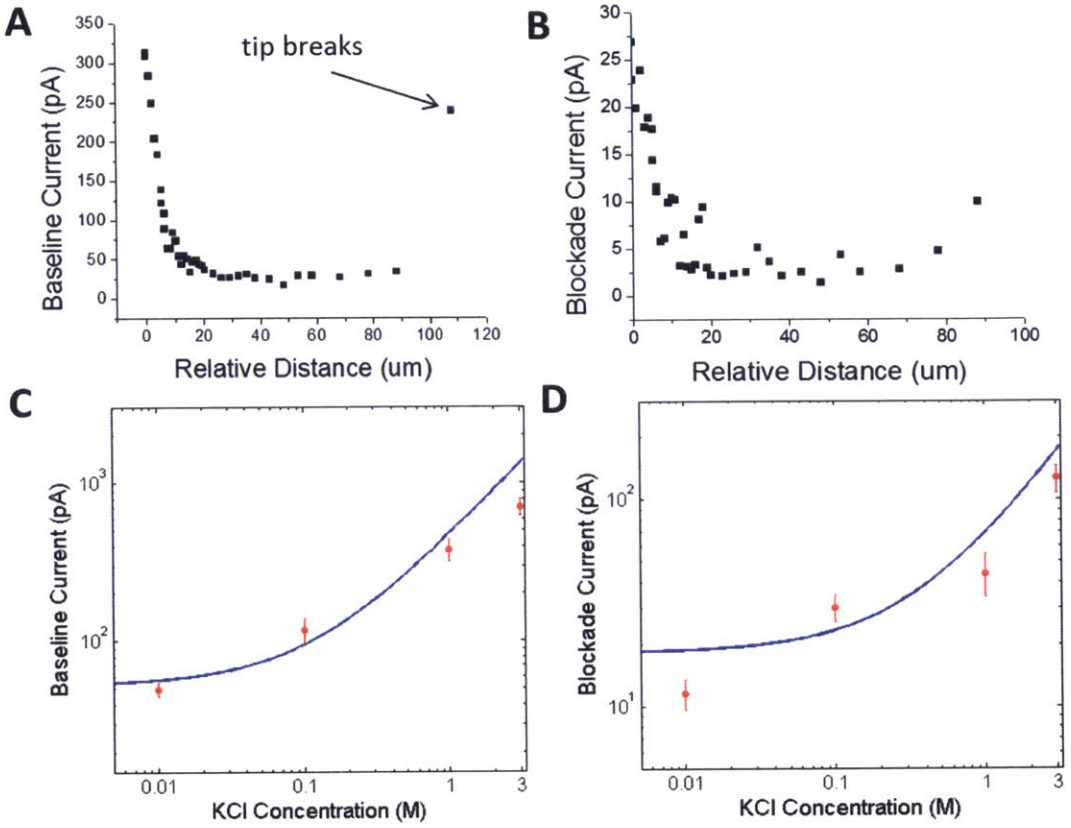

Figure 15. The effect of tip compression into the PDMS surface is to decrease the overall baseline current (A) and blockade current (B) indicating the pore is due to the PDMS, which is deformable under pressure. If too much pressure is applied, the pipette tip begins to crack, resulting in a higher baseline current. The identity of the majority charge carriers can be seen by observing the baseline conductance (C) and blockade current (D) as a function of electrolyte concentration. It is clear that the baseline and blocked current is carried by the electrolyte. The blue line is a fit to the data using Eq. (4).

The relationship between pore diameter and conductivity can be obtained using full molecular dynamics (MD) simulations which can be very computationally intensive.[58] Another method employs a multiscale approach--using MD simulations to generate ion mobilities inside the nanopore and continuum models (Navier-Stokes and Poisson-Nernst-Planck equations) to simulate the electrohydrodynamics.[59] These sophisticated models are most necessary when the pore diameter is <1 nm and the Debye length is comparable with the pore radius.[58-59] In this case, where the pore geometry is less well-defined and diameter unknown beforehand, simpler analyses are carried out to give a rough estimate of effective pore diameters.

A simple model relating pore conductance with the effective pore diameter, assuming a cylindrical pore geometry and a charged layer of zero thickness adjacent to the oppositely-charged surface (similar to the Helmholtz double layer approximation of zero thickness), is provided by Eq. (4),[60] which shows that the pore conductance is

$$(4)\quad G = \frac{\pi}{4}\frac{d_{pore}^2}{L_{pore}}\left(\left(\mu_+ + \mu_-\right)n_{electrolyte}e + \mu_K\frac{4\sigma}{d_{pore}}\right)$$

where G is the pore conductance (A/V), d_{pore} is the diameter of the pore (m), L_{pore} is the length of the pore (m), μ_+ and μ_- are the ion mobilities of the cation and anion, respectively (m^2/V-s), $n_{electrolyte}$ is the number density of the electrolyte species (#/m^3), e is the elementary charge (1.602x10^{-19} C), and σ is the negative surface charge density of the nanopore (C/m^2). Our calculations show a relatively weak surface charge of roughly -0.015 C/m^2 (or 11 nm^2/e^-) for native PDMS. The length of the pore can be assumed to be the thickness of the micropipette tip (170 nm).

A second relationship that better accounts for the diffuse double layer of finite thickness inside the nanopore is

$$(5)\quad G = \frac{\pi}{4}\frac{\left(d_{pore}-2\kappa_D\right)^2}{L_{pore}}\left(\left(\mu_+ + \mu_-\right)n_{electrolyte}e + \mu_K\frac{4\sigma d_{pore}}{\left(d_{pore}-2\kappa_D\right)^2}\right)$$

which assumes that within the Debye length ($\kappa_D(nm) = 0.304/\sqrt{I(M)}$) from the negatively-charged pore walls there is a concentration of cations that cancels out the surface charge (assuming anion concentration is negligible in this region); outside of this diffuse double layer is the bulk ion concentration.

Thirdly, if the mechanism of blocking is due to a phase transition, as will be postulated later, the fractional change of mean ion density inside the nanopore relative to the bulk ion density, denoted Δk, is only about 0.15.[61] As the mean ion density accounts for variation due to the charged surfaces, the surface charge term is not needed, and Eq. can be used to represent the change in conductance between the high- and low-conducting states. This calculation results in a larger calculated diameter since a larger nanopore is required to produce the same conductivity change if the density change is a fraction of that of the bulk.

(6) $$\Delta G = \frac{\pi}{4}\frac{d_{pore}^2}{L_{pore}}\left(\left(\mu_+ + \mu_-\right)\left(\Delta k\right)n_{electrolyte}e\right)$$

The diameters for 10 samples were calculated using these three methods. The first two methods assume that the pore is completely empty in the low-conducting state and so G is replaced by ΔG, the total change in conductance between the two states as determined by the blockade current. Figure 16 shows the diameter distributions using these different calculation methods. In the first case, the diameters range from 0.6 – 3.2 nm (1.9±0.7 nm); the second case yields diameters from 0.8-4.6nm (2.8±1.1nm); the third case yields diameters from 3.6 – 11.2 nm (7.4±2.1 nm). In all cases, the pore diameter is on the order of several nanometers. However, it is not possible to characterize the pores directly because their existence depends on the contact of the patch clamp tip with the PDMS surface.

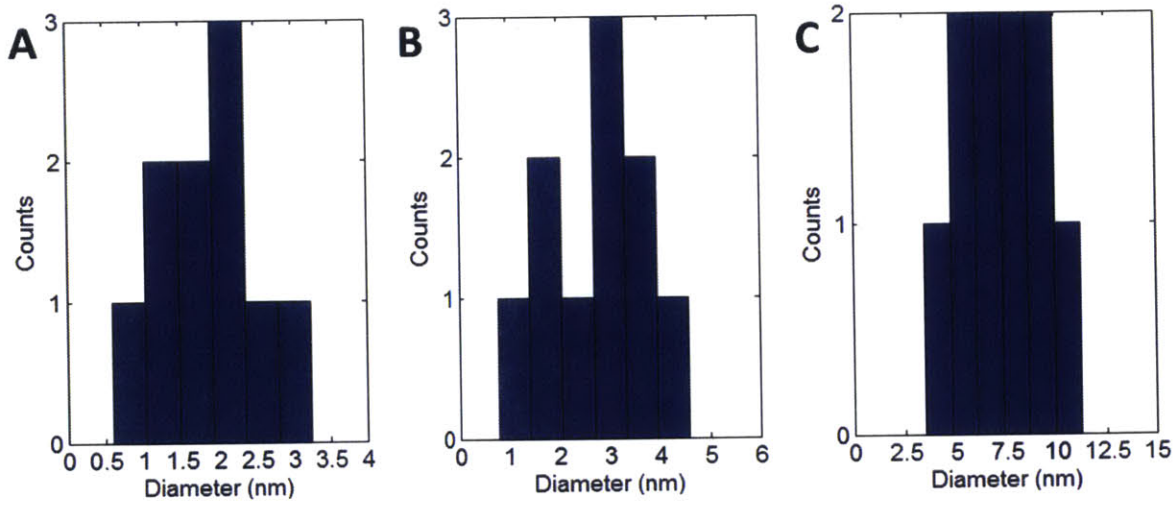

Figure 16. Calculated diameter distributions under the same experimental conditions (0.1M NaCl, 1000 mV, grooved PDMS sample, 170 nm thick tips). The diameters are calculated (A) using Eq. (4), (B) using Eq. (5), and (C) using Eq. (6).

To further confirm the presence of nanometer-sized, hydrophobic pores, experiments were performed using anionic and nonionic surfactants. The results, shown in Figure 17a, demonstrate that increasing concentrations of sodium dodecyl sulfate (SDS), an anionic surfactant, leads to an increase in baseline conductance. The same concentration experiment with Triton X-100, a nonionic

surfactant with only polar head groups, shows the opposite trend of decreasing conductance. In both cases, the baseline conductance flattens out past the critical micelle concentration (cmc). The cmc represents the point at which adding more surfactant results in mostly forming micelles. Assuming there is equilibrium between free monomer surfactant in bulk solution and adsorption inside the nanopore, one would expect any effect of surfactant concentration on nanopore transport would diminish past the cmc, which is indeed observed.

Assuming the pore is hydrophobic, the aliphatic part of the surfactant molecule will to adsorb to the hydrophobic pore surface. For a nonionic surfactant, surface adsorption will only decrease the cross-sectional area of the pore in theory and result in lower pore conductance. However, a significant decrease in pore conductance only occurs if the pore diameter is small, commensurate in scale with the thickness of the adsorbed layer. Assuming that the entire baseline current moves through approximately a single pore and Triton X-100 (~2 nm in length) coats uniformly around a cylindrical pore, the original pore diameter is calculated to be about 6.7 nm. However, if the pore is slit-shaped, the calculated pore height is around 4.8 nm. These estimates agree closely with those made directly from the pore conductance equations in the previous section.

$$(7)\quad \frac{G}{G_{surf}} = \frac{0.09nS}{0.015nS} = 6 = \frac{d^2}{d_{surf}^2} = \frac{d^2}{(d-\Delta d)^2} = \frac{d^2}{(d-2(2nm))^2} \rightarrow d = 6.7nm$$

$$(8)\quad \frac{G}{G_{surf}} = \frac{0.09nS}{0.015nS} = 6 = \frac{h}{h_{surf}} = \frac{h}{(h-\Delta h)} = \frac{h}{(h-2(2nm))} \rightarrow h = 4.8nm$$

For an anionic surfactant, like SDS, the pore surface will become more charged, which will significantly enhance transport only if the pore is small (the surface transport term in Eq. (4) is inversely proportional to diameter). There are two competing effects upon addition of SDS surfactant: the pore diameter will decrease which reduces bulk transport, but the surface charge will increase which enhances surface transport. For a 6.7 nm diameter pore, we calculate that the observed overall increase in conductance upon addition of SDS can be achieved with a physically reasonable surface charge density (0.28 C/m^2 or 0.57 nm^2/e^-) which is provided by the surfactant molecules.

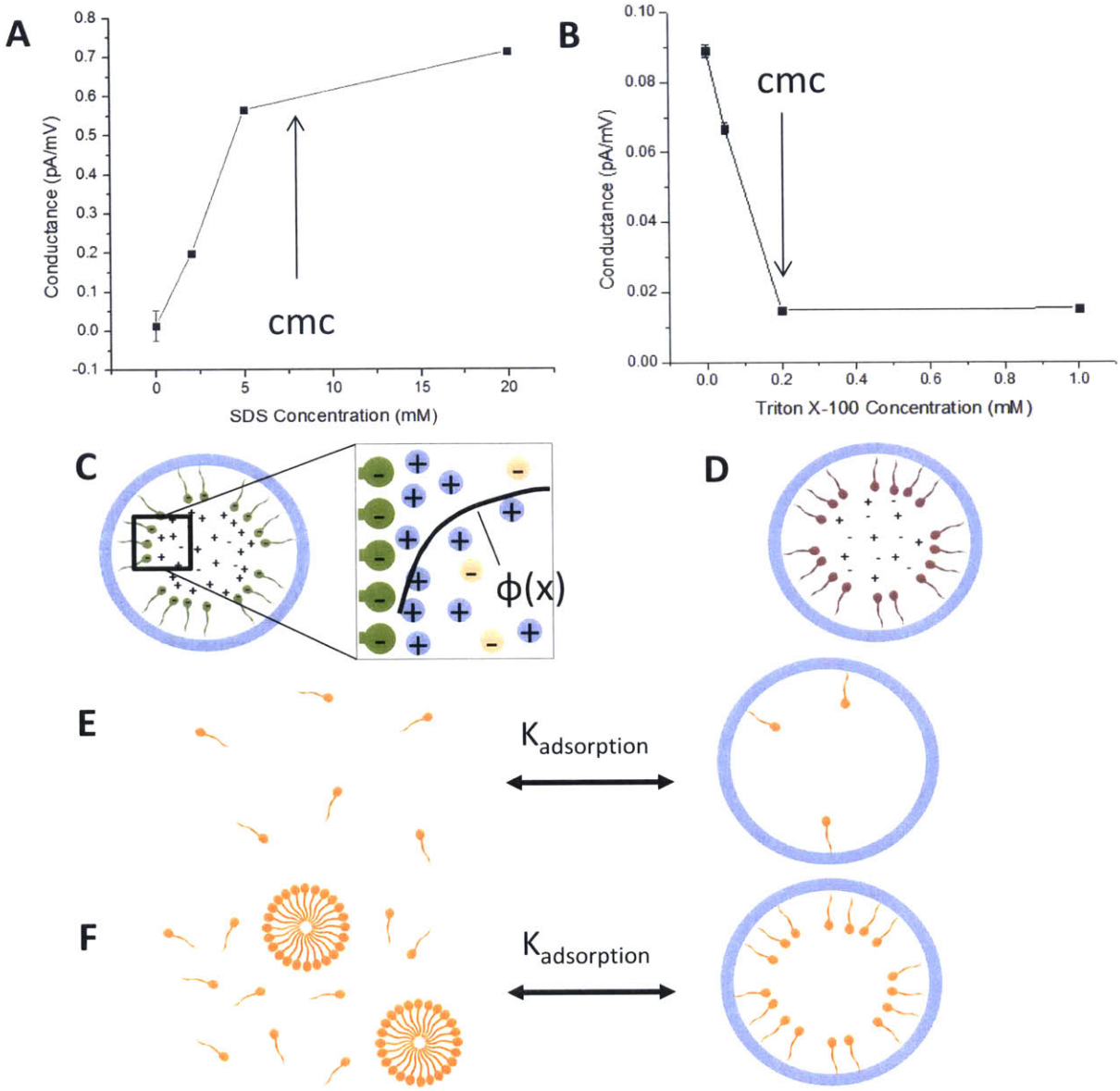

Figure 17. Effect of surfactant on pore properties. (A) The conductance increases upon addition of anionic SDS surfactant, and the change in conductance decreases as the concentration increases past the critical micelle concentration (cmc). (C) As shown in the schematic, an increase in pore conductance can be attributed to the increase in surface charge transport due to the presence of charged groups inside the pores which causes a buildup of charge near the surface. ϕ(x) is the electric potential near the surface. (B) The conductance decreases upon addition of nonionic Triton X-100 surfactant, and this change flattens out past the cmc. (D) The schematic shows that adsorption of nonionic surfactant does not increase surface charge transport, but only serves to occlude the pore area. (E) When the surfactant concentration is below the cmc, increasing the surfactant concentration increases the amount of free monomer in solution, which will increase the surfactant adsorption into the PDMS nanopores. (D) Past the cmc, increasing surfactant

in solution serves mainly to increase micelle concentration. Thus, the PDMS nanopore becomes saturated with surfactant molecules past the cmc.

There have been several studies performing voltage clamp on non-biological nanopores that observe stochastic current fluctuations or resistive pulses. There have been several mechanisms proposed to explain these discrete fluctuations, all of which may be accurate for the specific system in study: blockage by a charged ion or molecule,[19, 34, 44, 60] nanoprecipitation,[62] and complete wetting/dewetting of the nanopore (e.g. the presence of a nanobubble).[45, 59]

To ensure that the observed stochastic current fluctuations are not due to nanoprecipitation effects inside the PDMS nanopore, precipitation was forced to occur by adding $CaCl_2$ on one side and KH_2PO_4 on the other side. A similar experiment by Powell, et al.[45] demonstrated stochastic current fluctuations in track-etched PET membranes due to transient precipitates blocking the pore, followed by re-dissolution caused by the applied voltage. In our experiment, an electrical bias was applied such that calcium and phosphate ions would be driven toward the nanopore and precipitate to form $CaHPO_4$. As Figure 18 shows, prior to addition of KH_2PO_4 to the bath side, there were no fluctuations observed. However, once KH_2PO_4 was added, there were immediate stochastic current fluctuations that were more asymmetric and triangular-shaped compared to typical current traces observed when just simple electrolytes (e.g. KCl or NaCl) are used, as shown in Figure 13. This asymmetry is in agreement with previous observations of nanoprecipitation.[62] Hence, the mechanism responsible for the current fluctuations that is the focus of this work is distinct from nanoprecipitation.

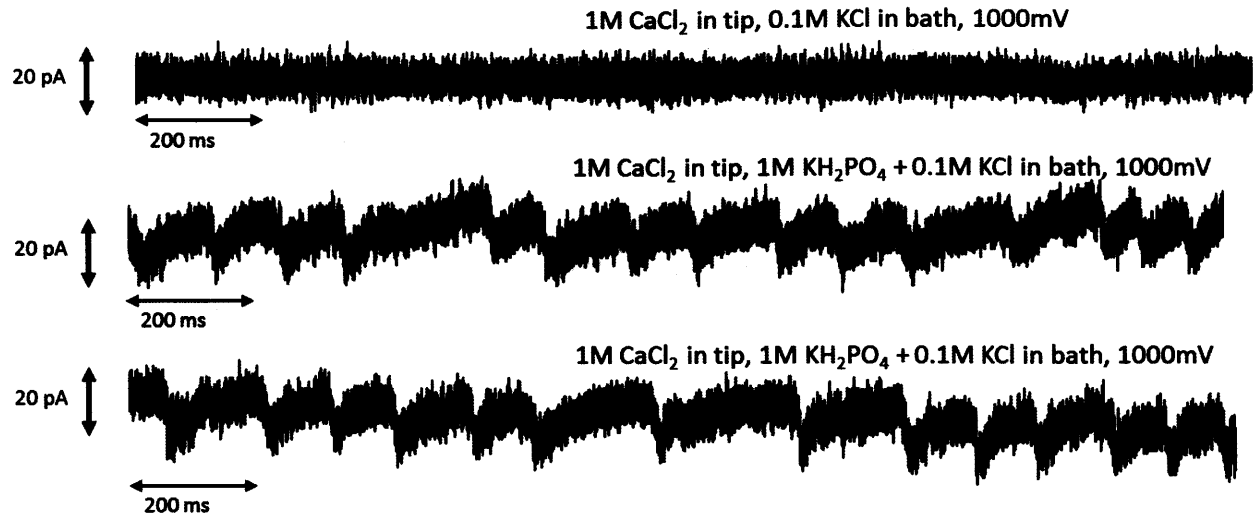

Figure 18. Experimental results demonstrating nanoprecipitation-induced current fluctuations inside the nanopore formed by the tip and PDMS surface. With $CaCl_2$ in the tip and only KCl in the bath, no stochastic fluctuations were observed. However, once KH_2PO_4 was added, this would precipitate to $CaHPO_4$ when the phosphate anion combines with the calcium cation on the other side. The current fluctuations are asymmetric and sloped. The nanoprecipitation-induced fluctuations in PDMS nanopores shown here are quite different than the fluctuations observed using normal electrolytes (e.g. NaCl and KCl), thus ruling out nanoprecipitation as the cause for stochastic current fluctuations.

Stochastic pore-blocking of the nanopore by the ions themselves was ruled out since the blockade current increases with electrolyte concentration, showing that the ions are the majority charge carriers. Also, pore-blocking was not observed in the presence of larger charged molecules, such as DNA, ruling out blocking by a molecule passing through the pore. To further distinguish between blockage by any charged species (the Coulter effect) and a phase transition, the blockade currents and dwell times were tabulated as a function of applied voltage in Figure 19. Pore-blocking data was collected and analyzed from devices made using our previous platform for studying transport through single-walled carbon nanotubes—the blocking phenomenon in these cases was confirmed to be caused by ions blocking an otherwise stable proton current.[19] This blocking mechanism involves a charged blocker moving through the pore, interrupting a baseline current carried by charged particles resulting in a dwell time that decreases as a function of the applied voltage and a pore-blocking current that scales linearly with the applied voltage. As with SWNT nanopores, the PDMS nanopores also demonstrated pore-blocking currents that increase linearly with applied voltage. However, the PDMS nanopores showed a widely variable dwell time distribution that was

not affected by the applied voltage. We conclude that the current blocker is uncharged and therefore not affected by the electric field in the pore.

These results suggest an uncharged "blocker" with a baseline current carried by ions. We explored the theory that there is a phase transition occurring inside the nanopore which causes an ionic concentration change inside the nanopore, such that the pore is rendered non-conducting due to water vapor blocking the pore. This mechanism has been studied theoretically for short hydrophobic/weakly charged nanopores[61, 63-64] and observed experimentally in track-etched PET nanopores with the interior functionalized with hydrophobic groups.[45] This work provides further evidence that this phenomenon is occurring by demonstrating that dwell times are invariant with applied voltage.

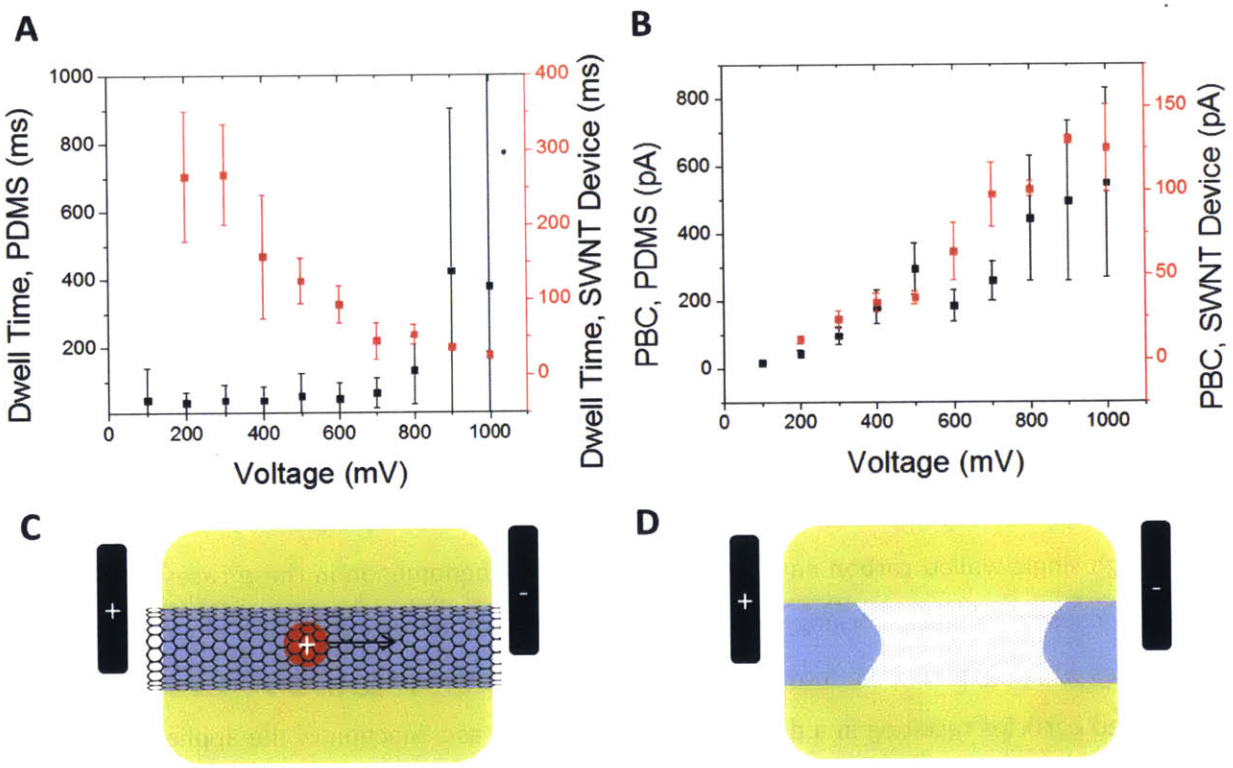

Figure 19. Comparison of the discrete, stochastic current fluctuations of PDMS nanopores and SWNT nanopores. (A) Dwell times as a function of voltage for PDMS nanopores (black, left axis) and for SWNT nanopores (red, right axis). While the dwell times are inversely related to the applied voltage for the SWNT nanopore, they are relatively invariant with respect to voltage for the PDMS nanopore. The large error bars in the PDMS case are due to groups of fluctuations located fewer and farther between at higher voltages. (B) Pore-blocking currents (PBC) as a function of voltage for PDMS nanopores (black, left axis) and for SWNT nanopores (red, right axis). In both cases, there is a roughly linear scaling of PBC with applied voltage. The PDMS nanopore data was taken using 0.1M NaCl, and the SWNT nanopore data

was taken using 1M $CaCl_2$. The inverse relationship of dwell times with applied voltage corresponds to a charged blocker moving through the pore (C), while having dwell times invariant with applied voltage is indicative of an uncharged blocker, which could be present as a vapor phase inside of the pore (D). The linear relationship between the PBC and applied voltage in both cases indicates that the blocked current is carried by charged species. These charged species are believed to be protons In the SWNT nanopore case[19] and electrolyte ions in the PDMS case.

To further confirm the existence of a phase transition as the cause of stochastic current fluctuations, we sought out a theory from the literature that offered predictive estimates of the pore-blocking currents and dwell times. Palmeri et al.[61] have developed a model using variational field theory that predicts phase transitions to occur for electrolyte solutions confined to neutral and weakly charged cylindrical nanopores. Their model considers the diameter of the pore, the dielectric constants of the solution and pore walls, surface charge on the pore walls, the effective Donnan potential inside the pore, and bulk ionic concentration. The major assumptions of Palmeri's model are as follows: 1) a perfectly cylindrical pore surface, 2) uniform surface charge density, 3) constant electrostatic potential inside the pore, and 4) no steric effects of ions (ions act as point charges). In reality, the pores studied here are non-cylindrical, may not have uniform charge density along the length of the pore, the electrostatic potential is not constant as we are applying a voltage across the pore, and ion size may indeed have significant effects at the nanoscale; thus while we can compare experiment and theory, one would not expect numerically equivalent results. Their model predicts that at low enough pore diameters, there exists a bulk electrolyte concentration around which the partition coefficient exhibits an abrupt change, where the partition coefficient is defined as $k = \frac{\langle \rho \rangle}{\rho_b}$, where $\langle \rho \rangle$ is the average ionic concentration inside the pore (mol/L) and ρ_b is the bulk ionic concentration (mol/L). Thus, there exists a high conductivity liquid (L) phase and a low conductivity vapor (V) phase. If the stochastic current fluctuations are due to fluctuating between these V and L phases, the difference in partition coefficients provides a way to estimate the magnitude of pore-blocking currents, given an applied voltage and pore length, using

(9) $\langle \rho \rangle = \rho_b (k_L - k_V)$

(10) $\Delta I = I_+ + I_- = (J_+ + J_-) \cdot A = q \cdot \langle \rho \rangle \cdot v_{avg} \cdot A = q \cdot \langle \rho \rangle \cdot (\mu_+ + \mu_-) \cdot E \cdot A$

$$(11)\ \Delta I = q \cdot \rho_b \left(k_L - k_V\right) \cdot \left(\mu_+ + \mu_-\right) \cdot \frac{\Delta V}{L} \cdot A$$

where k_L and k_V are the partition coefficients of the liquid and vapor phases, resp., ΔI is the predicted pore-blocking current (A), I_+ and I_- are the currents associated with positive and negative ions (A), J_+ and J_- are the current densities (A/m^2), A is the pore cross-sectional area (m^2), v_{avg} is the average velocity of the ions (m/s), μ_+ and μ_- are the ion mobilities of the cations and anions, resp. (m^2/V-s), E is the electric field across the pore (V/m), ΔV is the voltage applied across the pore (V), and L is the length of the pore (m). The area of the pore is given by

$$(12)\ A = f \cdot \pi \cdot a^2$$

where a is the radius of the nanopore (m), and f is some factor that accounts for the non-cylindrical shape of the pore which is unknown. It is possible that the pore may be a wide slit-shaped pore, for example. The model predicts a difference in partition coefficients, Δk, roughly from 0-0.15 for neutral nanopores, which changes slightly depending on the bulk concentration, pore diameter, and surface charge. The diameter distribution of samples tested for this study were presented earlier in Figure 16B, assuming a cylindrical pore (f = 1) and Δk = 0.15.

To compare with our experiments, we used ρ_b = 0.1M, a = 1nm, $\mu_+ = \mu_{Na^+}$ = 51.9x10^{-9} m^2/V-s, $\mu_+ = \mu_{Cl^-}$ = 79.1x10^{-9} m^2/V-s, ΔV =1.0 V, and L = 170 nm to get an envelope of predicted pore-blocking currents. The predicted pore-blocking current has a maximum value around 40-120 pA depending on the value of f used, where f is a factor accounting for non-circular pore cross-sections (f = 1 for circular cross-section). In Figure 20A-B, we compared these predicted pore-blocking currents with experiments made under similar conditions (ρ_b = 0.1M NaCl, ΔV =1.0 V, and L = 170 nm) and find very good agreement for low values of f < 3.

The model also predicts the thermodynamic stability of each phase in a region of coexistence. Over small differences in surface charge, there is predicted to be a wide range of ratios of residence times (τ_L / τ_V), that is, the time spent in the high-conducting state versus the time spent in the low-conducting state. For the particular example presented in their study (ρ_b =1mol/L, a = 0.617 nm), it

was predicted that as the surface charge varied from 6.5-7.5 x 10^{-4} C/m^2, the τ_L / τ_V varied roughly from 0.01 to 100, thus showing that slight deviations in surface charge, keeping ionic concentration and diameter constant, can result in significant changes in these residence time ratios. The surface charge explored in Palmeri's study is very weak (roughly 1 charge per 230 nm^2), although within the same vicinity as the surface charge for the PDMS surfaces (roughly 1 charge per 10-20 nm^2). We assume that whenever the conditions (diameter, concentration and surface charge) are such that fluctuations between a high- and low-conducting state are observed, slight deviations in any of these parameters will also result in significant sample-to-sample variation in the ratios of residence times similar to the specific case (ρ_b =1mol/L, a = 0.617 nm, σ = 6.5-7.5 x 10^{-4} C/m^2) studied by Palmeri et al[61]. It could be expected that among the samples that do demonstrate stochastic current fluctuations, there will be a distribution of actual surface charge values for each patch area so that one would expect to sample from the wide range of possible residence time ratios. Figure 20 shows that experimentally, the high-conducting state can occur more often or less often by factors as high as 25, in line with the qualitative predictions by the model. It should be noted that at very high or very low τ_L / τ_V ratios, it would be difficult to realize that rare stochastic current fluctuations were actually occurring as opposed to random, rare noise artifacts. In summary, the comparisons of pore-blocking currents and residence time ratios with the model proposed by Palmeri et al.,[62] along with dwell times that are invariant with applied voltage, provide evidence that the observed stochastic current fluctuations are due to switching between high-conducting liquid and low-conducting vapor phases.

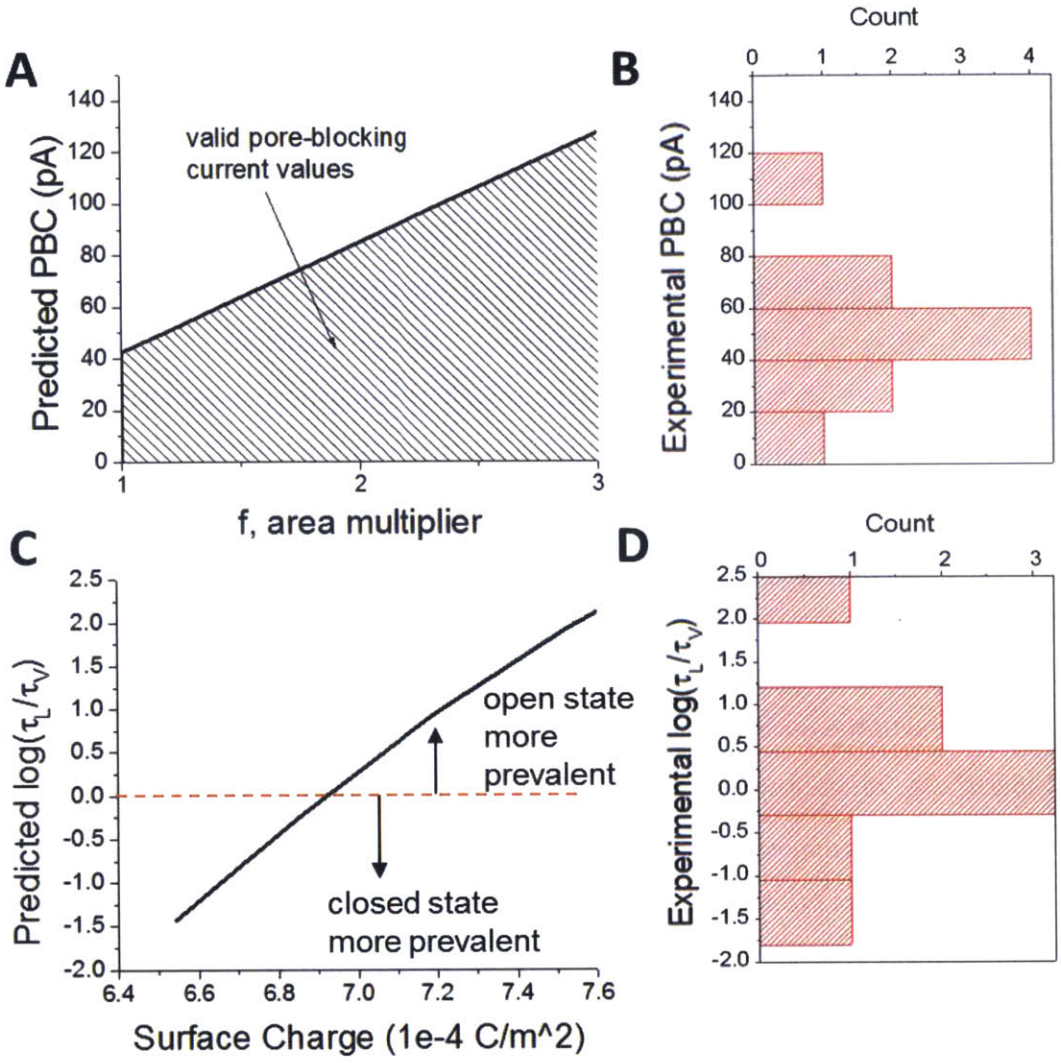

Figure 20. (A) Predicted log of the ratio of residence times in the liquid and vapor states versus area factor accounting for deviation from a cylindrical pore model according to the model proposed by Palmeri et al.[61] (B) The wide range of possible residence time ratios is reflected in the experimental data, where if fluctuations are observed, there is a wide range of residence time ratios. (C) The model also predicts an envelope of pore-blocking currents (PBC), which varies depending on the deviation from a circular pore cross-section. (D) The experimental pore-blocking currents fall within this envelope for f < 3.

However, it is acknowledged that there are some possible drawbacks of applying this model to the PDMS nanopores. For example, the model considers a pore in thermal and chemical equilibrium with the bulk, and it is assumed in the model derivation that the Donnan potential is constant within the pore. However, the applied voltage ensures that the system is not in equilibrium and the potential across the pore is not uniformly varying. It is unclear if the qualitative results of the model hold under these conditions. Furthermore, the model predicts that the bulk concentration at which

phase coexistence occurs varies inversely with the pore radius. Thus, one would expect that if the pore diameter remains constant, there would be only one bulk concentration where fluctuations are observed; in actuality, there is a wide range of ionic concentrations where fluctuations are observed for a single patch. It is possible that the pore geometry is non-cylindrical, resulting in different sections of the pore of varying dimensions which are active depending on the bulk concentration. Further experiments with well-defined pores and surface charge are needed to more completely confirm the existence of liquid/vapor transitions as the cause of stochastic fluctuations in these types of pores.

Experiments varying the temperature of the system were performed to confirm whether a phase transition was occurring, but the results were inconclusive. Theories that assert that stochastic fluctuations occur at the phase boundary between high and low conducting states as a first-order transition suggest that increasing the temperature and keeping all other parameters constant should halt the fluctuations. As one moves into the single phase region, for example, either the high or low conductance state should persist. However, stochastic events were observed as the temperature was steadily ramped from room temperature up to 42-62°C in three trials; eight other trials showed no events at all through the temperature increase. In one case, the events disappeared above 60°C, although this occurred just before the bath solution evaporated. The other two cases did not go above 42°C and 57°C, and events persisted from room temperature through the maximum temperature. The pore-blocking current is not well-correlated with temperature; this may be due to the fact that changing temperature has other effects such as changing the pore size, solution viscosity, solution concentration through evaporation, surface charge, etc. It is possible that as the temperature changes, the changing pore geometry and solution conditions allow it to remain on or otherwise traverse the phase coexistence curve. Carefully controlled temperature experiments will be needed to fully verify the presence of phase transitions in these systems.

In attempts to further characterize the shape of these PDMS nanopores, we introduced $[Ru(bpy)_3]^{2+}$ (1.2nm in diameter) to the system. Among other uses, this molecule is often employed as a probe molecule for transport measurements to determine steric selectivity in pores commensurate in size

to its diameter. However, upon addition of this molecule in concentrations >$5x10^{-8}$M there is reduction in overall conductance, and for concentrations >$1x10^{-4}$M, there is complete shutdown of any ionic transport even though relatively high concentrations of NaCl (0.1M) still exist in the pipette tip and bath, as Figure 21 demonstrates. If $[Ru(bpy)_3]^{2+}$ is added to just one side, we find a shutdown of both pore and leakage conductances if the polarity of the applied voltage is such that the $[Ru(bpy)_3]^{2+}$ ion is driven toward the pipette tip/PDMS interface containing the nanopores. These results strongly suggest that for relatively hydrophobic pores of nanometer-sized dimensions, one can have $[Ru(bpy)_3]^{2+}$ physisorbed on the interior of the pore, thus blocking overall transport. Further experiments performed demonstrated the reversibility and reproducibility of this $[Ru(bpy)_3]^{2+}$ physisorption.

The model proposed by Palmeri suggests that the presence of divalent cations would decrease the negative surface charge inside of the pore, which would cause the nanopore to switch from a high-conducting to a low-conducting state. As mentioned before, Palmeri's model assumes ions behave as point charges, with only Coulombic interactions present between ions. $[Ru(bpy)_3]^{2+}$, however, is approximately 1.2nm in diameter, and thus it cannot shield surface charge as effectively as Mg^{2+}, for example. Furthermore, there are significant van der Waals and dipole-dipole interactions present in $[Ru(bpy)_3]^{2+}$ that are not accounted for by the model. From our observations, it seems most likely that this ruthenium complex is adsorbing onto the inside of the pore, and at sufficient concentrations, completely blocks current through the pore. The conclusion from this set of experiments is that careful analysis is needed to ensure that transport results using probe molecules such as $[Ru(bpy)_3]^{2+}$ are not due to pore blockage caused by condensation and physisorption, especially in nanometer-scale hydrophobic pores.

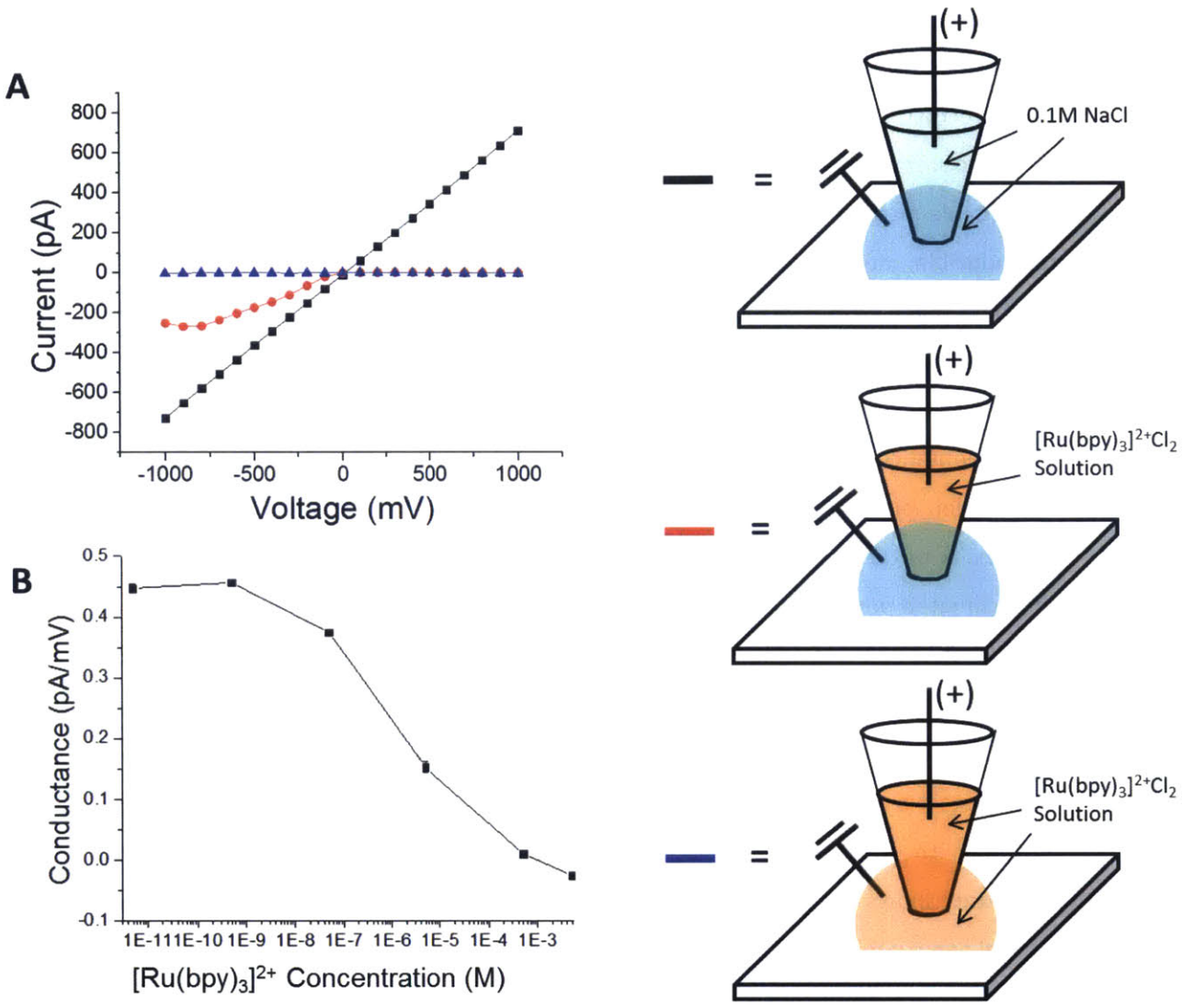

Figure 21. (A) Experimental IV curves showing that a simple electrolyte solution (0.1M NaCl) in the pipette tip and bath results in a linear IV curve, while addition of 50mM $[Ru(bpy)_3]^{2+}$ to the salt solution to one side of the bath causes complete current shutdown when the polarity is such that the $[Ru(bpy)_3]^{2+}$ ion is driven toward the pore, and complete current blockage is observed when $[Ru(bpy)_3]^{2+}$ is added to the salt solution on both sides at sufficient concentrations. (B) The overall conductance as a function of $[Ru(bpy)_3]^{2+}$ concentration. Conductance begins to decrease starting at $5x10^{-8}$M $[Ru(bpy)_3]^{2+}$. Hence, the absence of conductance of this organometallic ion is not, itself, proof of steric rejection from a hydrophobic nanopore.

4.4 Conclusions

To summarize, we study a unique, stochastic phenomenon in both grooved and flat PDMS substrates that would not be expected to have any analog to biological ion channels for which patch clamp techniques are normally used. This phenomenon was studied in depth to show the presence of nanopores formed at the interface of PDMS and glass when a patch is formed which imparts deformable properties to the pore. Transport through PDMS nanopores was confirmed by observing reproducible, multiple current states when patching onto grooved PDMS surfaces. The mechanism for these fluctuations is compared to Coulter blocking by ions in single-walled carbon nanotubes and nanoprecipitation, showing that the mechanism is fundamentally different. We compared our results with a model in the literature that predicts the coexistence of two phases at normal experimental conditions. Comparisons of the pore-blocking currents and residence time ratios with the model, along with the invariant nature of dwell times with applied voltage, suggest the plausibility of the mechanism being stochastic phase transitions inside the nanopore. Furthermore, the estimated pore diameter (ranging from 0.6-11.2 nm, depending on the calculation method) and surface charge (-0.015 C/m2) are in line with those considered by the proposed model. In this study we have demonstrated a simple method for creating deformable, interfacial nanopores, with a potential application being the creation of arrays of deformable, yet well-defined nanopores which could detect a variety of differently-sized molecules, as opposed to having a single, static nanopore. Secondly, the observation of ionic fluid phase transitions in these less well-defined nanopore structures shows the possibility of experimentally observing phase transitions in other interesting natural and synthetic porous systems, such as rocks and concrete. Finally, we have evaluated several potential mechanisms of stochastic pore-blocking in nanopores, including phase transitions, Coulter blocking, and nanoprecipitation—these experiments will be useful for characterizing future nanopore systems.

5. Raman Spectroscopic Monitoring of Phase Transitions and Filling in Single, Isolated Carbon Nanotubes

5.1 Introduction

Fluid confined inside carbon nanotube (CNT) nanopores is of significant interest for potential nanofluidic applications. CNTs are straight-line, atomically smooth nanopores ranging between 0.7 nm and 2 nm in diameter for single-walled carbon nanotubes (SWNT) and up to hundreds of nm in diameter for multi-walled carbon nanotubes (MWNT). The precise size of the CNT nanopore, enhanced slip flow at the CNT walls, and the ability to functionalize the end groups of the nanotube can possibly allow it to be used as an efficient membrane material—allowing both high fluxes and high selectivity.[16, 18] Drug delivery using carbon nantoubes is another exciting space, as carbon nanotubes can have high inner volume and can be easily taken up by cells.[29] However, knowledge of the conditions for loading and unloading are not well studied. Carbon nanotubes have also been considered for use as nanoreactors,[65] although the effect of confinement on the energy of reactants and products and kinetics of the reaction are not well understood.

Several groups have used molecular dynamics (MD) simulations to study the transport and thermodynamics of fluids, mainly water, inside of carbon nanotubes.[23, 64, 66-68] Pascal and co-workers used MD simulations to show that spontaneous water filling occurs inside carbon nanotubes across a diameter range from 0.8 to 2.8 nm. Further, they elucidate different regimes where water is stabilized mainly by entropy (0.8-1.0 nm and >1.4 nm) or enthalpy (1.1-1.2 nm).[69] MD simulations have demonstrated freezing transitions of water inside carbon nanotubes between 0.9 and 1.7 nm in diameter, showing highly non-monotonic freezing points with nanotube size.[68]

Early experimental studies on carbon nanotubes confirmed the possibility of filling carbon nanotubes with metals, as confirmed by TEM.[70-71] The filling of water inside carbon nanotubes has been explored in bulk quantities of nanotubes of mixed chirality using Raman spectroscopy.[72] Water phase transitions have also been observed on bulk nanotube samples neutron scattering[73], x-ray diffraction[74], and NMR[75]. The goal of this work is to extend these analytical techniques down to the single-nanotube level to precisely probe filling and phase behavior of materials inside an individual, isolated carbon nanotube.

Raman spectroscopy is an especially useful technique for analyzing carbon nanotubes, as carbon nanotubes are very strong Raman scatterers, allowing observation of single, isolated nanotubes.[36] Raman spectroscopy measures the vibrational modes of carbon nanotubes in the longitudinal, transverse and radial directions. The radial vibrational mode, termed the radial breathing mode (RBM), would be expected to be significantly affected upon interior filling of the carbon nanotube. And if that material undergoes a phase transition, the coupling to the carbon nanotube wall should change, resulting in a shift in the RBM.

5.2 Experimental

5.2.1 Device Fabrication

To fabricate the device, fiducial markers are placed on a silicon wafer using photolithography and e-beam evaporation, creating TiO_2-SiO_2 markers spaced 200 μm apart. Small rectangular pieces are cut using a diesaw (9 mm x 14 mm). The catalyst to grow ultra-long carbon nanotubes (CNTs) is a solution of 2 wt% sodium cholate-SWNT containing residual iron nanoparticles which act as the catalyst. A thin strip of the catalyst solution is placed on the edge of the silicon substrate. Ultralong, horizontally-aligned carbon nantoubes are grown using a chemical vapor deposition (CVD) process described previously.[19]

After CNT growth, an SEM map (JEOL SEM 6060, 1.2kV accelerating voltage) is taken of the entire surface to map out the locations of nanotubes relative to the markers. A thin PDMS sheet is cut and placed on top of the substrate in the middle. We then oxygen plasma etch the device (Harrick Plasma Cleaner PDC-32G, 3 min, low power) to etch away the exposed parts of the carbon nanotubes (not covered by the PDMS layer) and open up the nanotube ends. The PDMS layer is carefully peeled off, and SEM confirms that the nanotube has been etched up until where the PDMS layer was. Under some circumstances, the PDMS can peel the carbon nanotubes from the surface, indicative that the PDMS has a higher surface energy than the silicon surface. Experimentally, we found that thicker (~2 mm thick), fully cured (70C for 24 hr) PDMS pieces worked better at leaving the CNT on the silicon surface. Also, cleaning the PDMS piece with Scotch tape beforehand can

make the PDMS too sticky and result in CNT removal—thus, clean preparation of PDMS is required to make this cleaning step unnecessary.

PDMS reservoirs were created by preparing a roughly 1-2 mm thick PDMS layer using Sylgard 184 in a 10:1 ratio of elastomer to curing agent. A knife was used to cut out small, rectangular reservoirs. A PDMS "glue" mixture was also prepared using a 3:1 ratio of elastomer to curing agent—increasing the relative concentration of curing agent increases the cross-linking density and allows better conformation around smaller features, such as CNTs.[76] The PDMS "glue" was degassed for 5 minutes and spin-coated on a glass slide for 45 seconds at 3000 rpm. The PDMS reservoirs were cleaned with Scotch tape and placed onto the thin layer of PDMS glue. The reservoirs were then picked up and placed on the silicon substrate such that the opened ends of the nanotubes were in the middle of the reservoirs. The PDMS glue was cured in an oven at atmospheric pressure at 70°C for at least 3 hours.

Upon completion, there were several opened nanotubes spanning the reservoirs, with the separation in the two reservoirs allowing one to perform Raman spectroscopy while the reservoirs are filled with fluids. A Horiba LabRAM equipped with a 532 nm excitation laser was used to collect Raman spectra on the individual nanotubes. All spectra acquisition used the following conditions: 532nm excitation laser, a 100x super long working distance objective (WD 7.6 mm, N.A. 0.6), 500 μm confocal hole, 100 μm slit width, 1800 grooves/mm grating. Prior to each use, the Raman instrument was calibrated using cyclohexane which has a dominant peak at 801.8 cm^{-1}. Comparing SEM images with the video images on the microscope, a single nanotube could be located on the Raman microscope. It should be noted that the tube must be aligned parallel to the direction of laser polarization, or else no Raman signal will be observed.

After it was confirmed that external water does not affect the vibrational RBM spectrum, the PDMS reservoirs were not added to subsequent devices. For these cases, the sample was prepared by etching the ends of the nanotube. The etched portion of the silicon oxide surface is very hydrophilic, so water added to near the ends of the tube wet up to the edge of the etched nanotube region.

The temperature experiments used a separate, temperature-controlled environmental stage (Linkam THMS350EV) which has a theoretical range of -196 to 350°C. Under our experimental conditions (stage opened to the environment), however, the lower temperature limit is only around

-80°C. The device was secured to the heating/cooling stage and left open to the environment, since taking Raman spectra through a quartz window dramatically decreased the Raman intensity. To prevent water condensation during cooling, nitrogen flowed through the chamber. A very thin thermocouple was placed in one of the device reservoirs, and temperature readings at the surface of the device were found to be within 1-2 degrees Celsius of that measured at the silver heating/cooling stage. All subsequent temperature measurements correspond with the measured stage temperature unless otherwise indicated.

Variable laser power experiments were performed by mounting a variable neutral density filter (Thorlabs NDC-50C-2) in front of the 532nm laser. The actual laser power at the sample was measured using a digital power meter (Thorlabs PM100D).

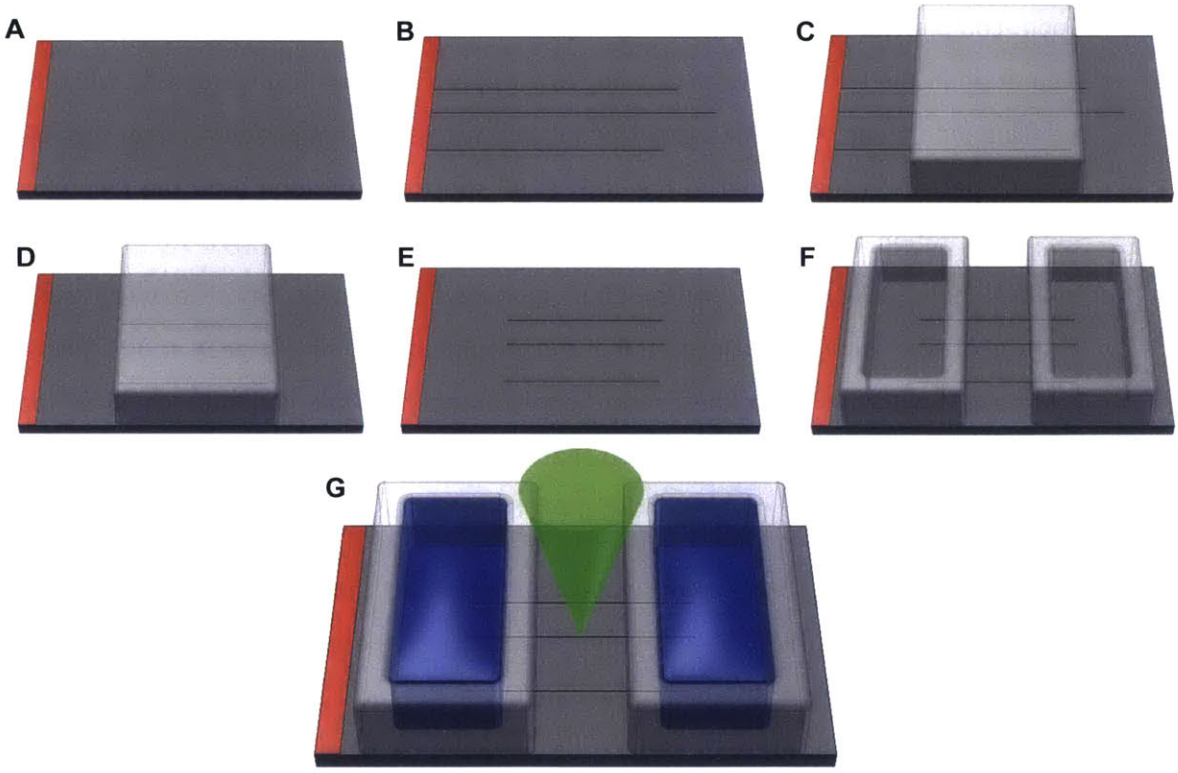

Figure 22. Device fabrication procedure. (A) A catalyst solution consisting of iron nanoparticles (red) is deposited along a side of the silicon substrate. (B) Ultralong, horizontally-aligned carbon nanotubes are grown using a CVD process. (C) A PDMS block is placed in the middle of the silicon substrate. (D) Oxygen plasma etching removes the uncovered parts of the nanotubes and opens up the ends. (E) The PDMS block is removed. (F) Two reservoirs are cut out of PDMS and adhered to the surface using PDMS glue, followed by curing. (G) During the experiment, the reservoirs are filled with a solution, and Raman spectroscopy is performed on a CNT region between the two filled reservoirs.

5.2.2 Peak Fitting and Analysis

Raman spectra were deconvoluted using single or multiple Lorentzian peaks. In some cases, the RBM are made up of several peaks, indicative of multiple possible phases present inside the nanotube. In order to determine the optimal number of peaks to fit, each spectrum was fit using 1, 2 and 3 peaks as shown in Figure 23. The peak fitting scenario to use was determined by computing the sum-squared error for each fit. If the relative improvement in sum-squared error by adding another peak was >30%, then that peak was included.

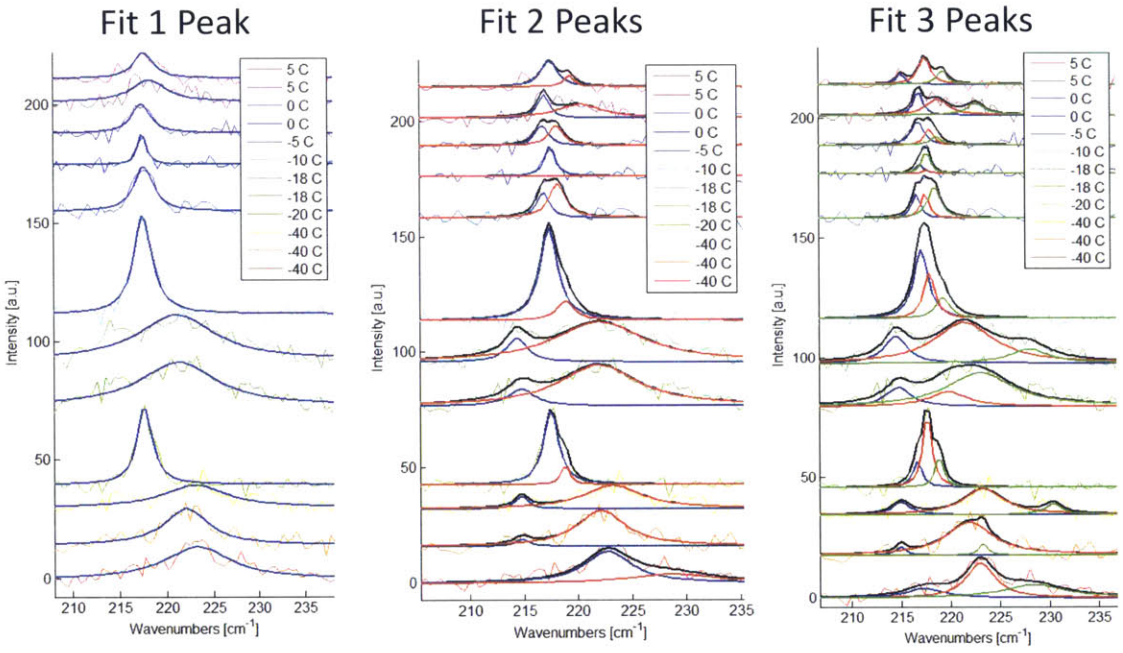

Figure 23. Raman peak fitting analysis. For each spectrum, 1, 2 and 3 peaks are fit to the data. The peak fitting scenario used for each spectrum is based on the relative improvement to the overall fit by the addition of another peak.

5.3 Results and Discussion

5.3.1 Raman Characterization of CNT

Although several tubes (10-20) may span the reservoirs, not all are available for study. Nanotubes are located by scanning the laser perpendicular to the direction of the nanotube and searching for a G peak. If a G peak is found, a full spectrum is acquired between 100-1800 cm^{-1} to obtain the RBM, D and G peaks. Because only certain tube chiralities are resonant with the 532nm excitation source, approximately a quarter of the tubes will have strong G peaks. Even if a tube has a strong G peak, only about a quarter are observed to have strong RBMs. Thus, a fabricated device usually has only zero to two tubes with strong RBMs to carry out the filling and phase transition experiments.

Once an RBM was found, its diameter was calculated using the following relationship:[38]

$$(13)\ d[nm] = \frac{248}{RBM[cm^{-1}]}$$

The metallicity of the tube was determined from the shape of the G peak.[40] Table 3 provides the details of the tubes used in this study. In the case of devices E23 and F05, two RBMs were actually observed in the same spot, which either suggests a DWNT or two SWNT grown side-by-side. It should be noted that it is difficult to definitively determine if a tube is a SWNT or DWNT purely from Raman spectroscopy, as tubes may be present of different chiralities that are not resonant with the excitation source. The second RBMs for devices E23 and F05 did not shift significantly during the experiments. Figure 24 uses VMD to illustrate the two RBMs in a double-walled tube configuration, showing the possibility that the larger tube is actually the outer tube in a DWNT. This description could also explain why no significant RBM shifts were observed for the larger nanotube.

Table 3. Devices studied and corresponding nanotube properties.

Empty CNT RBM [cm^{-1}]	CNT Diameter [nm]	CNT Metallicity	Notes
235	1.05	Metallic	
234.2	1.06	Semiconducting	2nd RBM at 160.3 cm^{-1} (1.55 nm)
216.1	1.15	Semiconducting	2nd RBM at 130.8 cm^{-1} (1.90 nm)
199.3	1.24	Semiconducting	
162.9	1.52	Semiconducting	2nd RBM at 114.1 cm^{-1} (2.17 nm)

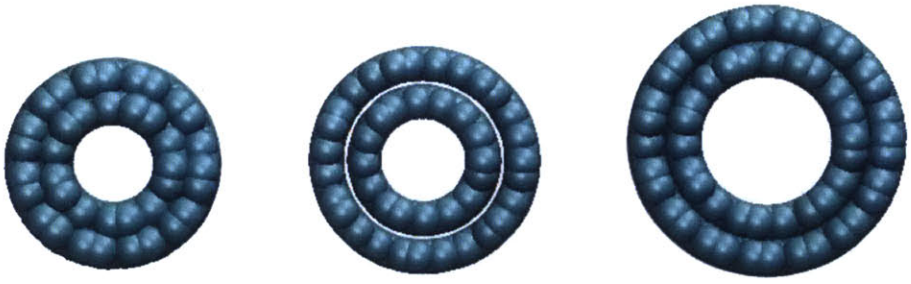

Figure 24. Devices where two RBMs were found. Modeling the CNTs in a double-walled nanotube (DWNT) configuration shows the possibility that the diameters could be consistent with a DWNT. The illustrated sphere size is based on the van der Waals radius of carbon (1.7 Angstroms).

5.3.2 Internal Filling of Individual CNTs with Water

Experiments were performed to first verify that internal water filling could be observed in Raman. We performed a time map by taking continuous Raman spectra on a single spot as a function of time. The results in Figure 25 show that the inner RBM at roughly 216 cm^{-1} undergoes a momentary upshift upon water addition to one reservoir, and then returns to its original value. Addition of water to the second reservoir causes a more prolonged, yet oscillatory shift to 218 cm^{-1}, before returning to the original peak position. The transience observed can be possibly explained by the fact that the Raman laser is heating the tube and its contents enough to vaporize the liquid water as it flows through the tube. Quantification of the amount of heating observed is discussed later.

While this experiment demonstrates that a significant RBM change occurs when water is added to the system, it does not preclude the possibility that there may be external water wetting that causes the RBM shift. In another experiment, it was verified that external water plays very little role in the RBM shift by adding water to the ends of the nanotube before and after etching. If external water caused an RBM shift, the application of water before etching would result in a shift in the RBM. Figure 26 demonstrates that the RBM upshifts only after etching and opening the ends of the nanotube and adding water to the ends. For this particular tube, the RBM remains upshifted (water remains inside the tube) even after removing water from the reservoirs.

There is still a possibility that physisorbed water is already on the nanotube under normal conditions, and the RBM is already shifted due to this physisorbed water. To test this hypothesis, the sample was heated from room temperature to 210 °C, well above the vaporization temperature for bulk water—any external water should be removed at this temperature. There was no significant shift in RBM observed from room temperature (where physisorbed water is a possibility), indicating that either there is no physisorbed water on the nanotube or the physisorbed water has no effect on the RBM of the tube. In both cases, this confirms that the shift observed from adding water to the ends of the tube is the result of internal, not external, water filling. Additionally, when the temperature was decreased such that frost visibly formed on the surface of the device, there was no significant change in the RBM compared to room temperature measurements.

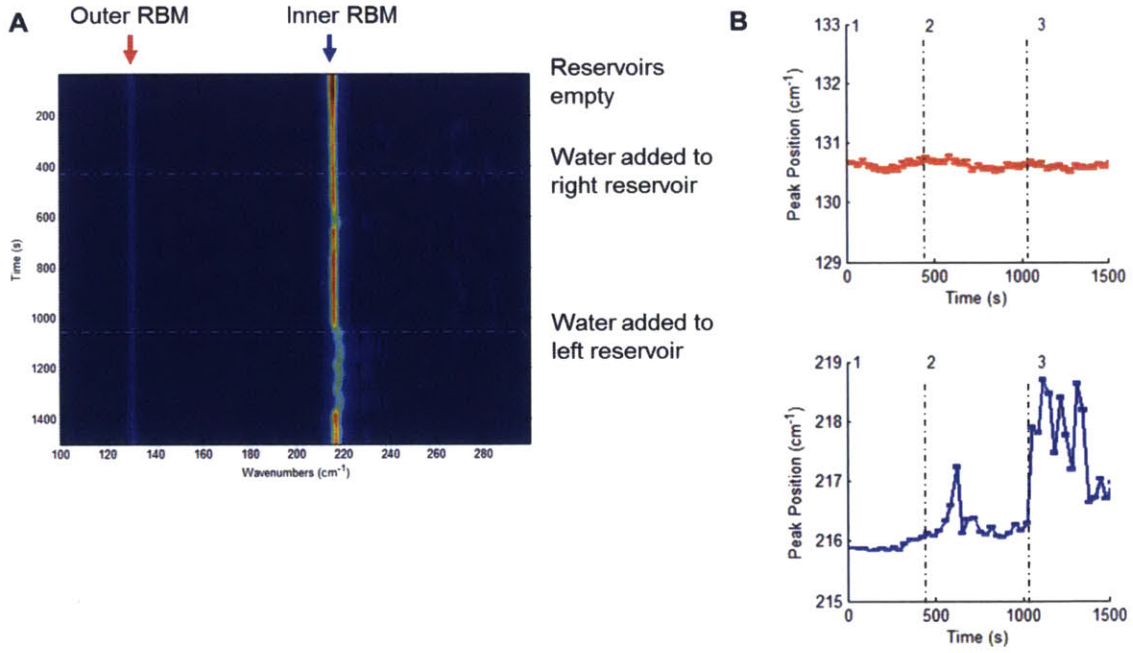

Figure 25. (A) A time map showing the RBM peak intensities as a function of time and wavenumber. Dotted white lines indicate the time points at which water is added to the reservoirs. The RBM at the lower peak position corresponds with the larger, outer CNT RBM, and the one at the higher peak position corresponds with the smaller, inner CNT RBM. (B) Fitted peak positions for the outer and inner RBMs, respectively. Time points correspond as follows: 1 = reservoirs empty, 2 = water added to right reservoir, and 3 = water added to left reservoir.

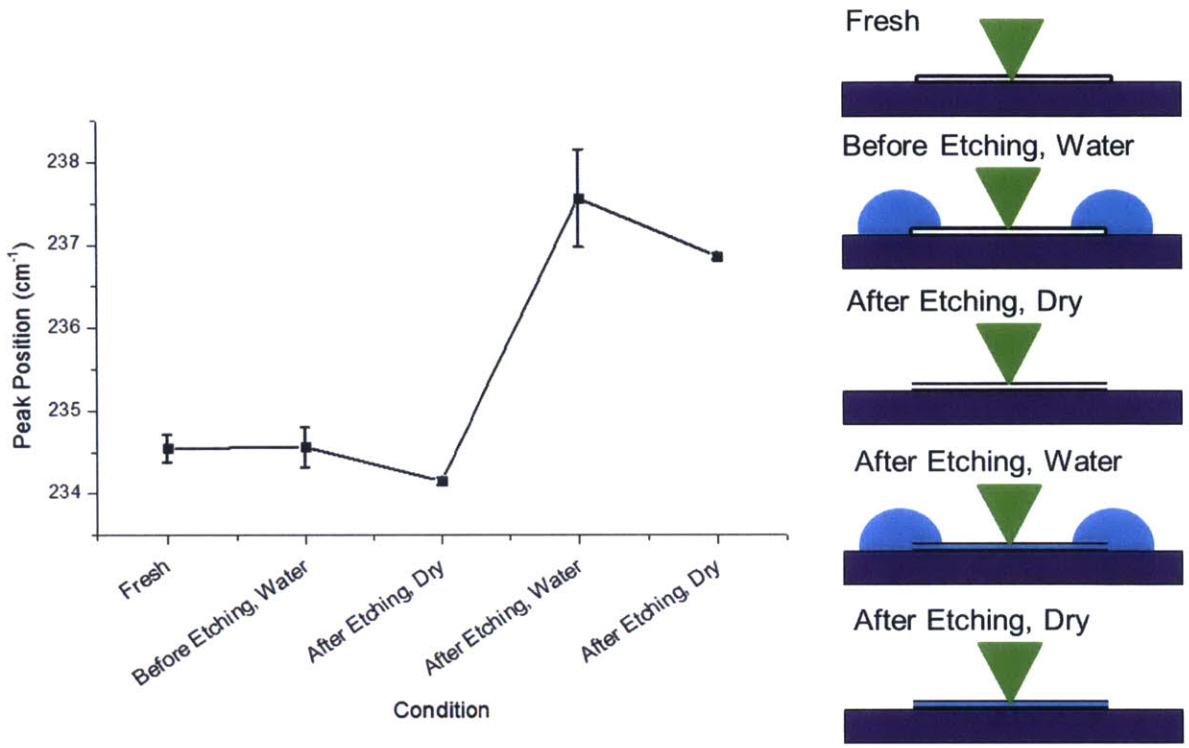

Figure 26. Experiment showing effect of adding water before and after etching. Before etching, adding water does not shift the RBM. Only after opening the ends of the nanotube and adding water to the ends does the RBM shift.

5.3.3 Removal of Water from Interior of CNT

The conditions for emptying water-filled tubes were found to vary significantly between devices and from day-to-day. For one tube (1.15 nm), just removing the bulk water from the surface with a pipette was enough to empty the tube. For another device (1.06 nm), removing bulk water was not enough to empty the tube. Only after heating at 210°C/20 minutes did the tube empty. Upon subsequent water filling, the tube could not be emptied at 210°C/20 minutes; instead, annealing in a tube furnace under a nitrogen atmosphere at 900C/1hr was able to empty the entire tube. For a third tube (1.24 nm), the tube would not empty up to 350°C, although placing overnight in a vacuum desiccator emptied the tube.

5.3.4 Laser Heating Effects

An important consideration while performing these Raman experiments on individual tubes is the effect of laser heating. Since the laser is focused on a small spot around 2 μm in diameter, local heating can occur, such that the local temperature of the tube being probed is significantly higher than the bulk sample temperature set by the stage. To accurately record the temperature at which phase transitions occur, it is necessary to use this local temperature. During laser illumination, the CNT G peak shifts a certain amount, which is proportional to the local temperature change. For each device, the following parameters can be obtained: the G peak shift versus temperature (X), and the G peak shift versus laser power (β). These measured parameters are important in subsequent phase transition experiments.

A simple model is derived that relates the extent of laser heating to carbon nanotube thermal properties, such as axial thermal conductivity and the heat transfer coefficient between the carbon nanotube and silicon substrate. We consistently observe that the nanotube thermal conductivity decreases upon water filling compared to an empty tube.

G Peak Shift -Temperature Calibration Curve

Previous studies have reported that the shift in the G+ Raman peak of the nanotube varies linearly with temperature.[77-79] Thus, we can create a calibration curve showing the shift in G+ peak with stage temperature, where the stage temperature is well-approximated to be the nanotube temperature when the laser power is very low. For a 2μm spot size and 0.21 mW laser power at the objective, the laser power density on the sample was below 67 W/mm^2. Decreasing the laser power further did not appear to have a significant effect on G peak position, indicating that the laser was not heating the tube appreciably below this power level. Figure 27 gives an example of a G peak-temperature calibration curve for one tube (1.15 nm diameter). The slope of the calibration curve is $\mathrm{X} = \left(\frac{\partial G}{\partial T}\right)_{P_{laser}\sim 0}$.

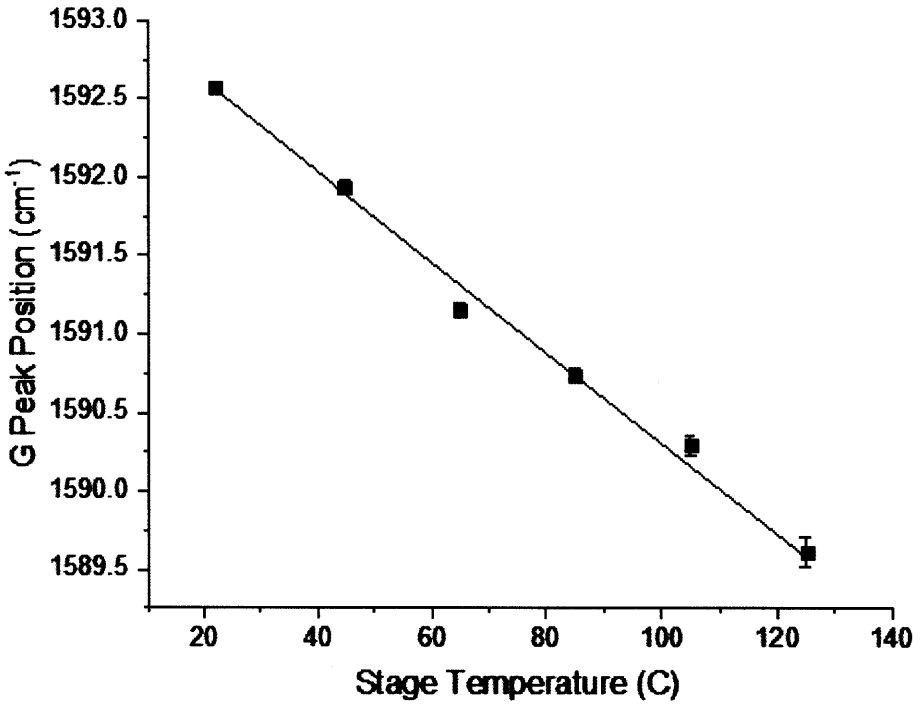

Figure 27. Example calibration curve for G+ peak position versus stage temperature at laser powers low enough to produce negligible local heating.

Table 4. Nanotubes with experimentally determined X = dG^+/dT [cm^{-1}/K]. (Note: this parameter was not measured for the 1.05 nm nanotube)

Nanotube Diameter [nm]	X [cm^{-1}/K]	Error in X [cm^{-1}/K]
1.06	-2.895×10^{-2}	1.14×10^{-3}
1.15	-3.147×10^{-2}	1.93×10^{-3}
1.24	-1.309×10^{-2}	8.58×10^{-4}
1.52	-4.847×10^{-2}	5.96×10^{-3}
1.63	-2.483×10^{-2}	1.77×10^{-3}

G Peak Shift – Laser Power Calibration Curve

Changing the laser power shifts the G+ peak as well, indicating a change in temperature.[78] Figure 28 illustrates this phenomenon for a 1.15 nm diameter tube. The slope of this line is $\beta = \left(\frac{\partial G}{\partial P_{laser}} \right)_{T=20C}$. The local temperature can be calculated using the actual laser power:

$$(14)\, T_{actual} = T_{stage} + \frac{\beta}{X} \cdot P_{laser}$$

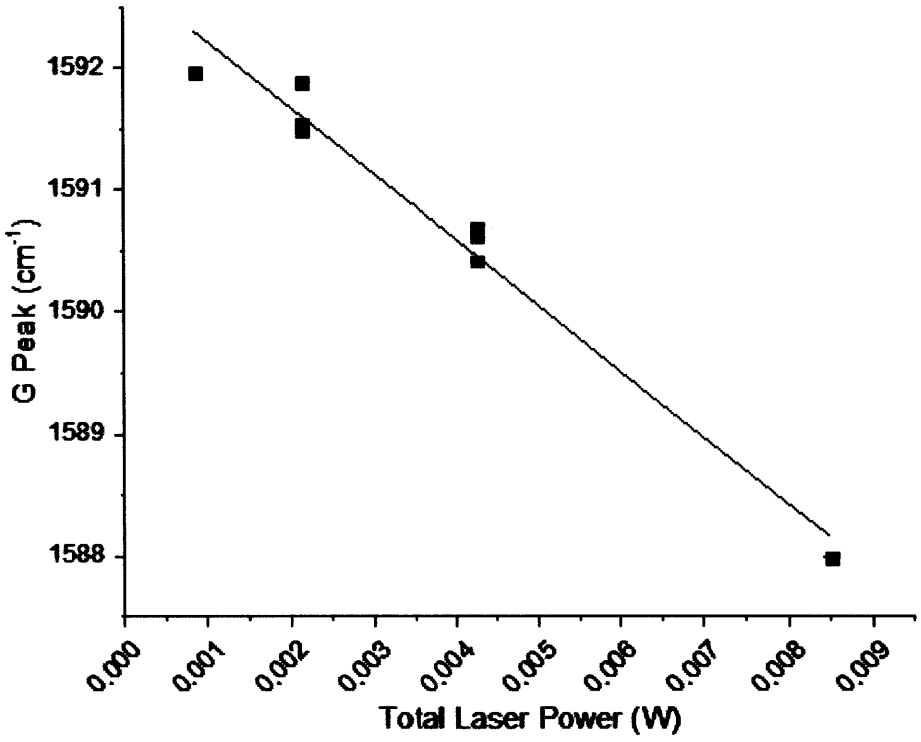

Figure 28. G+ peak position versus total laser power for a 1.15 nm diameter tube. Increasing laser power reduces the G peak position, indicating a local temperature increase.

Laser Heating Model of Carbon Nanotubes

To understand this laser heating effect more closely, we derived a simple model for laser heating of a carbon nanotube on a silicon substrate, as illustrated in the energy balance model used in Figure 29. The time-dependent energy balance for a differential nanotube element can be written as follows to include heating by the laser, conduction along the nanotube and heat transfer to the silicon substrate:

(15)

$$\left(\pi R^2 \Delta y\right)\rho C_p \frac{\partial T(y,t)}{\partial t} =$$
$$q_{laser}\alpha_{CNT,\lambda} 2R\Delta y + h_{CNT-Si} 2R\Delta y\left(T_{Si} - T(y,t)\right) + k_{CNT,axial}\left(T\left(y+\Delta y\right) - T\left(y\right)\right)\pi R^2 + k_{CNT,axial}\left(T\left(y-\Delta y\right) - T\left(y\right)\right)\pi R^2$$

Rearranging this equation, one arrives at:

(16)

$$\rho C_p \frac{\partial T(y,t)}{\partial t} = \frac{2\alpha_{CNT,\lambda} q_{laser}(y)}{\pi R} + \frac{2h_{CNT-Si}\left(T_{Si} - T(y,t)\right)}{\pi R} + k_{CNT,axial}\left(\frac{T\left(y+\Delta y\right) - 2T\left(y\right) + T\left(y-\Delta y\right)}{\Delta y^2}\right)$$

Taking the limit as Δy goes to zero, we obtain the final differential equation with the following boundary conditions: 1) $T(y,t=0) = T_{stage}$, 2) $\frac{\partial T}{\partial y}(y=0) = 0$, and 3) $T(y \to \infty) = T_{stage}$.

(17) $$\rho C_p \frac{\partial T(y,t)}{\partial t} = \frac{2\alpha_{CNT,\lambda} q_{laser}(y)}{\pi R} + \frac{2h_{CNT-Si}\left(T_{Si} - T(y,t)\right)}{\pi R} + k_{CNT,axial}\frac{\partial^2 T(y,t)}{\partial y^2}$$

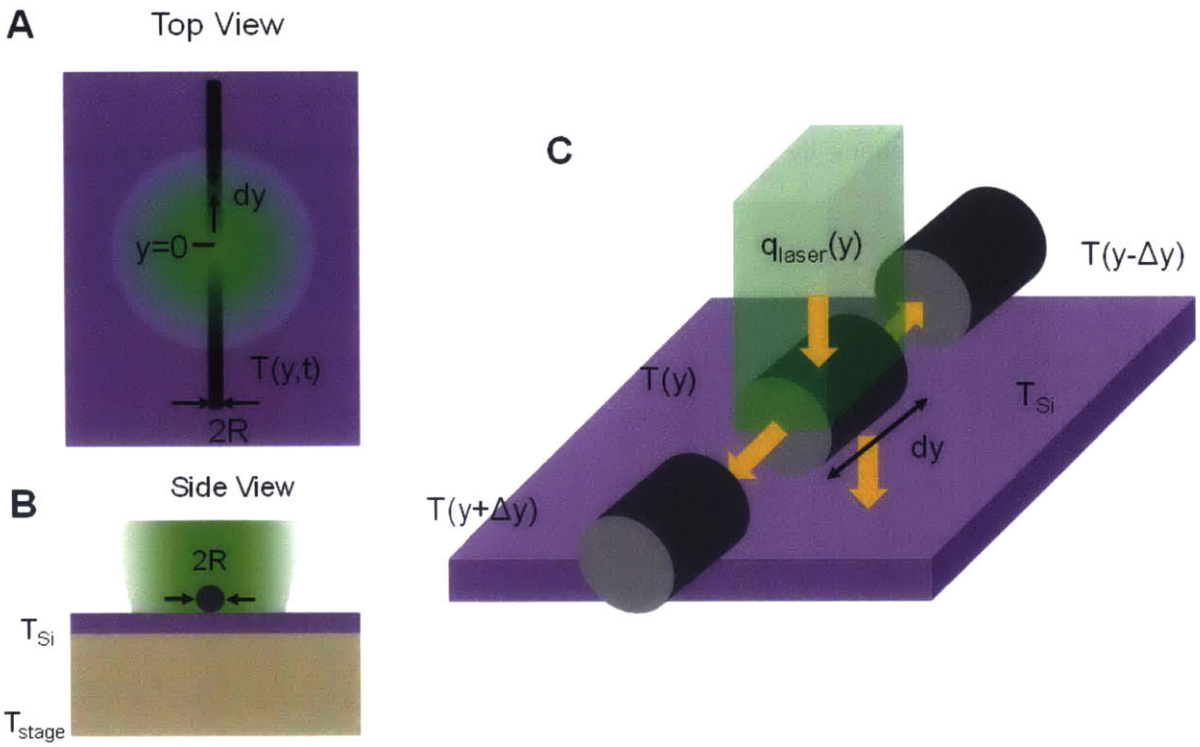

Figure 29. Schematic of model for laser heating of carbon nanotube on a silicon substrate. (A) In the experiment, a laser is focused on one spot along the length of the tube. This position is defined to be y = 0 in the model. (B) The silicon substrate in the experiment is lying on top of a silver heating stage. The temperature of the silicon, T_{Si}, is assumed to be the same as T_{stage}. (C) The energy balance for a differential element of the tube. Heating from the laser beam is dissipated through conduction along the nanotube and through heat transfer to the silicon substrate.

Table 5. Symbol definitions for model describing laser heating of carbon nanotube.

Symbol	Description	Units
R	CNT radius	m
T(y,t)	CNT temperature	K
y	Position along CNT, y=0 at center of laser	m
T_{Si}	Temperature of silicon wafer surface	K
T_{stage}	Temperature of stage	K
$q_{laser}(y)$	Power density of laser at position y	W/m^2
$\alpha_{CNT,\lambda}$	Absorption of light at wavelength λ by CNT	fraction
$k_{CNT,axial}$	Thermal conductivity of CNT in axial direction	W/m-K
h_{CNT-Si}	Heat transfer coefficient between CNT and Si surface, based on projected area of CNT on Si	W/m^2-K
ρ_{CNT}	Density of CNT (filled or unfilled)	kg/m^3
$C_{p,CNT}$	Specific heat of CNT (filled or unfilled)	J/kg-K

Laser heating has been experimentally shown to reach steady-state fairly quickly, as shown in Figure 30. Most of the temperature increase occurs within the first couple seconds, and given that typical spectra are taken with total exposure times between 80-240 seconds, the steady-state assumption can be assumed. Eq. (18) gives the differential equation for the steady-state case.

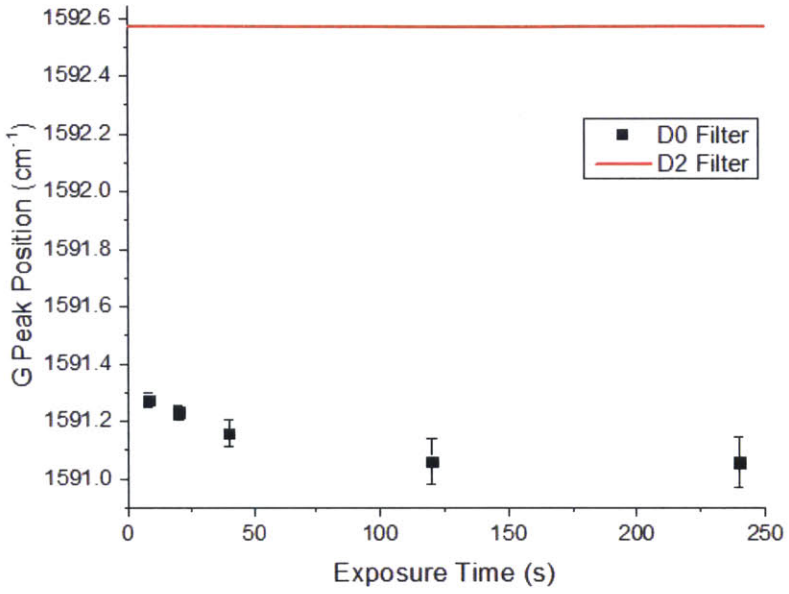

Figure 30. Experimental transient heating experiments on device F05. The G peak position taken at room temperature under very low power (D2 filter) is shown for reference. The G peak was measured as a function of laser exposure time at full laser power. Most of the temperature increase (shift in G peak) occurs within the first few seconds. Typical exposure times are between 80-120 seconds, so steady-state can be assumed.

$$(18)\quad 0 = \frac{2\alpha_{CNT,\lambda} q_{laser}(y)}{\pi R} + \frac{2h_{CNT-Si}\left(T_{Si} - T(y)\right)}{\pi R} + k_{CNT,axial}\frac{d^2T(y)}{dy^2}$$

The laser is assumed to emit a beam with a Gaussian profile. The laser power density [W/m^2] is described by Eq. (19), where $q_{laser,y=0}$ is the laser power density at the center of the beam and w_0 is the spot size radius at which intensity drops to $1/e^2$ of the value at the beam center. Integrating over the entire surface, the total laser power (measured experimentally at the objective) is related to the laser power density at the beam center through Eq. (20).

(19) $q_{laser}(r) = q_{laser}(y) = q_{laser,y=0} e^{\left(-2y^2/w_0^2\right)}$

(20) $P_{laser}(\infty) = \int_0^\infty q_{laser}(r) 2\pi r dr = \frac{\pi w_0^2}{2} q_{laser,y=0}$

Eq. (18) can be solved analytically using the boundary conditions provided previously. The steady-state solution for the temperature at y = 0 (the primary area of the CNT being probed during Raman) is given as

(21) $T(y=0) = T_{Si} + q_0 \alpha w_0 \sqrt{\frac{1}{4Rk_{CNT-axial} h_{Si-CNT}}} e^{\frac{h_{Si-CNT} w_0^2}{4\pi Rk_{CNT-axial}}} \left[1 - erf\left(\sqrt{\frac{h_{Si-CNT}}{4\pi Rk_{CNT-axial}}} w_0\right)\right]$

Written in terms of the measurable laser power, $P_{laser}(\infty) = P_{laser}$, and parameter $\gamma = \sqrt{\frac{h_{Si-CNT} w_0^2}{4\pi Rk_{CNT-axial}}}$ the center temperature becomes

(22) $T(y=0) = T_{Si} + P_{laser} \frac{2\alpha}{h_{Si-CNT} w_0^2 \sqrt{\pi}} \gamma e^{\gamma^2} \left[1 - erf(\gamma)\right]$

Eq. (22) provides the relationship between the local tube temperature and the total power of the laser at the sample surface. Specifically, the slope of $T(y=0)$ vs. P_{laser} is

(23) $\frac{\beta}{X} = \left.\frac{\partial T}{\partial P_{laser}}\right|_{y=0} = \frac{2\alpha}{h_{Si-CNT} w_0^2 \sqrt{\pi}} \gamma e^{\gamma^2} \left[1 - erf(\gamma)\right]$

Using a variable neutral density filter, the laser power was varied for nanotubes in both filled and empty states, where the state of the tube was determined by the RBM peak position. The local tube temperature was calculated using Eq. (14), and example data is shown in Figure 31A. Consistently, we observe that β/X increases going from empty to filled state, as shown in Figure 31B. This result means that the filled tube has a higher local temperature increase due to increased laser power. Eq. (23) provides the relationship between β/X and $k_{CNT\text{-}axial}$, as plotted in Figure 31C. Assuming that h_{Si-}

$_{CNT}$ is constant between empty and filled tubes, filled tubes appear to consistently have lower axial thermal conductivity compared to empty tubes.

Physically the larger increase in local filled tube temperature with increasing laser power means that the nanotube is not dissipating heat as fast as the unfilled tube. If heat transfer to the silicon surface remains the same in both cases, the only other heat dissipation arises from thermal conduction along the tube, which is hindered when the nanotube is filled. One probable cause is that the long phonon mean free path in empty carbon nanotubes is reduced by the presence of water inside the nanotube, resulting in phonon scattering and a decrease in thermal conductivity.

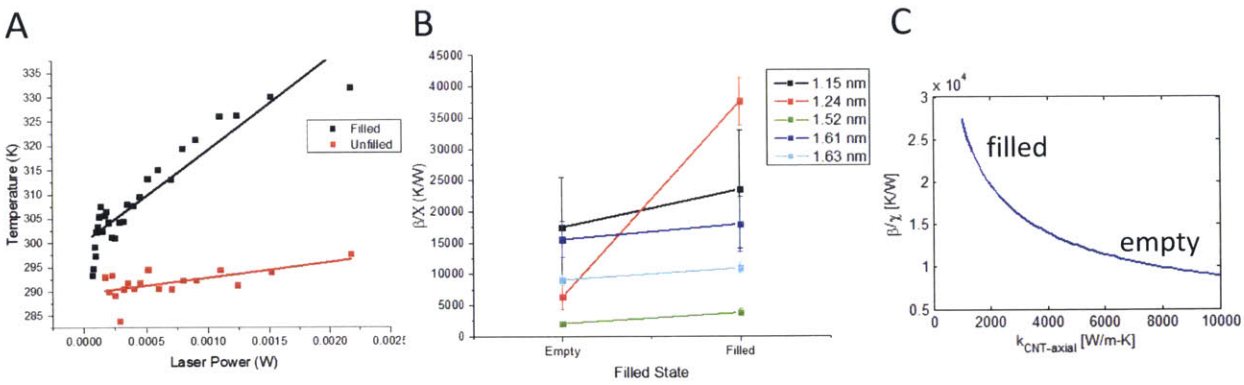

Figure 31. (A) Local temperature (obtained by G peak shift) versus the laser power for both water-filled and empty tube states (1.24 nm). The filled tube experiences a greater temperature rise as the laser power increases compared to the same tube in an empty state. (B) Comparison of β/X for tubes in an empty versus filled state. In all cases, the filled tube has a higher β/X, meaning that the local temperature increases more with increasing laser power compared to an empty tube. (C) Assuming that $h_{Si\text{-}CNT}$ is constant between filled and empty tubes, β/X is inversely related to $k_{CNT\text{-}axial}$. Accordingly, filled tubes are predicted to have lower axial thermal conductivity than empty tubes.

Laser-Induced Phase Transitions

The use of laser has been shown to affect the local filling state inside the tube due to local heating. Figure 32 demonstrates this finding for one nanotube (1.15 nm). When the reservoir and tubes are empty, varying the laser power does not change the RBM peak position. However, once the

reservoirs are filled with DI water and the tube fills, high laser power (lower filter optical density) causes enough local heating to locally vaporize the interior water. Thus, in the subsequent section on phase transition experiments, a combination of laser and stage heating can be employed to induce a phase transition.

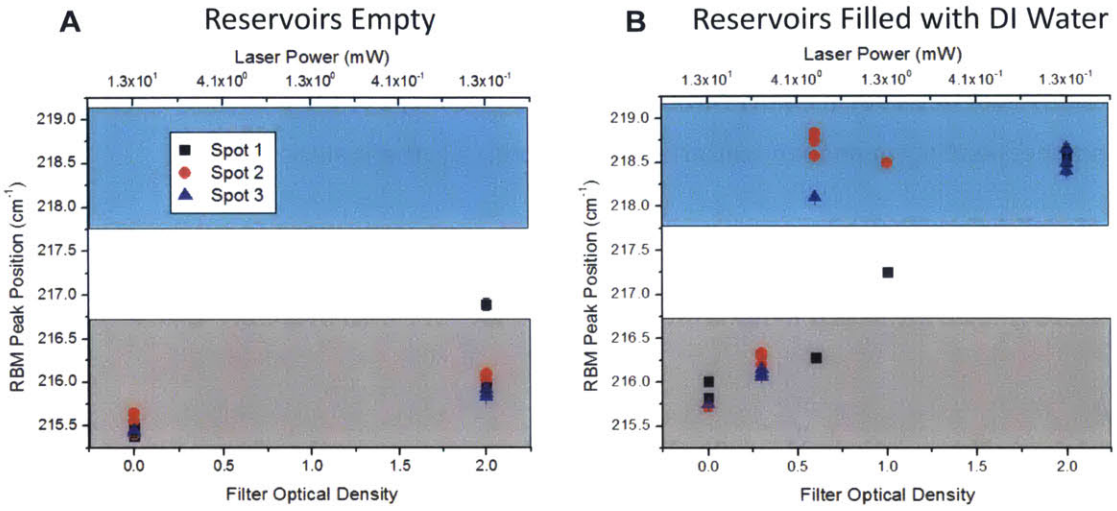

Figure 32. Inner RBM peak positions as a function of applied filter optical density (laser power) on three different spots along the nanotube. (A) When the reservoirs were empty, there is only a slight upshift in RBM peak position with decreasing laser power. (B) When the reservoirs are filled with DI water, there is a significant upshift in RBM peak frequency as the laser power decreases. The colored backgrounds serve to aid the eye in seeing the two different RBM peak regions, corresponding to empty/vapor (gray) and liquid water (blue).

5.3.5 Phase Transition Experiments

After thoroughly demonstrating that the Raman RBM upshift reflects the interior filling of the carbon nanotube with water and quantitatively determined the laser heating effect, the next step is to probe phase transitions of water inside the nanotube. Previous simulation work has indicated the possibility of such phenomena as well as significant shifts in freezing points with nanotube diameter.[68] To explore this effect, we used an environmental stage and/or laser power to vary the temperature while simultaneously monitoring the Raman spectrum. The first evidence that a phase transition is occurring is the discretized shift in RBM peak position with temperature and filling state. Despite varying temperatures and measurement conditions over a wide range, a histogram of the fitted RBM peak positions over many experiments (Figure 33) show the RBMs grouped into no more

than three distinct peak positions, which correspond with distinct water structures affecting the radial vibrations of the carbon atoms. Multiple Gaussian peaks were fitted to the histogram data, with the fitted peak centers provided in Table 6.

Longhurst and Quirke demonstrated the effect of internal filling of carbon nanotubes by modeling the carbon nanotube as an elastic shell and interior water as concentric rigid shells interacting through a Lennard-Jones potential.[80] This analytical model, confirmed by MD simulations, showed a 2-6 cm^{-1} upshift in the RBM frequency, albeit for a larger tube (1.72 nm). This shift is similar in magnitude the shift observed in our experiments.

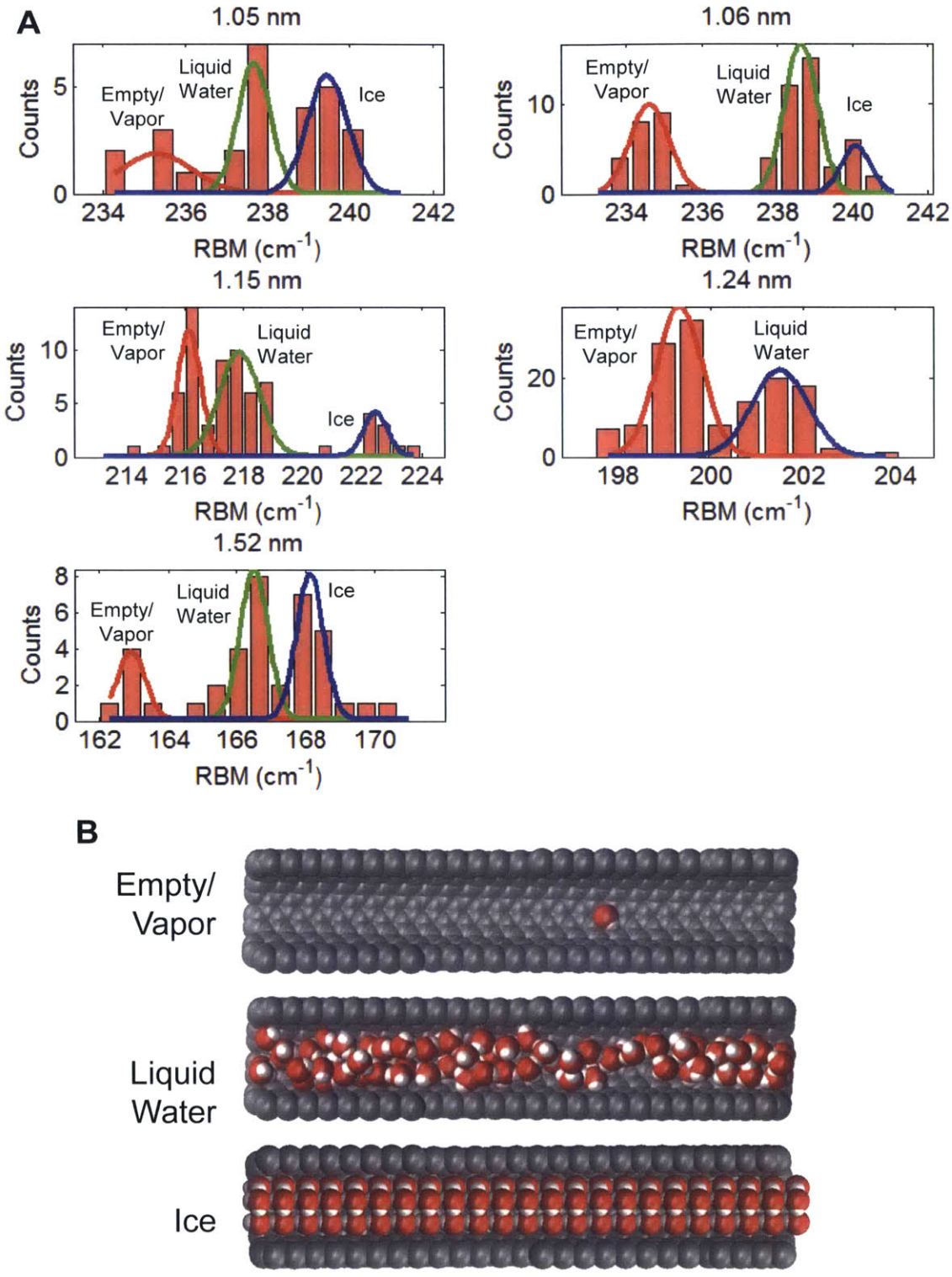

Figure 33. (A) RBM peak position histograms for each nanotube device. Gaussian peaks are fit to the histogram data, showing clear 2 or 3 peaks, corresponding to distinct filling states in the carbon nanotube. (B) Model illustrating the different filling states inside the nanotube.

Table 6. Fitted peak positions from fitting the RBM histograms.

Diameter [nm]	RBM 1 [cm^{-1}]	RBM 2 [cm^{-1}]	RBM 3 [cm^{-1}]
1.05	235 ± 3	237.7 ± 0.7	239.5 ± 0.7
1.06	234.2 ± 0.3	238.6 ± 0.3	240.0 ± 0.3
1.15	216.1 ± 0.2	217.9 ± 0.3	222.5 ± 0.5
1.24	199.3 ± 0.2	201.5 ± 0.4	--
1.52	162.9 ± 0.5	166.5 ± 0.4	168.1 ± 0.3

Further evidence that a phase transition is occurring is the reversibility of the process. Figure 34A shows that once the tube (1.15 nm) is filled with water (starting at experiment 3), cycling the stage temperature between 22 and -14.5 C causes reversible RBM shifts. Likewise, Figure 34B shows reproducible shifts in the RBM for another tube (1.06 nm) when cycling between laser filters, which vary the local tube temperature.

Additionally, Figure 34A shows that the RBM peak position does not vary significantly with temperature, and the discrete shifts cannot be explained by an effect that varies continuously with temperature (unlike the G peak, which was shown to vary significantly and continuously with temperature). In this example, decreasing the temperature by approximately 20 degrees once the RBM has upshifted a second time results in roughly the same RBM peak position around 222 cm^{-1}.

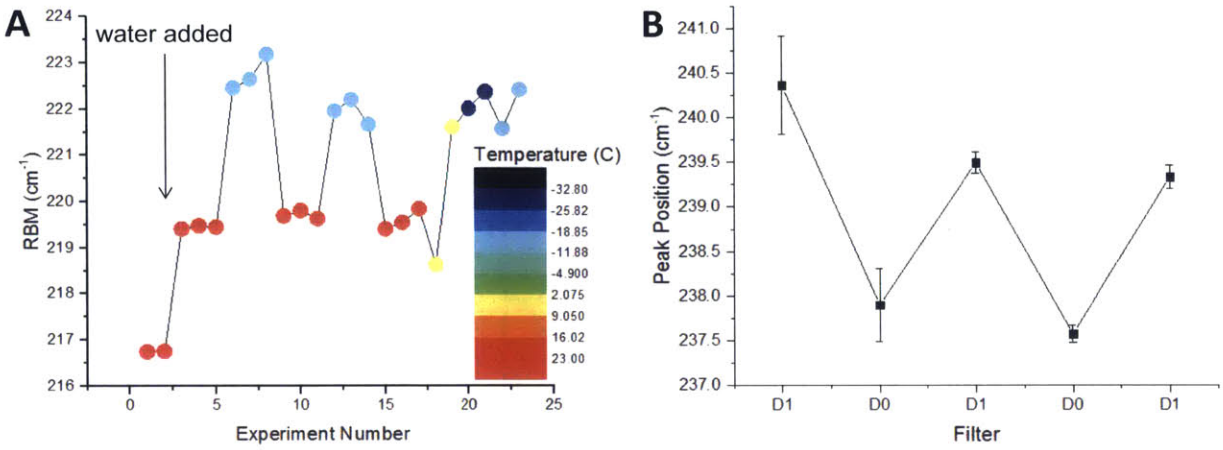

Figure 34. Reversibility of phase transitions of water inside a carbon nanotube. (A) Varying stage temperature for a nanotube (1.15 nm) causes discrete, reversible shifts in RBM peak positions. (B) Changing the laser intensity for another nanotube (1.06 nm), which also varies the local temperature, causes a reversible shift in the RBM.

Figure 36 provides the results for the phase transition experiments carried out on all the nanotubes, along with fitted curves. The transition data are fit to two Heaviside approximation functions, as described in Figure 35. For the one device (1.24 nm) which did not appear to show a solid-liquid phase transition, only the vapor-liquid transition curve was used. The equations are described as follows:

(24) $$R_{sl} = \frac{(R_s + R_l)}{2} + \frac{(R_s - R_l)}{2} erf\left(\frac{T_{sl} - T}{s_1}\right)$$

(25) $$R_{lv} = \frac{(R_l + R_v)}{2} + \frac{(R_l - R_v)}{2} erf\left(\frac{T_{lv} - T}{s_2}\right)$$

(26) $$R_{slv} = R_{sl} + R_{lv} - R_l$$

where R_s, R_l and R_v are the RBM peak positions of the solid, liquid and vapor phases, respectively. T_{sl} and T_{lv} are the solid-liquid and vapor-liquid transition temperatures. The parameters s_1 and s_2 are fitting parameters that adjust the width of their respective transitions. The final equation gives R_{slv}, the expected RBM value across solid-liquid-vapor phases.

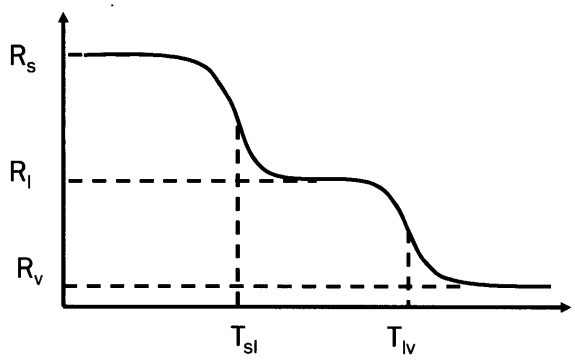

Figure 35. Sample curve used to fit the transition data (RBM peak position versus temperature).

The shaded regions indicate the range of RBM corresponding to the fitted peaks in Figure 33. While scatter is significant, these results clearly show that the upshift from the filled, liquid phase (green) occurs at lower temperatures. The RBM peak position was confirmed to be independent of the presence of external water or frost on the surface, so the second upshift likely comes from a change

in the internal water state. The fact that this second shift is a hardening of the radial vibrational indicates that the carbon atoms are in contact with a stiffer material of a higher modulus. Coupled with the observation that this upshift occurs at lower temperatures, we conclude that we are observing solidification of water inside the nanotube.

The approximate ranges of freezing and vaporization temperatures are provided in Table 7. The best-fit values are those corresponding with the fitted values when fitted to Eq. (26). The 95% confidence intervals for the values were determined using bootstrap resampling methods with 10000 resamples. However, due to lack of data at some phases and around the transition point, bootstrapping sometimes gave nonsensical confidence intervals (extremely large negative or positive values). In these cases, the confidence interval was manually recorded to be the closest data point that was clearly in the RBM range defined for the phase being transitioned to (denoted by an asterisk, *).

While it would be ideal to obtain more points at all the phases, the devices became inoperable over time and were unable to fill, perhaps due to blocking by contaminants. More consistent data collection, along with an estimate of what temperature ranges to probe (as provided by this study), will allow more data points around the transition region to provide a better estimate of transition temperatures. Regardless, the data show very clearly the distinct RBM transitions occur with respect to temperature.

The significant range of the phase transition temperatures can be explained by the effect of various environmental variables. Most of the effect on the water phase transition arises from confinement by the nanotube and the intermolecular interactions between interior water and carbon atoms which modify the chemical potential of the interior water. However, there are several confounding variables in this study that may also affect the chemical potential of interior water: the substrate, physisorbed material, and nanotube defects and inhomogeneity.

The nanotubes in this study were in physical contact with the substrate, a layer of silicon oxide. The state of the oxide layer may vary slightly from device to device and even on the same device, and the intermolecular interaction between the substrate and interior water will affect the water chemical potential. Using suspended SWNT, while more difficult to fabricate, would eliminate this variable.

While physisorbed water did not appear to affect the value of the RBM frequency, the interaction between external species and interior water could still modify the potential of the water and shift the transition point. We attempted to use a cleaner system by performing these experiments under vacuum in the enclosed environmental stage, but the glass barrier resulted in too much Raman signal loss for this approach to be feasible. Instead, we flowed nitrogen over the sample while exposed to the environment to reduce frost formation, humidity effects, and prevent other particulates from adsorbing to the surface.

Similarly, chemical defects along the nanotube can dramatically affect the water state. The nanotubes used in this study are quite pristine, as no D peak is observed in the Raman spectra (the D peak corresponds to sp3-hybridized carbons which indicate defects in the nanotube). However, the absence of a discernible D peak does not mean there are zero defects, and a couple defects, sidewall functionalization or kinks in the nanotube could have a significant impact on the interior water state. Future work may induce defects in the sidewall to more quantitatively determine the effect on filling and phase transitions.

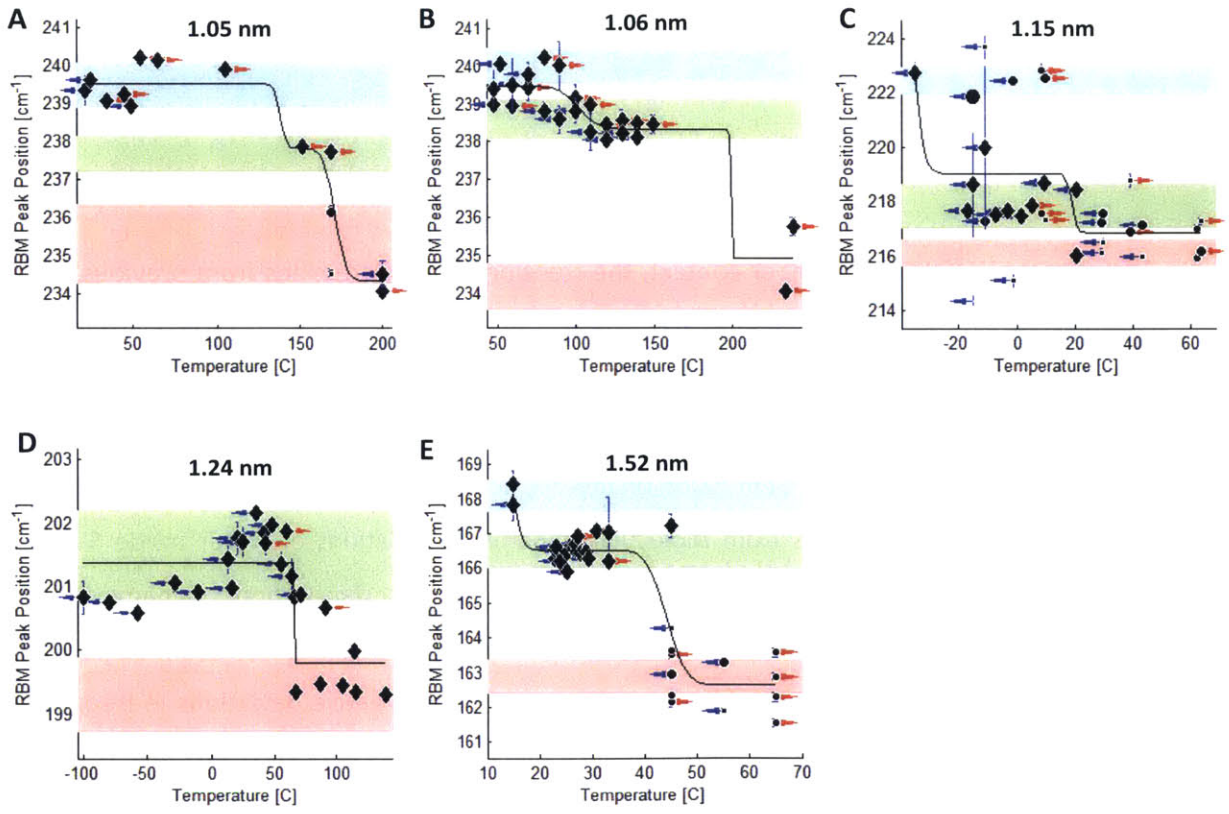

Figure 36. Phase transition experiments showing RBM peak position as a function of nanotube temperature, which was varied with laser and/or stage temperature. Blue, left-pointing arrows indicate that this point was approached by cooling from a higher temperature, red, right-pointing arrows indicate that this point was approached by heating from a lower temperature, and no arrow indicates a neutral, starting state. The shaded background illustrates the RBM regions that correspond to the given state of water (blue = ice, green = liquid water, red = vapor), where the width of each region is the FWHM of the peaks fitted to the RBM histogram in Figure 33. Diamond symbols indicate a single peak was fitted to the spectrum, while circle symbols indicate that multiple peaks were fit to the data, and the relative size of the symbol indicates the proportional area of the peak.

Table 7. Summary of phase transition temperatures observed in nanotube devices. Low and high values are from 95% confidence intervals using bootstrapping methods. In cases where the bootstrap value was invalid due to lack of data points around the transition, the upper or lower bound was manually recorded (marked with *) by finding the closest data point that was clearly in the RBM range defined for the phase being transitioned to.

	Solid-Liquid Transition [C]			Liquid-Vapor Transition [C]		
Diameter [nm]	Low	Fit Value	High	Low	Fit Value	High
1.05	105*	**138**	151*	158	**171**	171
1.06	87	**102**	117*	144	**199**	234*
1.15	-50*	**-50**	10*	18*	**19**	40*
1.24		**no transition**		44	**66**	80
1.52	3	**15**	30	39	**44**	51

To put these results in a broader context, the freezing point depressions from previous, molecular dynamics simulations, and theory are plotted together in Figure 37. The blue points are experimental data points from bulk quantities of MWNT that used DSC to measure the freezing point depressions.[81] This data fit well to the Gibbs-Thomson equation, which predicts a linear dependence of freezing point depression on inverse pore diameter. The red points on the plot show the predicted freezing points from molecular dynamics simulations of water inside SWNT.[68] The simulation data show very significant deviations from bulk, interfacial thermodynamics (blue line). The green and cyan points indicate experimental freezing points on bulk quantities of SWNT as measured by NMR[75] and XRD[74], which also show significant negative deviations in freezing points. The current set of experiments is represented by black points showing data taken across a range of nanotube diameters. The dashed black line indicates the one nanotube (1.24 nm) where water filling was observed, but no freezing transition was observed. Finally, the dashed magenta line represents

the lower temperature bound of the experimental apparatus (-80 °C). While the stage is cooled by liquid nitrogen (T_f = -210 °C), there is significant heat transfer from the stage and convection.

Interestingly, there are two devices of similar diameter (1.05 nm and 1.06 nm) that both have very high freezing points observed: 105 – 151 C and 87 – 117 C. The 1.24 nm nanotube did not have an observed phase transition even after decreasing the temperature below -80 C. Meanwhile, the 1.15 nm nanotube has a transition roughly around that of bulk water while the largest tube (1.52 nm) has an elevated phase transition around room temperature (3 - 30 C). Thus, we demonstrate a remarkable range in the freezing transition temperature of nanoconfined water that is highly variable and non-monotonic with diameter. The ability to make large quantities of pure, single-chirality nanotubes could create opportunities in making tunable phase transition materials over a wide temperature range.

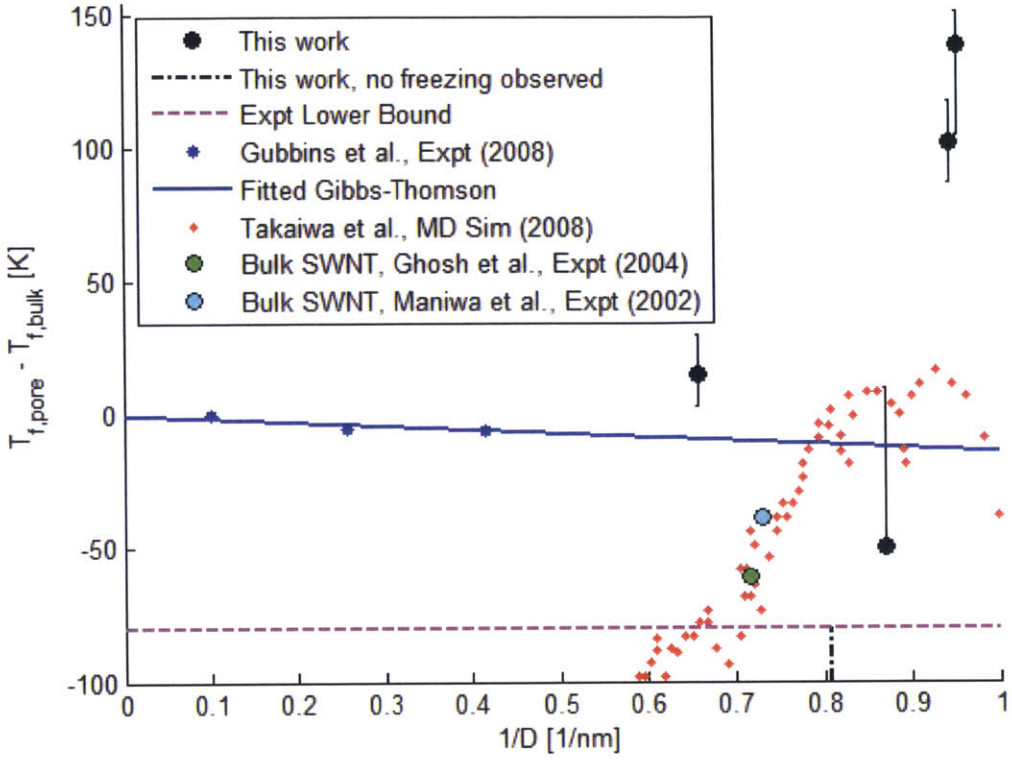

Figure 37. Freezing point depressions of water inside carbon nanotubes taken from experiment, theory, and modeling. Blue points indicate experimental freezing point depressions for water inside larger multi-walled carbon nanotubes.[81] The fitted blue line is the expected trend for freezing point depression assuming the Gibbs-Thomson equation holds. Red points indicate the results from molecular dynamics simulations of water freezing inside SWNT.[68] The green and cyan points are experimental freezing point depressions measured on bulk samples of SWNT using NMR[75] and XRD[74]. Black points indicate experimental freezing point depressions from this work, and the dashed black line indicates a tube for which no freezing transition was observed despite water filling. Finally, the dashed magenta line indicates the approximate lower temperature bound for the experiment, roughly -80 °C.

5.4 Conclusion

While previous experiments have shown changes in Raman spectra for bulk collections of filled and unfilled nanotubes of different chiralities, this study spectroscopically probes the effect of filling and phase transitions on the radial breathing modes of single, isolated nanotubes. Detailed analysis of the laser heating effect on the local temperature and filling state is presented, along with the ability to infer nanotube properties in different filling states. Solid-liquid phase transitions are observed in four of the tubes studied, showing significant positive deviations in the freezing point compared to bulk. These experiments introduce a simple and useful analytical technique for obtaining phase

diagrams and understanding filling conditions in individual carbon nanotube nanopores which will play a large role in the field of nanopore thermodynamics and nanofluidics.

6. Analysis of Freezing Point Changes in Fluids Confined to Nanopores

6.1 Introduction

Phase transitions of nanoconfined fluids are important for understanding adsorption and transport through networks of nanopores, including carbon[16], silica[82] and zeolites[83]. The prediction and modeling of freezing points of nanoconfined fluids is important in several applications, including understanding transport through nanopore-based membranes, the extraction potential of oil and gas inside of geological nanopores[22], and the construction of self-releasing nanocontainers for small-molecule delivery[29]. Recently there have been several experimental studies on the freezing of fluids in nanopores[84-85] which show quite different behavior from that of bulk fluid.

While the freezing point depression can be shown to vary linearly with inverse pore radius, as predicted by the Gibbs-Thomson equation, researchers frequently employ this equation assuming ΔH_m is invariant with radius. However, thermo-calorimetry data[86] indicate that ΔH_m monotonically increases with radius with some generality. The purpose of this current paper is to address the problem that widely employed models predicting ΔH_m and surface free energy (γ_{SL}) separately as a function of radius, when evaluated in the Gibbs-Thomson equation, cannot predict experimental freezing points of confined fluids. As an alternative to using the Tolman length correction[87] for calculating solid-liquid surface energies, with questionable validity, we instead apply energetic analysis from metal nucleation theory[88]. Nanoconfined fluids are well described by a so-called Turnbull coefficient, $\gamma_{SL}/\Delta H_m$, that is predicted theoretically and experimentally shown to remain invariant with pore radius but variable for different molecules.

The Gibbs-Thomson equation is often used to explain the variation in freezing points compared to the bulk for fluids confined to micro- and nano-sized dimensions.[89] The most common form of the Gibbs-Thomson equation employed in the literature for freezing in cylindrical pores is[90]:

$$(27)\ \Delta T_f = T_{f,bulk} - T_{f,pore} = \frac{2T_{f,bulk}V_m\gamma_{SL}}{R_{pore}\Delta H_m}$$

where $T_{f,pore}$ is the modified freezing point of the fluid inside the pore, $T_{f,bulk}$ is the bulk freezing temperature, V_m is the molar volume of the liquid or solid phase, γ_{SL} is the interfacial energy between the liquid and solid phases, r is the radius of the pore, and ΔH_m is the enthalpy of melting (= $H_l - H_s > 0$). It should be noted that the right-hand side of the equation is generally positive, meaning that the fluid experiences a freezing point depression when inside a pore. This common form of the equation assumes that $V_{s,m} = V_{l,m} = V_m$ and that the solid is surrounded by its own liquid melt inside the pore (e.g. there is a solid plug in equilibrium with a liquid annulus). Thus, the center of curvature of the solid-liquid interface lies within the solid phase—otherwise, there would be a negative sign in front of the right-hand side of the equation.

In theory, the Gibbs-Thomson equation could be used to predict freezing point changes for confined fluids, but this is rarely employed due to the difficulty in determining reliable values of γ_{SL}. There is some controversy in the literature on the best way of obtaining solid-liquid and solid-vapor surface energies, which are more difficult to obtain experimentally compared to liquid-vapor surface tensions.[91]

We address the applicability of the Gibbs-Thomson equation in this work for nanoconfined fluids both organic and aqueous in pores between 4 and 25 nm in diameter. We note that a continuum assumption for the solid-liquid interface can break down for pores smaller than 4 nm generally[68], and so we limit the applicability of our analysis to pores larger than this limit.

Table 8. List of symbols used in this study.

Symbol	Name/Description	SI Units
$T_{f,bulk}$	Bulk freezing temperature	K
$T_{f,pore}$	Freezing temperature inside the pore	K
ΔT_f	Difference between bulk and pore freezing temperatures	K
ΔH_m	Enthalpy of melting	J/mol
r	Pore radius	m
$V_{m,sol}$	Solid molar volume	m^3/mol
$V_{m,liq}$	Liquid molar volume	m^3/mol
γ_{SL}	Solid-liquid surface free energy	J/m^2
$\gamma_{SL,\infty}$	Solid-liquid surface free energy of a planar interface	J/m^2
δ	Tolman length	m
R	Universal gas constant	J/K-mol
N_A	Avogadro's constant	#/mol
d^2	Ratio of mean-square amplitudes in the liquid phase	--
$\Delta S_{m,bulk}$	Melting entropy of the bulk	J/K-mol

6.2 Deficiency of Tolman Length Correction to Predict Freezing Point Depressions

While it has been demonstrated that the Gibbs-Thomson equation is applicable for solid-liquid phase equilibria[91], the equation assumes γ_{SL} and ΔH_m values are constant. Experimentally, the freezing points of fluids are commonly measured using dynamic scanning calorimetry (DSC)[86, 92] which has the added advantage of being able to simultaneously measure the enthalpy change of the transition. Only a few studies[86, 92] have actually measured both freezing points and enthalpies of fusion for substances as a function of the pore diameter, and these studies found very significant changes in ΔH_m as a function of pore radius. The data is reproduced in Figure 38. These results would seem to suggest that a simple plot of ΔT_f vs. 1/r would be very non-linear, assuming γ_{SL} is

constant, as suggested by the Gibbs-Thomson equation; in fact experimentally, plotting ΔT_f vs. 1/r shows linearity down to 3 or 4 nm pore diameter.

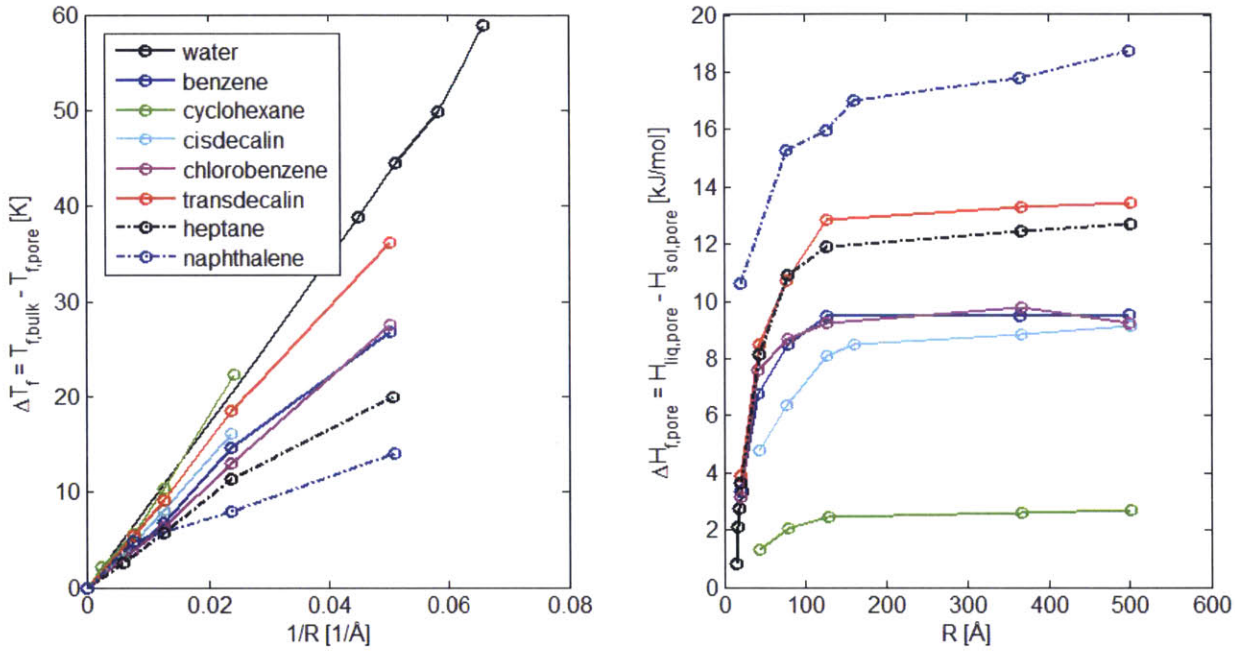

Figure 38. Freezing point depression and enthalpies of fusion plotted versus inverse pore radius and pore radius, respectively. Data reproduced from Jackson and McKenna[86] and Findenegg[92].

In order to explain this trend, assuming V_m does not change significantly with pore diameter, then the solid-liquid surface free energy (γ_{SL}) must be a function of radius as well. Several researchers have employed the Tolman length correction to predict the γ_{SL} using Eq. (28).[93-94] However, the actual form of the equation derived by Tolman is Eq. (29). Eq. (28) is a first-order approximation of Eq. (29) by expanding around $2\delta/r = 0$ (a planar surface). The Tolman length, δ, is a distance equal to the difference between the equimolar surface and the surface of tension. The value of this parameter is largely unknown, and there is debate as to the sign of the Tolman length, as well as its magnitude, although most agree that it is on the order or smaller than the molecular diameter.[87]

$$(28)\ \gamma_{SL}(r) = \gamma_{SL,\infty}\left(1 - \frac{2\delta}{r}\right)$$

$$(29)\ \gamma_{SL}(r) = \gamma_{SL,\infty}\frac{1}{(1 + 2\delta / r)}$$

Shin and co-workers attempted to explain theoretically why the enthalpy of fusion changes at small pore radii for the same dataset used here.[94] Their model assumes a spherical particle in equilibrium with its own melt and uses the Tolman equation to describe the surface energy as a function of radii. The enthalpy of melting they obtain is a function of radius, surface energy, the change in solid molar volume with respect to temperature, and the change in surface energy with respect to temperature. The surface energy as a function of pore radius is modeled using Eq. (28), the simplified Tolman length correction. They successfully fit the datasets of fusion enthalpies versus pore radii using only the Tolman length as a fitting parameter, and making use of data and correlations in the literature to obtain the other parameters related to molar volume and surface energies.

Extending this analysis, we used the fitted Tolman lengths to compute the predicted surface energy at each pore radius. Substituting the experimental ΔH_m and γ_{SL} into the Gibbs-Thomson equation, we show that the resulting ΔT_f calculated using this model is much higher than observed experimentally by over several hundred Kelvin, as shown in Figure 39. Thus, while their model can fit the enthalpy change as a function of Tolman length, the freezing points cannot be accurately predicted using this method.

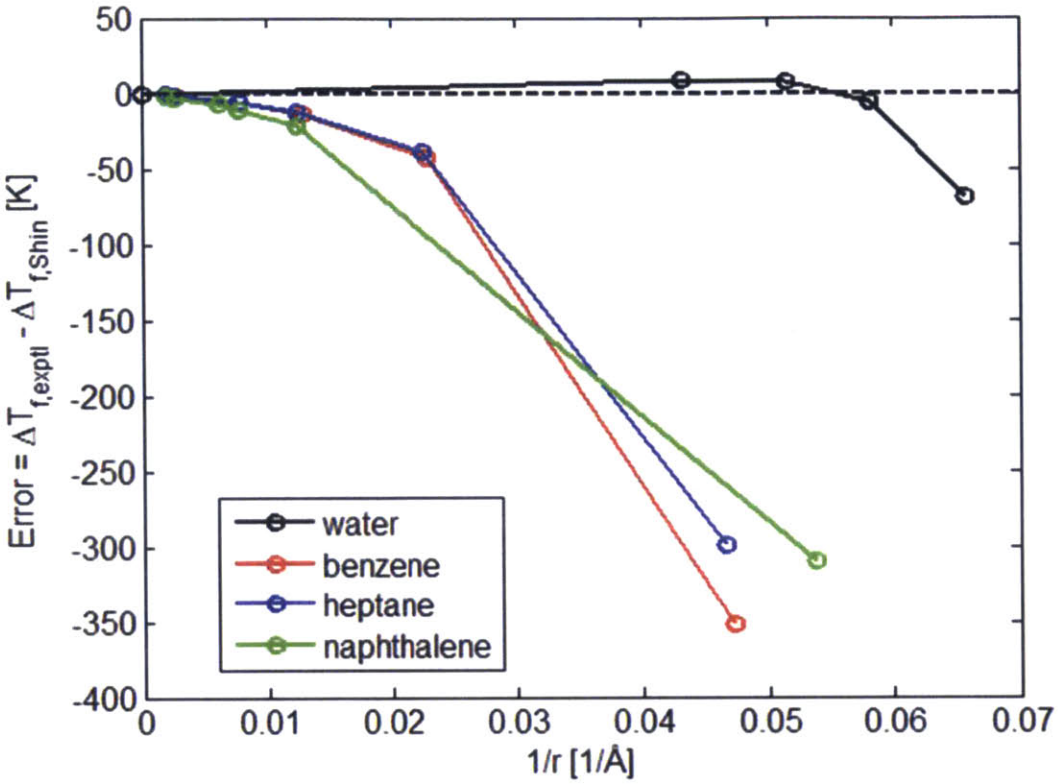

Figure 39. Plot showing the discrepancy between experimental freezing point depressions and those predicted using the Gibbs-Thomson equation and fitted Tolman lengths from Shin et al.[94]

We then determined whether the Tolman length correction could correctly compensate for the change in the experimental fusion enthalpies by fitting the Tolman length (δ) and solid-liquid surface energies for planar interfaces ($\gamma_{SL,\infty}$) in Eq. (28) and (29) to best fit the observed freezing point depressions using the experimental ΔH_{pore}. Figure 40 shows the discrepancy between observed $\Delta T_{f,calc}$ and $\Delta T_{f,expt}$. Interestingly, the more precise Tolman length correction gives a worse fit to the data and gives unreasonably large values for the Tolman length (see Table 9)—the first-order approximation actually works better in all the cases despite the prediction not being valid at such small sizes. This result calls into question the use of the Tolman length correction for solid-liquid systems. Tolman originally[95] derived the equation for a vapor-liquid system, and there have since been no rigorous derivations for solid-liquid systems. Furthermore, since the Tolman lengths and solid-liquid surface energies for materials are controversial, even using the first-order approximation of the Tolman correction to predict freezing points is difficult.

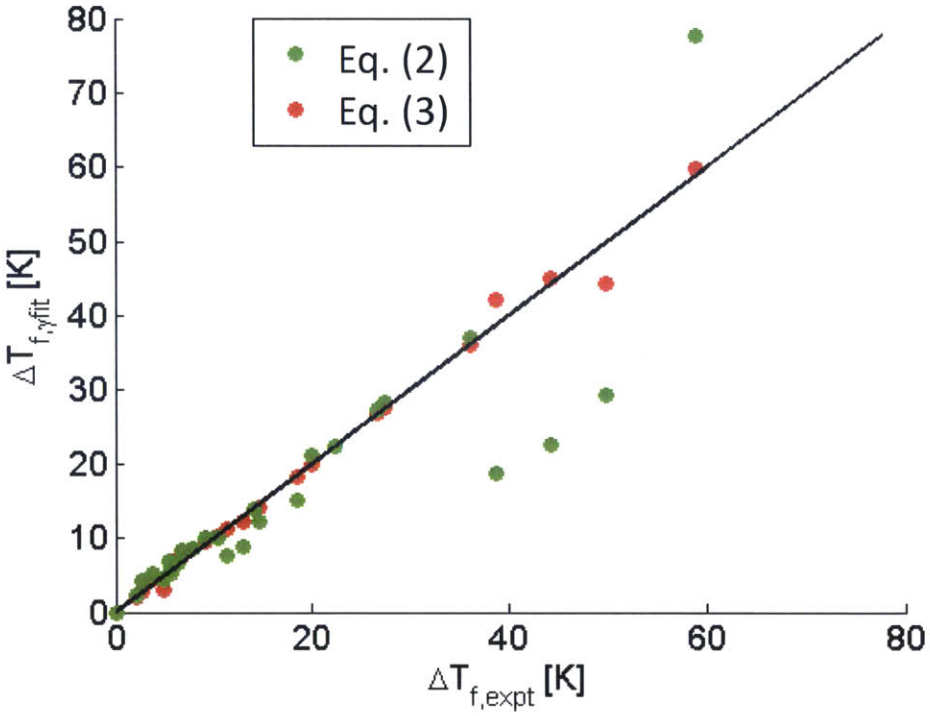

Figure 40. A parity plot showing the freezing point depressions for all fluids calculated by fitting the Gibbs-Thomson equation to the experimental ΔT_f, using the experimental ΔH_{pore} and the Tolman length correction (either Eq. (28) or (29)) describing γ_{SL} as a function of radius. The parameters $\gamma_{SL,\infty}$ and δ were fitted for each fluid's temperature dataset. Eq. (28), despite being the more accurate form of the Tolman length correction for small droplet sizes, does not predict the freezing point changes well at higher freezing point depressions (smaller pore radii).

Table 9.Fitted values of $\gamma_{SL,\infty}$ and δ by fitting $\Delta T_{f,expt}$ to the Gibbs-Thomson equation using $\Delta H_{m,expt}$ and the Tolman length correction.

	Tolman Correction (Eq. 2)		Tolman Correction (Eq. 3)	
Fitted Parameters	$\gamma_{SL,\infty}$ (mJ/m^2)	δ (Å)	$\gamma_{SL,\infty}$ (mJ/m^2)	δ (Å)
Water	84.2	6.9	41548	32876
Chlorobenzene	13.3	7.6	36.2	103
Trans-decalin	13.2	7.2	34.1	79.4
Benzene	12.3	7.1	38.8	95.8
Heptane	11.6	8.0	56.6	266
Naphthalene	8.9	5.8	18.9	41.6
Cis-decalin	7.3	7.8	8.3	17.1
Cyclohexane	3.5	9.0	4.2	22.5

Thus, using the Tolman length correction to predict the trend of γ_{SL} as a function of r is not ideal, especially since this also requires a model for $\Delta H_{m,pore}(r)$ (in the previous analysis, we used the available, experimental $\Delta H_{m,pore}$, but generally this is not known as a function of pore size for a given substance). Instead, it can be reasoned that if ΔT_f varies linearly with 1/r, then the ratio of solid-liquid free energy and enthalpy of fusion, $\gamma_{SL}/\Delta H_m$, should be a constant. Indeed, plotting $\gamma_{SL}/\Delta H_m$ (found by using experimental ΔT_f in the Gibbs-Thomson equation) versus the inverse pore radius, we show this quantity to actually be invariant with radius as demonstrated in Figure 41.

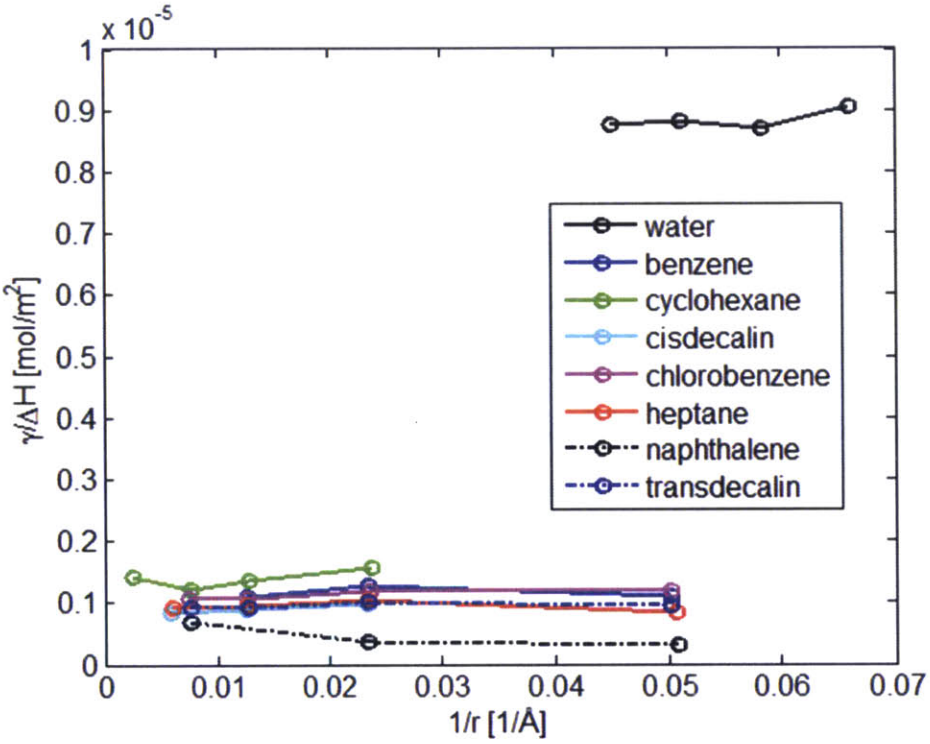

Figure 41. A plot of calculated $\gamma_{SL}/\Delta H_m$ as a function of inverse pore radius for compounds considered in Figure 38, showing the invariant nature of this quantity as a function of pore radius.

6.3 Analysis of First-Order Model for the Turnbull Coefficient

Turnbull was the first to realize the value of this ratio, which we term the Turnbull coefficient, further non-dimensionalizing the quantity to become $\gamma_{SL}V_{m,sol}^{2/3}N_A^{1/3}/\Delta H_f$, which physically represents the free energy of forming a monolayer of solid-liquid interface using one mole of material, divided by the enthalpy of fusion.[96] The experimental γ_{SL} were found by measuring rates of homogeneous nucleation, which is modeled as being a function of γ_{SL}. He demonstrated this ratio to be useful in describing metal nucleation, where many metals had Turnbull coefficients ≈ 0.45; this empirical correlation could be used to predict nucleation rates and melting points for metals.

For a first-order approximation of the Turnbull coefficient, we first consider only the enthalpic contributions to the surface free energy; no entropy changes are considered. Consider placing two blocks of bulk solid and bulk liquid with molar volumes $V_{m,sol}$ and $V_{m,liq}$, respectively. When the interface forms, we assume that the interfacial layers retain their respective bulk densities and there is a single interfacial layer in each phase. There are three representative outcomes: 1) the interfacial layer of the solid remains the same as $H_{sol,bulk}$, but the liquid rearranges itself and has an enthalpy halfway between solid and liquid, 2) the solid interfacial layer appears more liquid-like and has an enthalpy halfway between solid and liquid, while the liquid interfacial layer has the same enthalpy as $H_{liq,bulk}$, or 3) the interfacial layers of both phases have enthalpies equal to half of ΔH_f. These scenarios are represented in Figure 42, along with the expected Turnbull coefficient for each case.

In all cases, the energy required to form a monolayer of interface from the reference state (bulk liquid and bulk solid phases) in J/mol-solid is

$$(30)\ \gamma_{SL}V_{m,sol}^{2/3}N_A^{1/3} = \text{Energy to form a solid-liquid interface from the reference state [J/mol-solid]}$$

For the case where only the liquid interfacial layer is affected energetically (Figure 42B), the energy of the solid phase is constant up to the dividing surface, and so the enthalpy change is just the energy to convert the liquid monolayer to an interfacial monolayer is

$$(31)\ -\frac{\Delta H_m}{2}\frac{V_{m,sol}^{2/3}}{V_{m,liq}^{2/3}} = \text{Energy to convert liquid layer to interfacial layer [J/mol-solid]}$$

where V_m is the molar volume, either of the solid or liquid phases. For the case shown in Figure 42C where the solid atoms are primarily affected upon the formation of the interface, the enthalpy change of the system can be written simply as

(32) $\frac{\Delta H_m}{2}$ = Energy to convert solid layer to interfacial layer [J/mol-solid]

And finally, in the third case, where the interfacial layers of the solid and liquid phases both change energetically, as in Figure 42D, we can write the energy change of the system to be

(33) $\frac{\Delta H_m}{2} - \frac{\Delta H_m}{2}\frac{V_{m,sol}^{2/3}}{V_{m,liq}^{2/3}}$ = Energy to convert solid and liquid to interfacial layers [J/mol-solid]

Equating Eq. (30) with Eqs. (31), (32) and (33), we obtain the following predicted Turnbull coefficients:

(34) $\gamma_{SL} V_{m,sol}^{2/3} N_A^{1/3} = -\frac{\Delta H_m}{2}\frac{V_{m,sol}^{2/3}}{V_{m,liq}^{2/3}} \rightarrow \frac{\gamma_{SL} V_{m,liq}^{2/3} N_A^{1/3}}{\Delta H_m} = -\frac{1}{2}$ (only liquid interfacial layer changes energy)

(35) $\gamma_{SL} V_{m,sol}^{2/3} N_A^{1/3} = \frac{\Delta H_m}{2} \rightarrow \frac{\gamma_{SL} V_{m,sol}^{2/3} N_A^{1/3}}{\Delta H_m} = \frac{1}{2}$ (only solid interfacial layer changes energy)

(36) $\gamma_{SL} V_{m,sol}^{2/3} N_A^{1/3} = \frac{\Delta H_m}{2}\left(1 - \frac{V_{m,sol}^{2/3}}{V_{m,liq}^{2/3}}\right) \rightarrow \frac{\gamma_{SL} V_{m,sol}^{2/3} N_A^{1/3}}{\Delta H_m} = \frac{1}{2}\left(1 - \frac{V_{m,sol}^{2/3}}{V_{m,liq}^{2/3}}\right) \approx 0$

(both solid and liquid interfacial layers change energy)

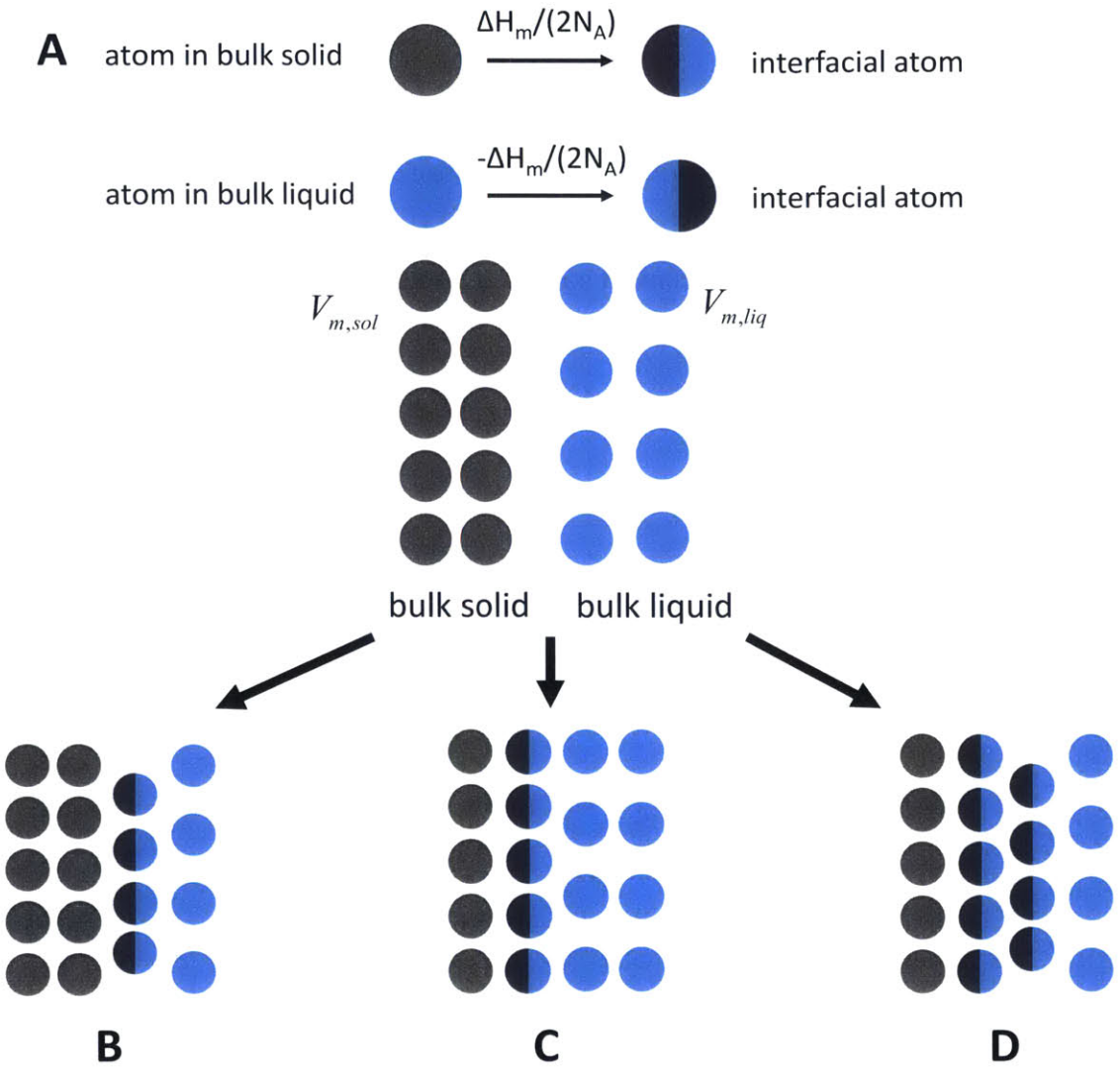

Figure 42. Schematic of formation of solid-liquid interface. (A) Representation of an atom in bulk solid or bulk liquid becoming an interfacial atom, which is represented as being equally in each phase. Three representative scenarios upon formation of an interface are when (B) only the interfacial layer of the liquid experiences a change in enthalpy, (C) only the interfacial layer of the solid phase experiences a change in enthalpy, and (D) both interfacial layers experience a change in enthalpy.

Okui suggested a zero-order approximation of the Turnbull coefficient to be ½ since a molecule on the surface is essentially half liquid.[97] The more complete analysis above shows that this reasoning is valid only if one assumes that entropy plays no role and only the solid interfacial layer has an enthalpy midway between solid and liquid. And physically, the surface energy cannot be negative

(scenario 1), or else the bulk phases wouldn't exist—it would be more favorable to form as much surface as possible.

Broughton and Gilmer's molecular dynamics simulation for crystal-melt interfaces was used to approximate the Turnbull coefficient for a Lennard-Jones system to determine which scenario is more likely.[98] The density and potential energy profiles per particle were calculated for a face-centered-cubic crystal, with three different crystal faces ((111), (110) and (100)) in contact with bulk liquid. These data are summarized in Figure 44. These profiles were used to find the predicted Turnbull coefficient for each type of interface, using the assumption that the bulk potential energy for each phase can be used to directly estimate the change in enthalpy of the system.

The total energy change for the system was calculated per solid molecule at the interface to find the surface interfacial energy. The Turnbull coefficient was determined as the ratio between the interfacial energy and the enthalpy change of the system. The value of this ratio for the (111), (110) and (100) crystal faces were 0.56, 1.2, and 0.42 respectively, indicating that the system is anisotropic. The calculated ratios for the (111) and (100) interfaces fall close to the expected coefficient value 0.50, but the value for the (110) interface is twice as high. The (110) crystal face has the least number of solid particles in direct contact with the interface, which could indicate that inefficient packing or irregularity in the crystal lattice may have a pronounced effect on the value of the Turnbull coefficient for a given system.

We observe that the potential energy of the solid phase is more affected by the formation of the interface, and the potential energy change extends beyond the first interface layer, which more than offsets the decrease in potential energy of the interfacial liquid layers. The zero-order model we presented assumes only the first interface layers of the solid or liquid phase can have a change in enthalpy. In reality, since the potential energy changes propagate through the liquid and solid phases, one can expect the Turnbull coefficient to be >1/2.

We can thus conclude that a first-order approximation to the Turnbull coefficient is ½, which provides a close approximation to the values obtained from freezing point data for fluids confined to nanopores, which range between 0.097 and 0.51 (Figure 43).

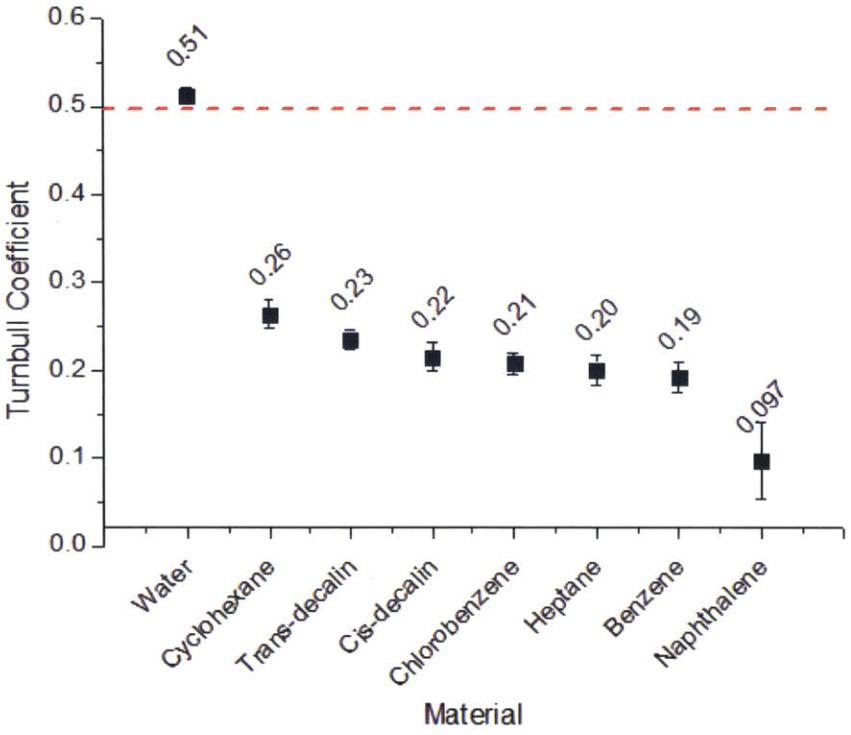

Figure 43.Plot of Turnbull coefficients ($\gamma_{SL}V_m^{2/3}N_A^{1/3}/\Delta H_f$) calculated by applying the Gibbs-Thomson equation to the freezing point depression data to solve for $\gamma_{SL}/\Delta H_f$. This value was obtained for all pore radii available and averaged. The red dashed line indicates the first-order model predicted if only enthalpy is considered when estimating the surface free energy.

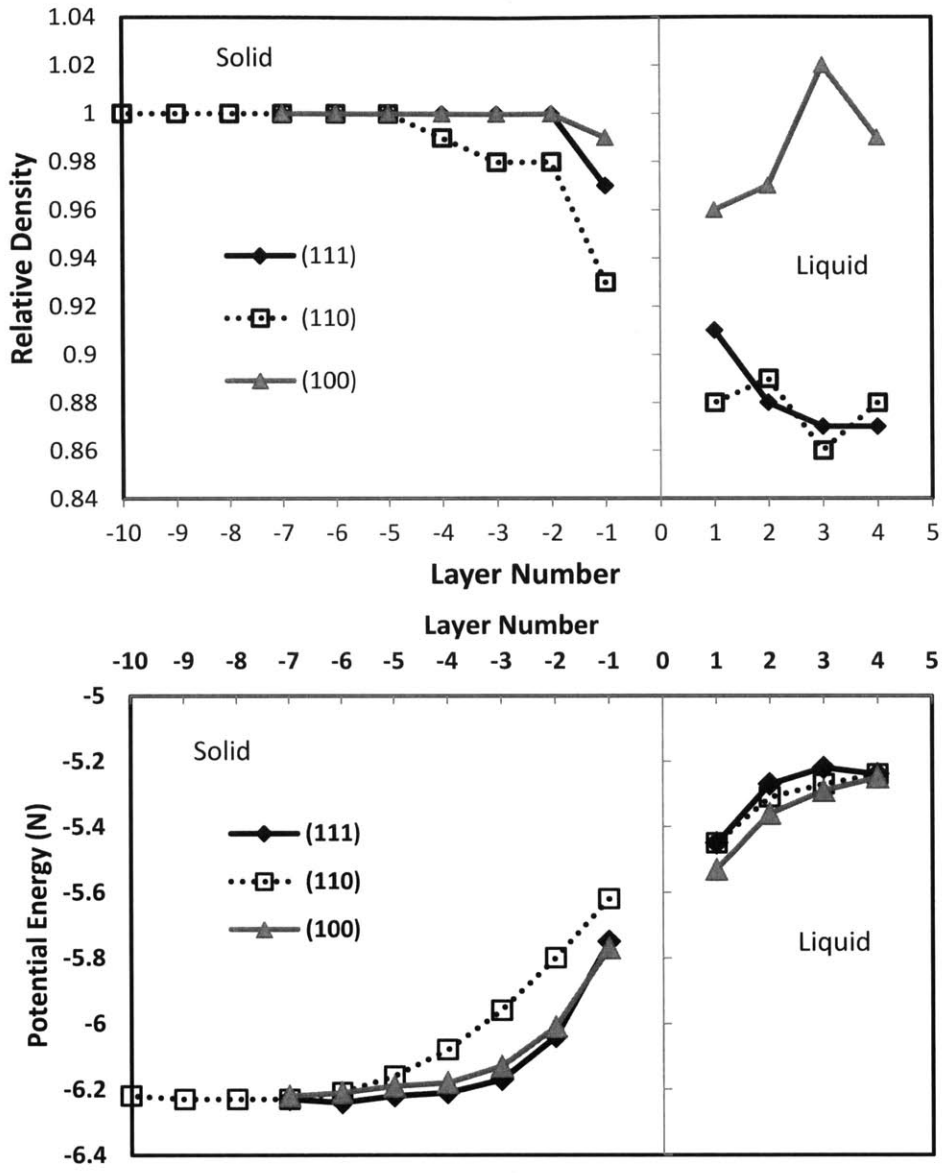

Figure 44. Summary of data from Broughton and Gilmer[98] The density of the bulk crystal is normalized to unity, such that the solid phase is on the left and the liquid phase is on the right.

6.4 Digilov Model and Application

While Turnbull empirically found that the ratio $\gamma_{SL}V_{ms}^{2/3}N_A^{1/3}/\Delta H_m$ for metals is relatively constant and equal to 0.45,[96] Digilov later derived a model for the solid-liquid interfacial energy shown in Eq. (37) which shows that the ratio can be related to material properties with a fitted constant, d^2,[88] where $d^2 = d_{SL}^2/d_L^2$, d_{SL}^2 is the mean-square amplitude of thermal vibrations in the solid-liquid interface, and d_L^2 is the mean-square amplitude in the liquid phase. The derivation assumes vibrational changes contribute most significantly to the energy change of the transition region at the interface. Although it assumes monatomic species, it can be approximated that larger molecules behave similarly.

Equation (37) implies that plotting the Turnbull coefficient, $\frac{\gamma_{SL}V_{m,sol}^{2/3}N_A^{1/3}}{\Delta H_m}$, versus $\frac{3R}{2\Delta S_{m,bulk}}\exp\left(\frac{\Delta S_{m,bulk}}{3R}\right)$ for different substances should result in a straight line with a zero intercept and slope equal to d^2, assuming d^2 is constant for all the substances. For simplicity, the bulk ΔS_m is used, although this value may vary somewhat with pore size.

Indeed, Figure 45 demonstrates that metals, semimetals and water fall roughly on a line that intersects at the origin, giving a fitted d^2=0.248 for these classes of substances. All of the nano-confined organic compounds fall significantly below the metal Turnbull coefficients, which together can be fit with a d^2 value of 0.110. Empirically, we observe that the organic compounds group into two separate regions which can be fit well by the correlation, although the data is limited. One grouping consists of benzene, chlorobenzene, cyclohexane, and trans-decalin, while the second grouping consists of naphthalene and heptane. We show later that nano-confined ibuprofen falls within this second grouping. The first grouping can be fit with d^2=0.143, and the second grouping can be fit with d^2=0.058. Cis-decalin was not included in the analysis as the solid molar volume could not be found.

In either case, organic compounds confined inside of nanopores have significantly lower Turnbull coefficients compared to particles of metals or semimetals in a homogeneous melt. Physically, a smaller d^2 value suggests that compounds undergo a much larger relative decrease in thermal vibration amplitude upon freezing compared to metals, semimetals and water. We were unable to find a distinguishing characteristic to account for this apparent segmentation of organic compounds using physicochemical properties (e.g. ΔV_m, $\Delta H_{f,bulk}$, $T_{f,bulk}$, or dipole moment).

Table 10 summarizes the fitted d^2 values for the different compound types determined from this current work. It will be of interest to measure experimental Turnbull coefficients of several more organic compounds to determine if the correlation and initial groupings continue to hold.

$$(37)\ \frac{\gamma_{SL} V_{m,sol}^{2/3} N_A^{1/3}}{\Delta H_m} = \frac{3R}{2\Delta S_{m,bulk}} d^2 \exp\left(\frac{\Delta S_{m,bulk}}{3R}\right)$$

Table 10. Fitted d^2 Values for different compound types

Compound type	Fitted d^2 Value
Metals, Semimetals, Water	0.248
Organics Confined in Nanopores	0.110
Organics Group 1	0.143
Organics Group 2	0.058

To employ these correlations, one can simply use the bulk ΔS_m of the material with the appropriate d^2 value to obtain the Turnbull coefficient, and hence the value of $\gamma_{SL}/\Delta H_m$ which has been shown to be relatively invariant with pore size. This coefficient can then be substituted into the Gibbs-Thomson equation to predict freezing point changes for an organic fluid confined to a nanopore of a specific size. Using this correlation, a parity plot can be generated for these organic substances (Figure 46). The calculated ΔT_f at each pore radius using the Turnbull coefficient generated from Figure 45 is plotted versus the experimental ΔT_f showing fairly good agreement.

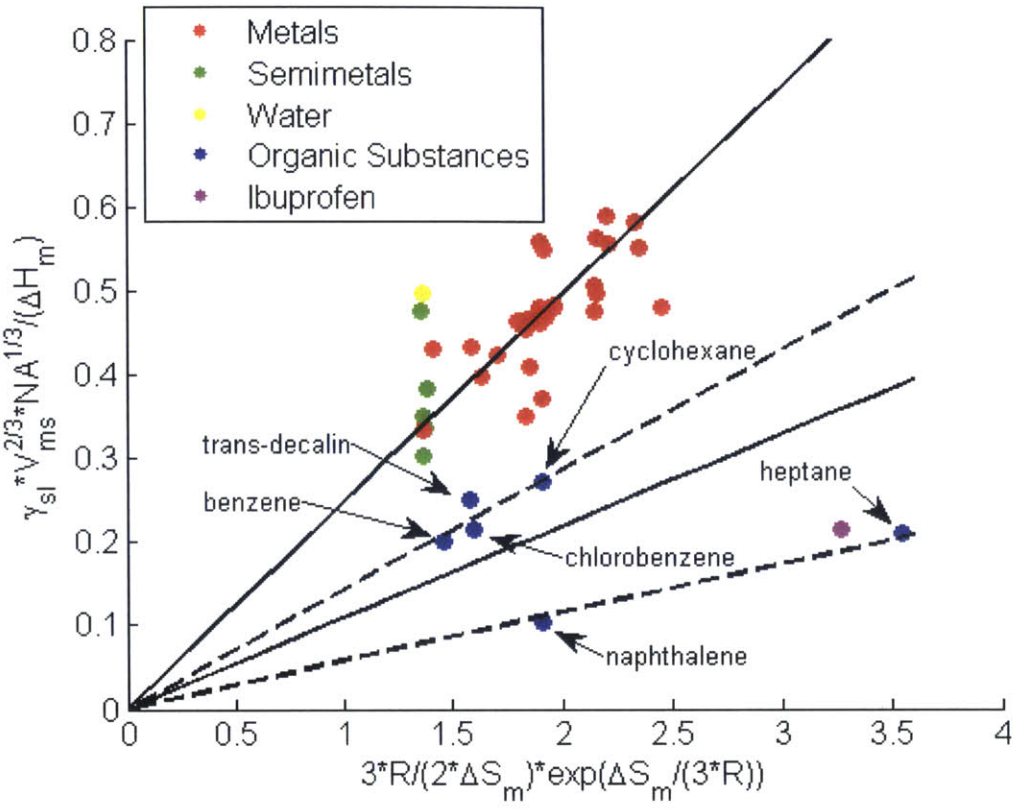

Figure 45. A plot of metal, semimetals, water, and organic substances show that metals, semimetals, and water follow the correlation found in Digilov's original model. The nano-confined organic substances fall significantly below the metals, semimetals, and water, and they can be fitted to the correlation in Eq. (37) using a different d^2 value. The organic compounds appear to segregate into two groups, and separate correlations are plotted for each, as indicated by the dashed lines. The fitted lines have fixed the y-intercept at zero.

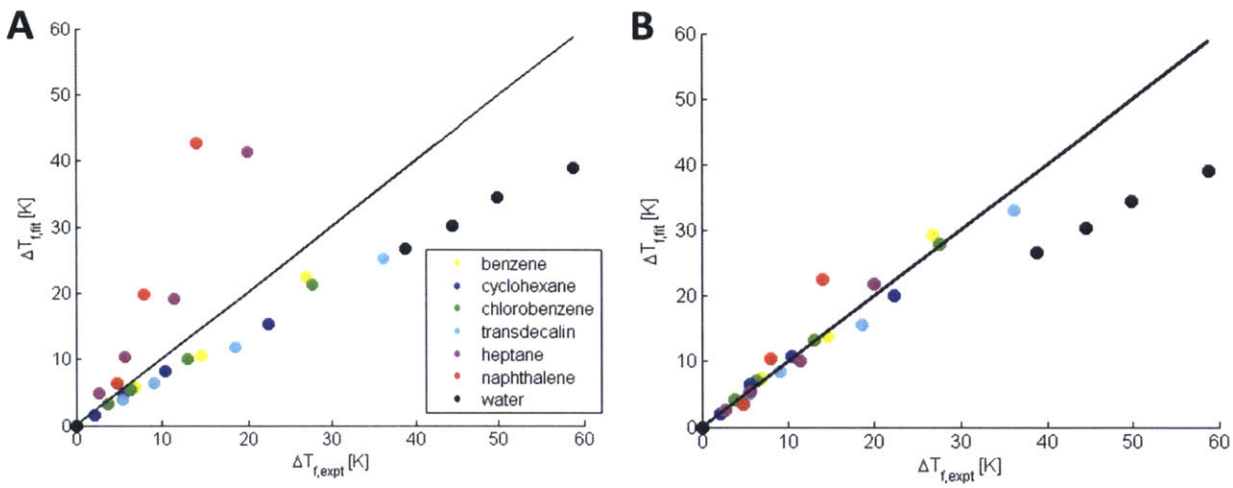

Figure 46. Parity plots showing the predicted ΔT_f versus the experimental ΔT_f. The predicted ΔT_f is found using the correlations of Eq. (37) and the fitted d^2 value in Table 10, with data from Figure 45, to obtain the Turnbull coefficient ($\gamma/\Delta H_m$), which are used in Eq. (27) to calculate the predicted freezing point depression. In both plots, the fitted d^2 value for metals, semimetals and water is used to compute the Turnbull coefficient for water. (A) ΔT_f calculated using the fitted d^2 value for all the organic compounds. (B) ΔT_f calculated using separate d^2 values for the two organic compound groups.

An application of this correlation is in predicting the size-dependent melting point for nanosized active pharmaceutical ingredients (APIs) inside nanoporous materials, as the melting point is related to solubility, an important property for bioavailability.[99] The freezing point of ibuprofen inside controlled pore glass (CPG) with average pore diameters ranging from 38 to 300 nm was measured using DSC, resulting in a very linear relationship between melting point depression and inverse pore radius (Figure 47).[100] Despite a melting enthalpy for the smaller pore sizes that decreases by as much as 23% compared to the bulk value, the Gibbs-Thomson equation still appears to hold. This data further supports the claim that the ratio $\gamma_{SL}/\Delta H_m$ is largely invariant with pore radius. The slope of the fitted line in Figure 47 is used to compute the non-dimensional Turnbull coefficient, and the bulk ΔS_m for ibuprofen is used to compute the x-axis value in Figure 45. Interestingly, ibuprofen lies relatively close to the correlation line for organic compounds (off by 40% of the predicted value), but it is quite far from the correlation line for metals. We note that ibuprofen appears to fall within the second grouping of organic compounds consisting of naphthalene and heptane. Thus, the presented correlation provides a useful estimate of how the melting point will change for organic compounds with pore size.

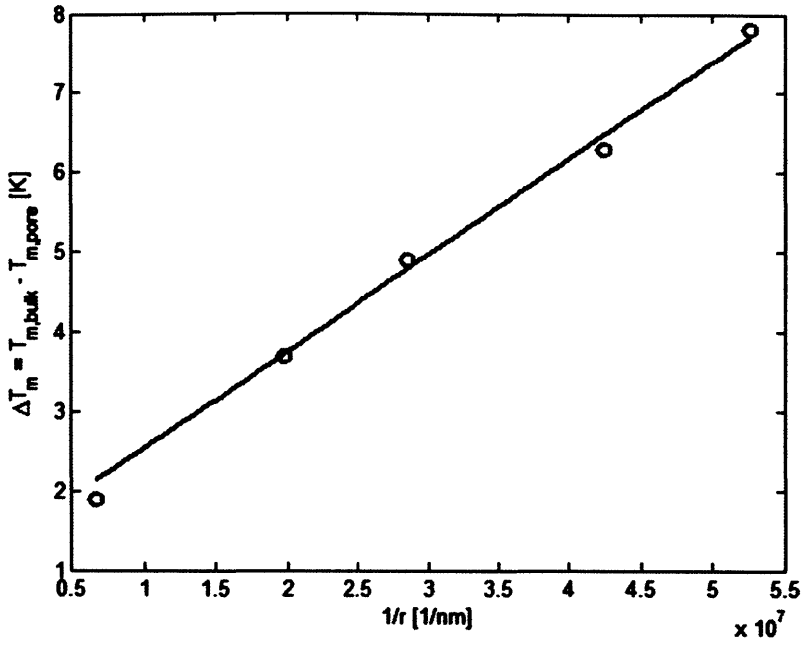

Figure 47. Freezing point depression versus inverse pore radius for ibuprofen inside controlled pore glass (CPG) of various average pore diameters. A linear relationship is observed.

The validity of the results presented in this paper, namely that the Turnbull coefficient is invariant with radius and the application of Digilov's correlation to estimate $\gamma_{SL}/\Delta H_m$ values, may not necessarily hold at pore diameters < 4 nm. In fact, there is surprisingly no mention of specific pore properties (e.g. pore composition) here. However, at smaller diameters, it is predicted that the pore structure and size can have a dramatic effect on the solid structure. For example, water confined to carbon nanotubes ranging between 0.9 and 1.7 nm in diameter experience a freezing point variation that is highly non-monotonic with pore size, and thus could not be explained by the Gibbs-Thomson model owing to the several discrete solid phases of ice that form at different diameters.[68]

6.5 Conclusion

The purpose of this study is to provide clarification to the nanopore field regarding the appropriate use of the Gibbs-Thomson equation for predicting freezing points and interpreting solid-liquid

surface energies—namely the fact that solid-liquid surface energies and enthalpies are predicted to vary with pore size, although the ratio of these two values are relatively invariant with pore size (>4 nm in diameter). The use of separate corrections for ΔH_m and γ_{SL} were shown to be inadequate for predicting freezing point depressions in nanopores. We further explain the first-order model for prediction of the Turnbull coefficient, the non-dimensional form of $\gamma_{SL}/\Delta H_m$, being equal to ½, which is very dependent on the assumptions regarding which phase is more affected energetically upon formation of the interface. The metal nucleation literature has decades of studies regarding analysis of solid-liquid surface free energies, which directly impact nucleation phenomena. We show that Digilov's model for metal nucleation can also predict fluid freezing behavior of organic substances inside of nanopores, albeit with a different fitting constant related to the change in thermal vibrations upon freezing. The results of this study will help enable freezing point estimation of various fluids inside of nanopores of different sizes.

7. Conclusions

The previous chapters have described advances on several fronts in nanopore research, specifically transport and phase behavior.

First, we have demonstrated the ability to study proton and ion transport in individual single-walled carbon nanotubes. Using voltage clamp techniques, the pore-blocking current, which is a lower-bound for the proton current, can be measured. The major conclusion is that the pore-blocking current varies significantly and non-monotonically with the nanotube diameter (1-2 nm).

In order to study transport more easily in nanopores without significant device fabrication effort, we developed a method to produce nanopores whereby a glass micropipette is patched onto a grooved PDMS surface. This pore size can be tuned depending on the force applied to the micropipette. The nanopore was characterized using patch clamp methods, and stochastic current fluctuations were observed, which were attributed to ionic vapor-liquid transitions.

Because of the possibility of an ionic vapor-liquid transitions in these PDMS nanopores, which isn't observed under typical conditions for bulk solutions, we explored the possibility of monitoring phase transitions inside of pure fluids (water) inside of small carbon nanotube nanopores (1-2 nm) where bulk thermodynamic equations do not apply. Unlike previous studies which explored phase transitions in bulk quantities of nanopores, we have measured phase transitions in single, isolated nanopores of well-characterized diameters using Raman spectroscopy as a probe. As with transport through carbon nanotubes, the change in phase transition temperatures compared to bulk varied significantly and non-monotonically with diameter.

At larger pore diameters (>4 nm), there has been confusion in the literature about the application of bulk thermodynamics relations, such as the Gibbs-Thomson equation, for predicting freezing point temperatures inside pores. Knowing the solid-liquid surface energy (γ_{SL}) and enthalpy of fusion (ΔH_{fus}) allows one to predict the freezing point depression, but many studies assume ΔH_{fus} to be constant inside the pore despite varying significantly with pore radius. We show, using experimental data in the literature, it is the ratio ($\gamma_{SL}/ \Delta H_{fus}$), not ΔH_{fus}, that is relatively invariant with pore radius.

7.1 Future Work

As this work and other studies show, all nanopores are not equal. At very small diameter ranges (<2 nm), where many interesting transport and phase transitions occur, small variations in nanopore diameter can have dramatic effects on pore properties. Unlike some porous materials which are made of amorphous material, carbon nanotubes and zeolites, for example, are crystals with well-defined sizes. The problem is that it is difficult to synthesize or separate carbon nanotubes to be all of the same chiral index (same diameter), although there has been recent progress towards this goal.[101] The work done in this thesis lays part of the groundwork for understanding the diameter-dependence of nanopore transport and phase behavior. Having a membrane consisting of pores of a single diameter will open up much more efficient membranes for desalination, proton-exchange, and molecular separations.

Likewise, the ability to control the phase transition temperature of fluids in nanopores and synthesize specific diameters of nanopores opens up the opportunity to create phase change materials using bulk quantities of single-diameter nanopores.

The ability to use individual carbon nanotubes as molecular sensors is also an intriguing prospect. This could be achieved through voltage clamp measurements and functionalizing the nanotube ends with specific-binding groups which modulate the impedance upon detection. Raman spectroscopy can also be used as a way to distinguish between different filled liquids inside nanotubes using the shift in Raman peak properties.

8. List of Publications

8.1 Main Author/ Contributor

- **Shimizu, S.**; Agrawal, K.V.; Kilcoyne, D.; Drahushuk, L.; Strano, M. S., Raman spectroscopic observation of phase changes of water inside an individual carbon nanotoube. (in preparation)
- **Shimizu, S.**; Manohar, N.; Strano, M. S., Analysis of freezing point changes in fluids confined to nanopores. (in preparation)
- **Shimizu, S.**; Strano, M. S., The Structubent: a nanocomposite solution to compressed natural gas storage. Advanced Engineering Materials, 2014 (published online).
- Choi, W.; Ulissi, Z. W.; **Shimizu, S. F. E.;** Bellisario, D. O.; Ellison, M. D.; Strano, M. S., Diameter-dependent ion transport through the interior of isolated single-walled carbon nanotubes. Nat Commun 2013, 4.
- **Shimizu, S.**; Ellison, M.; Aziz, K.; Wang, Q. H.; Ulissi, Z.; Gunther, Z.; Bellisario, D.; Strano, M., Stochastic Pore Blocking and Gating in PDMS–Glass Nanopores from Vapor–Liquid Phase Transitions. The Journal of Physical Chemistry C 2013, 117 (19), 9641-9651.
- **Shimizu, S.**; Choi, W.; Abrahamson, J. T.; Strano, M. S., New concepts in molecular and energy transport within carbon nanotubes: Thermopower waves and stochastically resonant ion channels. physica status solidi (b) 2011.
- **Shimizu, S.**; Song, C.; Strano, M., Role of Specific Amine Surface Configurations for Grafted Surfaces: Implications for Nanostructured CO2 Adsorbents. Langmuir 2011, 27 (6), 2861-2872.

8.2 Secondary Author/Contributor

- Hilmer, A. J.; Bellisario, D. O.; **Shimizu, S.**; McNicholas, T. P.; Wang, Q. H.; Speakman, S. A.; Strano, M. S., Formation of High-Aspect-Ratio Helical Nanorods via Chiral Self-Assembly of Fullerodendrimers. The Journal of Physical Chemistry Letters 2014, 5 (5), 929-934.
- Zhang, J.; Kruss, S.; Hilmer, A. J.; **Shimizu, S.**; Schmois, Z.; De La Cruz, F.; Barone, P. W.; Reuel, N. F.; Heller, D. A.; Strano, M. S., A Rapid, Direct, Quantitative, and Label-Free Detector of Cardiac Biomarker Troponin T Using Near-Infrared Fluorescent Single-Walled Carbon Nanotube Sensors. Advanced Healthcare Materials 2014, 3 (3), 412-423.
- Wang, Q. H.; Bellisario, D. O.; Drahushuk, L. W.; Jain, R. M.; Kruss, S.; Landry, M. P.; Mahajan, S. G.; **Shimizu, S. F. E.**; Ulissi, Z. W.; Strano, M. S., Low Dimensional Carbon Materials for Applications in Mass and Energy Transport. Chemistry of Materials 2013, 26 (1), 172-183.
- Jain, R. M.; Howden, R.; Tvrdy, K.; **Shimizu, S.**; Hilmer, A. J.; McNicholas, T. P.; Gleason, K. K.; Strano, M. S., Polymer-Free Near-Infrared Photovoltaics with Single Chirality (6, 5) Semiconducting Carbon Nanotube Active Layers. Advanced Materials 2012.
- Paulus, G. L. C.; **Shimizu, S.**; Abrahamson, J. T.; Zhang, J.; Hilmer, A. J.; Strano, M. S., The chemical engineering of low-dimensional materials. AIChE Journal 2011, 57 (5), 1104-1118.

- Ulissi, Z. W.; **Shimizu, S.**; Lee, C. Y.; Strano, M. S., Carbon Nanotubes as Molecular Conduits: Advances and Challenges for Transport through Isolated Sub-2 nm Pores. The Journal of Physical Chemistry Letters 2011, 2 (22), 2892-2896.
- Jin, Z.; McNicholas, T. P.; Shih, C.-J.; Wang, Q. H.; Paulus, G. L. C.; Hilmer, A. J.; **Shimizu, S.**; Strano, M. S., Click Chemistry on Solution-Dispersed Graphene and Monolayer CVD Graphene. Chemistry of Materials 2011, 23 (14), 3362-3370.
- Choi, W.; Lee, C. Y.; Ham, M.-H.; **Shimizu, S.**; Strano, M. S., Dynamics of Simultaneous, Single Ion Transport through Two Single-Walled Carbon Nanotubes: Observation of a Three-State System. Journal of the American Chemical Society 2010, 133 (2), 203-205.

9. Appendices

Part of my research has focused on other condensed phases, such as those formed by adsorption, and the following appendix sections detail two of these studies. In section 9.1, titled "Modeling of Amine-Grafted CO_2 Adsorbents", the adsorption problem faced in solid amine-based CO_2 adsorbents is analyzed, where a CO_2 molecule can only be adsorbed if there are two adjacent amine groups present. An adsorption isotherm is developed which can be used to predict the adsorption capacity of an arbitrary nanostructured amine adsorbent. This model is used to provide insight into the design of optimal amine-based CO_2 adsorbents.

Section 9.2, titled "The Structubent: A Nanocomposite Solution for Compressed Natural Gas Storage", details another adsorption problem, which involves the analysis of the shell of a compressed natural gas (CNG) cylinder which combines a nanoporous adsorbent and structural material. While maintaining the same structural integrity as an inert container shell, it is shown that under certain circumstances, it is possible to achieve higher mass- and volume-specific capacities which are the key figures of merit for CNG vessels.

9.1 Modeling of Amine-Grafted CO_2 Adsorbents

9.1.1 Introduction

There is renewed interested in materials and processes that adsorb and capture carbon dioxide from, for example, combustion streams or other emission sources.[102] One of the earliest methods to capture acid gases, such as CO_2, from gas streams dates as far back as the 1930's where a basic liquid amine/water solution is used to chemically absorb the acid gas, CO_2; heating the solution regenerates a relatively pure CO_2 gas stream to be sequestered or used elsewhere.[103-106] The main drawback comes from the large energy requirements required for heating the large volume of liquid to desorb the CO_2.[106] A proposed solution first carried out by Leal et al. is to use very porous solids with amine groups grafted on the surface as a CO_2 adsorbent.[107] It is believed that using solids with grafted amines would increase the efficiency by reducing the energy required to heat up the

adsorbent compared to water.[102, 108] Also, because the amines are covalently bonded to the substrate, evaporative losses of amines due to heating would be minimal.[102]

To date, there has been much experimental work in grafting amines onto porous substrates and characterizing their adsorption properties. Zelenak et al. and Choi et al. give concise accounts of most of the recent experimental work involving amine-grafted adsorbents.[102, 109] However, there has been little theory developed to explain the equilibrium adsorption characteristics. To the best of our knowledge, the only adsorption isotherm model developed for CO_2 adsorption was a semi-empirical one proposed by Serna-Guerrero et al.[110] It involves separating the total uptake into chemisorption and physisorption contributions, and the individual adsorption isotherms for each process are given the functional form of the Toth equation.[111] The uptake due to physisorption is approximated as being the uptake for the ungrafted substrate material corrected for the different surface areas between the ungrafted and grafted adsorbent materials. Then, the actual adsorption data with physisorption contributions subtracted is fitted to the chemisorption isotherm equation, and the fitted parameters are related to the strength of adsorbate-adsorbent interactions and the surface heterogeneity.[110] The disadvantage of this type of model is that the underlying isotherm equation (in this case, the Toth equation) does not accurately reflect the chemistry that is occurring at the surface, namely the reaction of adjacent amine groups, and thus, the fitted parameters do not have a clear physical connection with the reaction that is actually occurring. Their model also does not have a built-in reason to explain how increasing amine densities lead to more than proportional increase in CO_2 uptake (an increase in amine binding efficiency), which is observed experimentally by Hiyoshi et al.[112]

Thus, there have been no models proposed that are related to the chemistry occurring at the molecular level. In this study, we examine anhydrous, dry CO_2 chemisorption on surfaces grafted with amines, although the analysis could be applied to any adsorption problem with a similar chemistry. The analysis also applies to adsorption at temperatures above which there is no adsorbed water phase on the adsorbent surface. While this model applies strictly to anhydrous CO_2 adsorption, there is still reasonable application of the model to adsorption under humid conditions. Under a dry CO_2 stream, there is only one chemical reaction taking place, which involves reaction of two adjacent amine groups with CO_2 to form alkylammonium alkylcarbamates, as depicted in Eq. (38) and written as:

(38) $CO_2(g) + NH_2R = + NH_2R = \underset{k_{-1}}{\overset{k_1}{\rightleftharpoons}} NH_3^+R = + NHCOO^-R =$

in the case of a primary amine. The literature supports this claim through experimental FT-IR studies, thermodynamic considerations, and ab-initio calculations, and they find the possibility of forming a carbamic acid species (RNH_2CO_2H) or zwitterion species ($RNH_3^+CO_2^-$) to be negligible.[107, 113-115] Figure 48 shows a single step-mechanism for this reaction, which has been suggested elsewhere.[113, 116] Although fitting the adsorption data to existing isotherms may result in a better fit, the derived parameters have no physical basis (e.g., they might assume a CO_2 molecule can adsorb to a single amine group). The fitted equilibrium constants in the proposed model are a first-order approximation to the actual equilibrium constant which controls for the unique requirement that adjacent amines are required for successful adsorption.

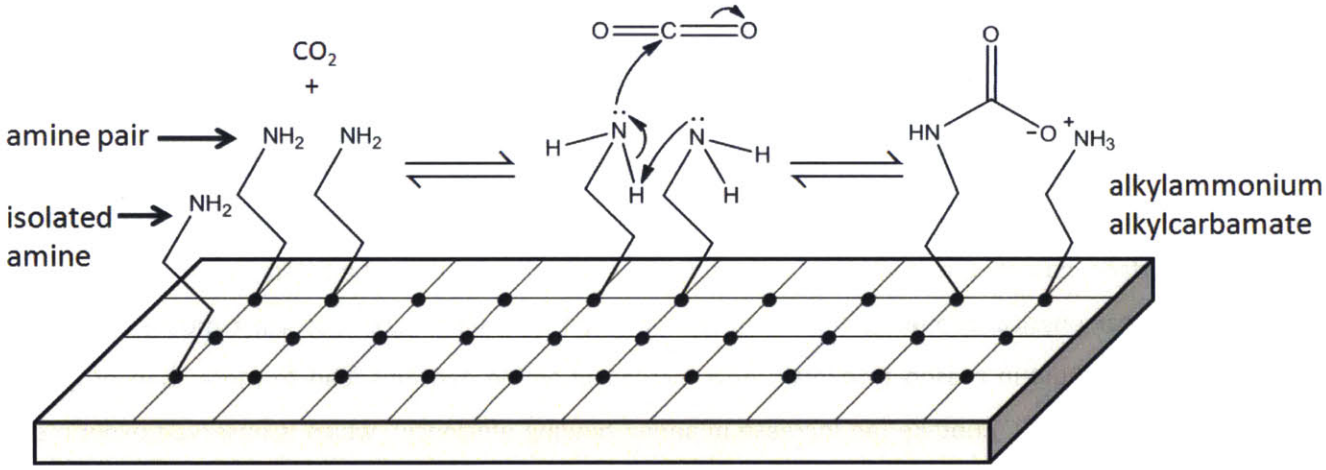

Figure 48.Schematic of reaction of anhydrous CO_2 on amine-grafted surface.

This situation is unique compared to other chemisorption systems in that: 1) dry CO_2 must adsorb onto two adjacent amine groups, and 2) the active surface for chemisorption of CO_2 is based on the prior chemisorption of amine groups on the initial substrate surface. Thus, the initial surface configuration of amine groups can have a critically important role in how much CO_2 can be adsorbed.

One reason that an adsorption isotherm taking the chemistry in Eq. (1) into account has not yet been proposed is the enormous difficulty of solving the problem analytically. Because CO_2 requires

two sites when it adsorbs, the problem is essentially the adsorption of a dimer on a surface. Given a fixed chemical potential (or pressure) of the dimer species, the problem of finding the equilibrium surface coverage of the dimer on an empty, homogeneous lattice with no lateral interactions has been the subject of significant study, and an analytical solution has only been found in the case of a 1-D line of sites.[117-120] Attempts at solving this problem have usually involved complex statistical mechanical theories where the partition function is evaluated using various approximations, and the formulae of statistical mechanics are applied to generate the adsorption isotherm of surface coverage (θ) as a function of chemical potential (μ). Currently, the most accurate approximation of the adsorption isotherm on a surface with all sites available for adsorption is the Occupation Balance method by Roma, et al.[120-121] However, when the underlying surface is only partly active (e.g. there may be patches of active groups available to adsorb a dimer), the problem becomes quite difficult, as shown in studies of a similar problem which concerns dimer adsorption onto heterogeneous surfaces.[122-123] Another problem is that the isotherms derived in these studies are relatively complicated expressions that cannot be written easily in the familiar form of surface occupancy, θ, as an explicit function of pressure (e.g. the Langmuir adsorption isotherm) and thus, difficult for an experimentalist to apply. Our goal in this study is to present a novel approach toward predicting the adsorption characteristics of dimers (CO_2) for any arbitrary active group (amine) surface configuration that experimentalists can easily use to describe their data and screen potential adsorbents based on their expected surface configuration.

9.1.2 Theoretical Basis

As discussed previously, the adsorption of CO_2 requires adjacent amine groups to react, so the surface configuration of covalently bonded amines is an important consideration. In the following analysis, we assume: 1) the initial porous substrate material can be represented as a discrete 2-D lattice, 2) interaction energies are negligible, 3) physisorption is negligible at low pressures, 4) all potential amine pairs are equivalent, 5) the underlying surface is homogeneous, and 6) the products formed in Eq. (1) can only pair with each other to desorb (i.e., an alkylcarbamate group cannot pair with just any alkylammonium group surrounding it). If physisorption is significant, control experiments on the ungrafted substrate will still make the model applicable, as discussed in the Results section. Furthermore, the model can also be extended to describe multilayers of amines,

diamines, triamines and other polyamines using slightly different fitting conditions, as discussed later.

It is a difficult problem to quantitatively describe an arbitrary surface configuration using less information than an actual snapshot of the surface. In this study, we wanted to find the simplest set of parameters to describe a surface that would also sufficiently describe CO_2 adsorption. One option that was considered was the radial distribution function (RDF), which describes the variation in density as a function of distance averaged over each occupied site. However, the RDF contains little useful information about how the number of potential amine pairs will evolve during the course of the reaction.

A better way to describe a surface is to make a histogram showing the fraction of amines having z number of nearest neighbors, which will be henceforth referred to as the z-histogram. This study considers three lattice types: hexagonal, square and triangular, where the maximum number of nearest neighbors, z_{max}, is 3, 4 and 6, respectively. For each lattice type, the z-histogram bins range from z = 0 (no nearest neighbors) to $z = z_{max}$ (completely surrounded) in integer steps. Also, let α_z be the fraction of total amines for each z-value. One might expect that if adjacent amine sites are the only important factors in CO_2 adsorption, knowledge of the initial distribution of sites with a specific number of nearest neighbors would give sufficient information. A sample initial surface configuration and its corresponding RDF and z-histogram are shown in Figure 49 to illustrate the two methods.

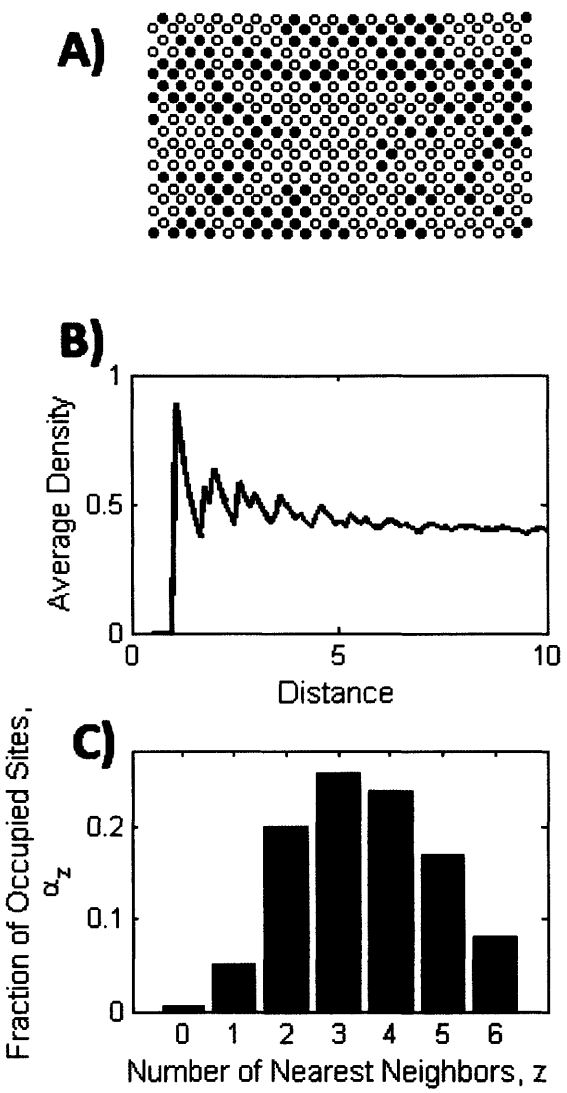

Figure 49. (A) A random surface configuration (black dot = an amine group, white dot = an empty site). (B) RDF of the corresponding surface. (C) Nearest neighbor histogram (z-histogram) of the corresponding surface.

Assuming for now that the z-histogram uniquely determines the resulting adsorption isotherm of the surface, then a surface that is partitioned into smaller sub-surfaces of constant-z (constant number of nearest neighbors) with the same overall amine density could be devised that recreates the same z-histogram, and thus, also has the same adsorption characteristics. The essential idea behind this model simply involves fully characterizing these constant-z surfaces and having the overall CO_2 uptake equal the uptake due to relative proportions of constant-z surfaces.

The derivation of the adsorption isotherm equation begins with writing the equilibrium expression for the reaction in Eq. (39) as

$$(39)\ K = \frac{k_1}{k_{-1}} = \frac{\theta_{prodpairs}}{P_{CO_2}\theta_{pairs}}$$

where K is the equilibrium constant, $\theta_{prodpairs}$ is the number of product pairs divided by the total number of sites on the surface, θ_{pairs} is the number of apparent amine pairs divided by the total number of sites on the surface, and P_{CO2} is the equilibrium pressure of CO_2. To put these terms in a more familiar context, the site balance for this problem at any time may be written as

$$(40)\ \theta_{amine,0} = 2 \cdot \theta_{prodpairs} + k \cdot 2 \cdot \theta_{pairs} + \theta_{isolated\ amines}$$

where $\theta_{amine,0}$ is the overall amine loading, the factors of two are due to there being two groups associated for each pair, and $\theta_{isolated\ amines}$ is the fraction of surface sites occupied by unpaired amine groups. This balance requires a non-constant variable k, which relates the number of apparent amine pairs to the actual number of contributing amine groups; thus, k is some complicated function of the extent of reaction and the initial surface configuration of amines.

Unlike the case of Langmuir adsorption, the number of potential adsorption sites (amine pairs) is not conserved. As an example, for a completely filled square lattice, if one amine pair reacts, the number of amine pairs decreases by seven (one pair that reacted plus six surrounding pairs); for a lone amine pair, however, a single reaction results in the loss of a single amine pair. At equilibrium, the value of θ_{pairs} at a specific θ_{rxn} (net number of forward reactions divided by the total number of sites) is constant for a given initial surface configuration. Thus, one can write

$$(41)\ \theta_{pairs} = f(\theta_{rxns})$$

where f is some arbitrary, monotonically decreasing function whose form depends on the initial surface configuration of amine groups.

If one assumes that a single product pair forms with each forward reaction as mentioned in the assumptions stated above, then

$$(42)\ \theta_{prodpairs} = \theta_{rxn} = \theta_{CO_2}$$

where θ_{CO2} is the number of CO_2 molecules adsorbed divided by the total number of sites. Combining these results, one can rearrange Eq. (39) in terms of θ_{CO2}:

$$(43)\ K = \frac{\theta_{prodpairs}}{P_{CO_2}\theta_{pairs}} = \frac{\theta_{rxn}}{P_{CO_2} f(\theta_{rxn})} = \frac{\theta_{CO_2}}{P_{CO_2} f(\theta_{CO_2})} \Rightarrow \theta_{CO_2} = h\left(K \cdot P_{CO_2}\right)$$

Eq. (43) shows that θ_{CO2} can be written as some arbitrary function, h, of non-dimensional pressure, $K*P_{CO2}$.

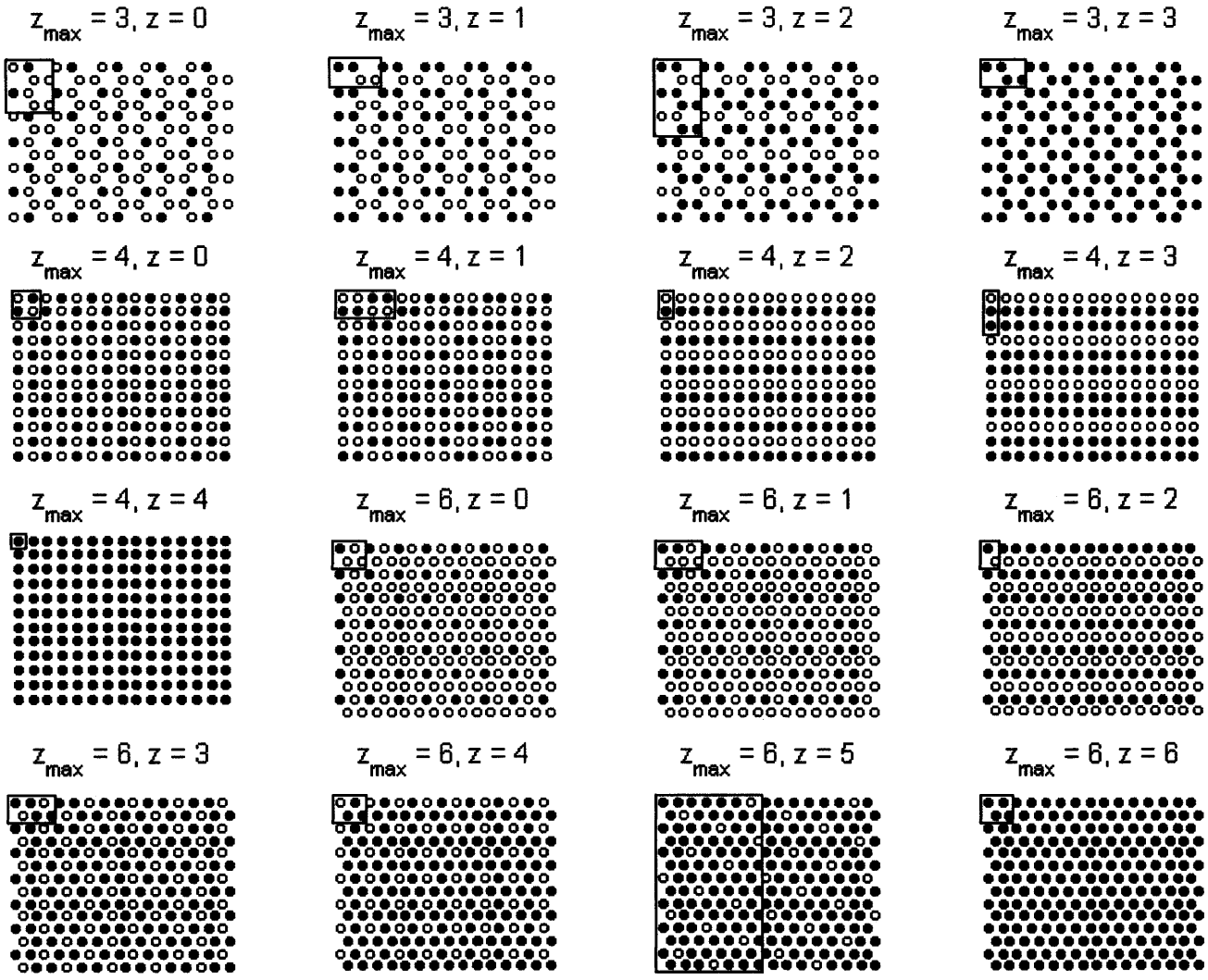

Figure 50. Constant-z surfaces for different lattice types (black dots = amine group, white dots = empty sites). Rectangles indicate unit cells for the surface.

Before proceeding with the derivation, we first determine the constant-z surfaces. The constant-z surfaces are depicted in Figure 50 for each lattice type, along with the unit cells. These constant-z surfaces were defined so that they have the maximum density of amines. For example, it is possible for isolated amine sites in a $z_{max} = 3$, $z = 0$ surface to be separated further and still be a $z = 0$ surface, but as will be discussed later, decreasing the surface density of constant-z surfaces limits the range of adsorption isotherms that can be predicted or fitted. One should also note that in a large lattice composed of different proportions of constant-z surfaces, deviations due to edge groups with a different number of nearest neighbors become completely negligible.

If one knows the initial, overall surface fraction of amines (number of amines divided by the total number of sites), $\theta_{amine,0}$, and the surface is covered by constant-z surfaces, then $\theta_{amine,0}$ can be written as

$$(44)\ \theta_{amine,0} = \sum_{z=0}^{z_{max}} \theta_z \cdot \frac{A_z}{A_{total}} = \sum_{z=0}^{z_{max}} \theta_z \cdot \beta_z$$

where θ_z is the amine surface fraction of a specific constant-z surface, and A_z/A_{total} is the fractional area of the total surface occupied by a specific constant-z surface, which will be denoted as β_z. This β_z value is related to the corresponding α_z value through

$$(45)\ \alpha_z = \frac{\text{number of amines with z nearest neighbors}}{\text{total number of amines}} = \frac{\theta_z \cdot A_z}{\sum_{z=0}^{z_{max}} \theta_z \cdot A_z} = \frac{\theta_z \cdot \beta_z}{\sum_{z=0}^{z_{max}} \theta_z \cdot \beta_z} = \frac{\theta_z \cdot \beta_z}{\theta_{amine,0}}$$

Using these relationships, we can continue from Eq. (44) to write the overall contributions of CO_2 uptake due to constant-z surfaces as

$$(46)\ \theta_{CO_2} = \sum_{z=0}^{z_{max}} h_z\left(K \cdot P_{CO_2}\right) \cdot \frac{A_z}{A_{total}} = \sum_{z=0}^{z_{max}} h_z\left(K \cdot P_{CO_2}\right) \cdot \beta_z$$

where $h_z\left(K \cdot P_{CO_2}\right)$ are the adsorption isotherm functions for a constant-z surface in terms of dimensionless pressure, $K*P_{CO2}$, which will be referred to as h-curves. After substituting Eq. (45) into Eq. (46), one obtains the final form of the adsorption equation:

$$(47)\ \theta_{CO_2} = \theta_{\text{amine},0} \sum_{z=0}^{z_{\max}} h_z \left(K \cdot P_{CO_2}\right) \cdot \frac{\alpha_z}{\theta_z}$$

This equation can be used to predict adsorption isotherms for a given surface configuration and fit adsorption data. Note that the h-curves for each constant-z surface in Figure 50 only need to be simulated once.

9.1.3 Simulation Procedure

A simulation was performed to generate empirical expressions for the h-curves. This Monte Carlo simulation was performed in the grand canonical ensemble using the Metropolis algorithm. The probabilities of adsorption and desorption of CO_2 are given by

$$(48)\ P_{adsorption} = \min\left\{\exp\left[\frac{1}{k_b T}\left(\mu - E_{N+1} + E_N\right)\right], 1\right\} = \min\left\{\exp\left[\frac{1}{k_b T}\left(\mu - \Delta E\right)\right], 1\right\}$$

$$(49)\ P_{desorption} = \min\left\{\exp\left[\frac{1}{k_b T}\left(-\mu + E_N - E_{N-1}\right)\right], 1\right\} = \min\left\{\exp\left[\frac{1}{k_b T}\left(-\mu + \Delta E\right)\right], 1\right\}$$

where k_b is Boltzmann's constant, T is the absolute temperature, μ is the chemical potential of the gas, and $\Delta E = E_{N+1} - E_N = E_N - E_{N-1}$ is the energy difference of the lattice when a CO_2 molecule is adsorbed onto the surface.[124] Since the model assumes no lateral interactions, the value of ΔE is a constant throughout the simulation.

For a single step in the simulation, a list of all potential amine pairs and product pairs (adsorbed CO_2 groups) was generated, and a random pair was chosen. If it was an amine pair, a random number was generated between 0 and 1; if this random number was less than $P_{adsorption}$ as calculated in Eq. (48), then a CO_2 molecule was adsorbed onto that amine pair. On the other hand, if a product pair was chosen and the random number was less than $P_{desorption}$ as calculated in Eq. (49), then the CO_2 group was desorbed. After each successful adsorption or desorption, the list of the amine and product pairs was updated. For the simulation of each constant-z surface, a lattice size was used such that the surface contained approximately 10,000 amine groups. Periodic boundary conditions were also employed. These simulation conditions were sufficient to make the finite size effects

negligible. For a specific $\mu - \Delta E$ value, 5 x 10^5 to 1 x 10^6 of these steps were performed to reach equilibrium, and then a further 5 x 10^5 to 1 x 10^6 steps were performed, during which the average θ_{CO2} and average θ_{pairs} were computed. By rearranging Eq. (39), one obtains

$$(50)\ K \cdot P_{CO_2} = \frac{\theta_{CO_2}}{\theta_{pairs}}$$

which allows one to calculate the K^*P_{CO2} value from the equilibrium θ_{CO2} and θ_{pairs} for each $\mu - \Delta E$ value. For each constant-z surface, the $\mu - \Delta E$ values that were used ranged approximately from -5 to 5.

From the simulation of each constant-z surface, the set of points (K^*P_{CO2}, θ_{CO2}) was generated which is the simulated adsorption isotherm in terms of non-dimensional pressure, K^*P_{CO2}. These data were fitted to an empirical equation given by

$$(51)\ \theta_{CO_2} = h_z\left(K \cdot P_{CO_2}\right) = \frac{\frac{\theta_z}{2} \cdot b \cdot \left(K \cdot P_{CO_2}\right)^{1/m}}{1 + b \cdot \left(K \cdot P_{CO_2}\right)^{1/m}}$$

which resembles the Sips equation,[125] where b and m are empirical parameters. There was no theoretical reason for using this form other than goodness of fit and the following limit is finite:

$$(52)\ \lim_{\left(K \cdot P_{CO_2}\right) \to \infty} \left[\theta_{CO_2}\right] = \frac{\theta_z}{2}$$

However, the isotherm does not allow a finite slope at zero pressure, which is physically inaccurate.[126-127] In the limit of infinite pressure, the adsorbed layer will become completely ordered, such that all the amine sites are occupied for constant-z surfaces with z > 0, and Eq. (52) shows this limit. This functional form fit the data very well, as shown in Figure 51 in the case of a triangular lattice at both high and low non-dimensional pressures. It should be noted that no simulation data is needed for a z = 1 surface since pairs are actually conserved in this case, and the adsorption isotherm reverts to a Langmuir isotherm equation. Additionally, for the z = 0 surface, there can be no adsorption, so θ_{CO2} is zero at all values of K^*P_{CO2}. The fitted parameters for all lattice types are shown in Table 11. While the results for honeycomb and square lattices are presented for

the sake of completeness, it is believed that if no other knowledge of the surface is known, the triangular lattice allows a close-packed configuration of amine groups and wider range of possible surface configurations. Thus, the following analysis only employs the triangular lattice for fitting data and making predictions.

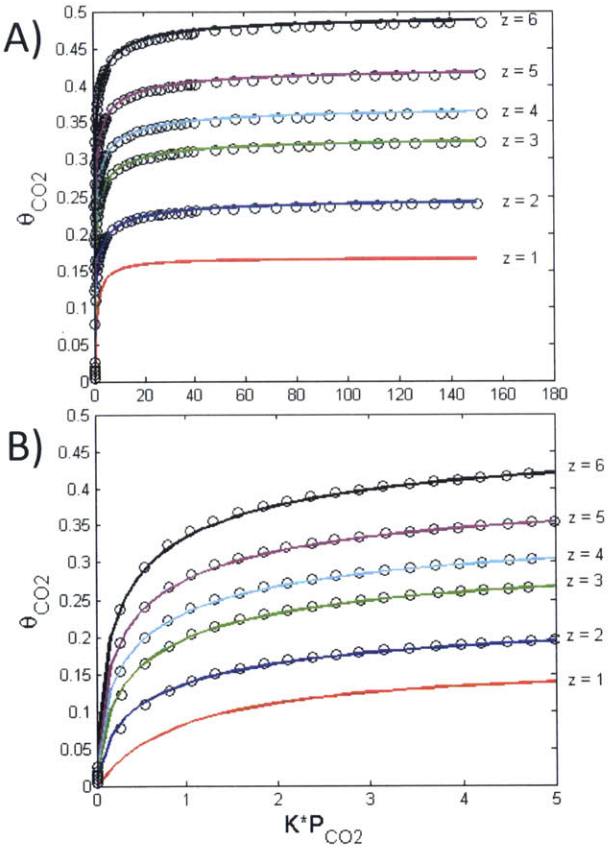

Figure 51. Fitted simulation data for the constant-z surfaces of a triangular lattice (z_{max} = 6) in a (A) moderately high pressure region and (B) a low pressure region.

Table 11. Fitted parameters (b and m) and amine surface fractions (θ_z) for each constant-z surface

z_{max}	z	b	m	θ_z
3	0	0		1/4
	1	1	1	1/2
	2	1.2232	1.5509	2/3
	3	1.4654	1.5735	1
4	0	0.00		1/2
	1	1	1	1/2
	2	1.2229	1.5497	1/2
	3	1.5017	1.3711	2/3
	4	1.7106	1.5682	1
6	0	0		1/4
	1	1	1	1/3
	2	1.2236	1.5476	1/2
	3	1.4639	1.5729	2/3
	4	1.6403	1.6517	3/4
	5	1.8337	1.6727	6/7
	6	2.0171	1.6720	1

When fitting the data to the isotherm equation in Eq. (47), one varies K and the vector [α_z, z = 0,1,..,z_{max}-1]. Because the [α_z] sum to 1, there are only z_{max}-1 independent α_z values. The constraints that must be satisfied during the fitting process are:

(53) $K > 0$

(54) $0 \le \{\alpha_z, z = 0,1,\ldots, z_{\max} - 1\} \le 1$

(55) $\sum_{z=0}^{z_{\max}-1} \alpha_z \le 1$

(56) $\theta_{\text{amine},0} \le \dfrac{1}{\sum_{z=0}^{z_{\max}} \dfrac{\alpha_z}{\theta_z}}$

The constraint in Eq. (54) is present so that α_{zmax} cannot be negative. The constraint in Eq. (55) comes about because the maximum surface density of amines for a given z-histogram occurs when

there is no empty space on the surface (i.e., the surface is only made up of constant-z surfaces). Thus, the overall density must not exceed this maximum surface density given by the z-histogram. This constraint also demonstrates the reason that the most dense constant-z surfaces were chosen, as mentioned earlier, since they allow the widest possible range of $\theta_{amine,0}$ to be accommodated.[128] This constraint in Eq. (56) also gives the condition to determine if a given z-histogram is possible to reconstruct. For instance, if one wanted to know the adsorption isotherm of a surface with an arbitrary z-histogram and a specified $\theta_{amine,0}$, one could check if such a surface is even possible to construct by seeing if the constraint in Eq. (56) holds. If such a surface is possible, then one merely plugs in the z-histogram values, $[\alpha_z]$, into Eq. (47), the parameters from Table 11, and a specified K-value to determine the resulting adsorption isotherm.

This model can also be applied to fit data from multilayers of amines, diamines, triamines, and other polyamines—not just monolayer coverage. The difference is that since surface fractions only make sense for monolayer amine coverage, one must fit amine efficiencies ((C:N) = $\theta_{CO2}/\theta_{amine}$) versus pressure data. Furthermore, since there is no concept of surface fraction, the constraint in Eq. (56) need not apply, which actually makes the fitting process simpler.

9.1.4 Results

This model was used as a predictive tool to determine the surface configurations that give the maximum and minimum θ_{CO2} as a function of $K*P_{CO2}$, and $\theta_{amine,0}$, as shown in Figure 52A for the case of a triangular lattice. This procedure involved maximizing or minimizing θ_{CO2} at set values of $K*P_{CO2}$ and $\theta_{amine,0}$ by varying $[\alpha_z, z = 0:1:z_{max}-1]$. From this plot, the corresponding CO_2/amine ratio ranges can be obtained, as depicted in Figure 52B. When the $\theta_{amine,0}$ is low enough the amine groups can be arranged in any possible manner, allowing a wide range of CO_2/amine ratios to be achieved. However, as $\theta_{amine,0}$ becomes larger, the range of surface configurations possible becomes more limited because the surface is more crowded, thus making the range of possible CO_2/amine ratios narrower.

The maximum and minimum θ_{CO2} as a function of $\theta_{amine,0}$ for the case of low pressure ($K*P_{CO2}$ = 1) and moderately high pressure ($K*P_{CO2}$ = 100) are shown in Figure 52C-E and Figure 52F-H,

respectively (these are effectively cross-sections of Figure 52A). In addition, the compositions of each maximum and minimum surface in terms of fractional area of a constant-z surface are presented. One can see that the maximum surface composition changes between low pressure and moderately high pressure conditions due to the fact that at low pressures, it is better to have more apparent pairs (z = 6 surfaces are better than z = 1 surfaces). However, at higher pressures, isolated amines become more of an issue, and thus, having some z = 1 surfaces (isolated amine pairs) are preferable at certain amine loadings. This switch in the ideal surface composition occurs around K^*P_{CO2} = 6. At infinitely high pressures, there is no specific optimal surface configuration for a given amine loading, since all the amines become occupied as long as z > 0.

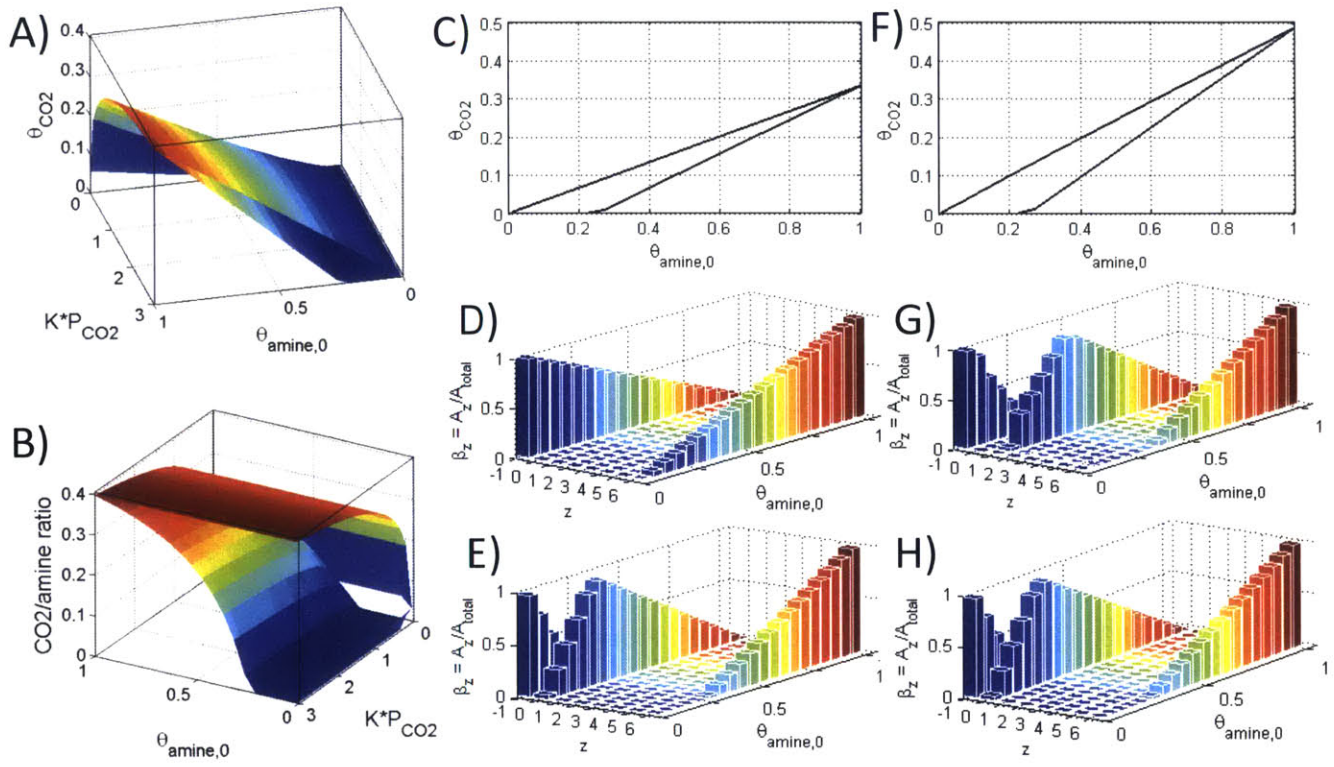

Figure 52. (A) and (B) show the maximum and minimum θ_{CO2} and CO_2/amine ratios, respectively, possible at specific values of K^*P_{CO2} and $\theta_{amine,0}$ by varying surface configuration (α_z values) for a triangular lattice. (C) shows the maximum and minimum values of θ_{CO2} at K^*P_{CO2} = 1 as a function of $\theta_{amine,0}$. (D) and (E) show the makeup of the corresponding surfaces in terms of constant-z surfaces for the maximum and minimum values, respectively. The z = -1 values refer to empty space. (F), (G) and (H) give the same information as (C), (D) and (E), except that K^*P_{CO2} = 100.

We used our developed isotherm in Eq. (47) to fit several experimental data sets from the literature to extract meaningful parameters. Information on the data sets that were used is given in Table 12. Although several data sets were considered, only those that used mono-amine groups, had known amine loadings, included multiple data points in low pressure regions (< 1 bar), adsorbed under anhydrous conditions, and provided grafted sorbent surface areas were used. At higher pressures, physisorption can be accounted for by subtracting the adsorption isotherm of the ungrafted substrate (an estimate of the physisorption contribution) from the adsorption isotherm of the grafted substrate, as performed in the analysis by Serna-Guerrero et al.[110]

Usually, CO_2 uptake and amine loading is reported in mol/g-sorbent or in some other quantity that is based on measurable values rather than as a surface fraction. Because this model is based on a discrete lattice, these quantities must be converted into surface fractions, which require an effective molecular radius or area of the amine and the total area of the surface. Ideally, only amine groups that are within two radii of each other (up to z_{max} groups) will react with a constant K, and everything beyond two radii will never react (K = 0). The molecular area for 3-aminopropylsilane (APS) was taken to be 0.30 nm^2,[112] and the molecular area for pyrrolidinepropylsilane (PyrPS) was taken to be roughly 1.5 times that of APS, or 0.45 nm^2. It was also assumed that the total area of the surface is given by the surface area of the grafted material as opposed to the surface area of the initial porous material.

For case 1,the data was only fitted to an early part (<0.25 bar) of the adsorption isotherm. The model was not able to fit the data well if points at higher pressures were included. However, the entire adsorption isotherm could be reasonably fitted for cases 2 and 3 up to 1 bar. For each data set, K and $[\alpha_z, z = 0,1,\ldots,z_{max}-1]$ were fitted using χ^2-minimization. Calculated parameters for each data set are given in Table 13 along with the molecular structures of the grafted amine groups; the meaning of these parameters will be discussed later. The 95% confidence intervals for the fitted K-values were determined using bootstrap methods with 500 resamples.[129] The $[\alpha_z]$ values, which are the fractions of amines in each constant-z surface, can be converted using Eq. (45) to give the $[\beta_z]$ values. These values are represented in the form of a histogram, as shown in Figure 54. The z = -1 bin represents the fraction of surface that is just empty space. The error bars indicate 95% confidence intervals, using the same method indicated previously.

Table 12. Characteristics of experimental data fitted to the model

Case[Ref.]	Surface Area of Porous Material (m^2/g)	Surface Area Grafted Material (m^2/g)	Mean Pore Diameter (A) of porous material	Mean Pore Diameter (A) of grafted material	Type of Material	Amine Group	Amine Group Content (mmol/g)	Temp-erature (K)
1[115]	672	409	4.2	4.1	Silica	APS*	1.6	303
2[130]	1290	505	25.8	-	MCM-48	APS*	2.45	298
3[130]	1290	507	25.8	-	MCM-48	PyrPS†	1.48	298

* = 3-aminopropylsilane
† = pyrrolidinepropylsilane

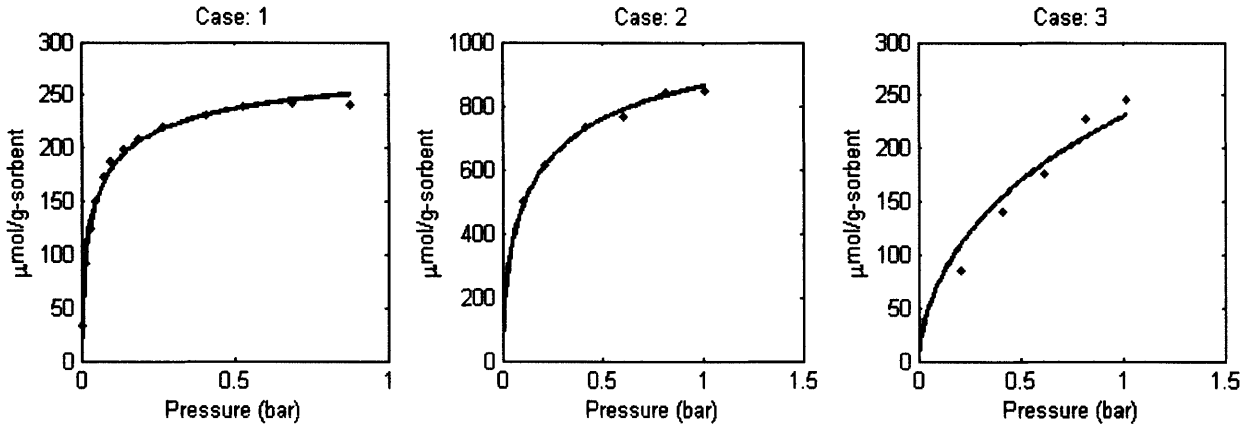

Figure 53. Experimental CO_2 uptakes (•) fitted to current model (—). Adsorbent characterization data for each case are given in Table 12.

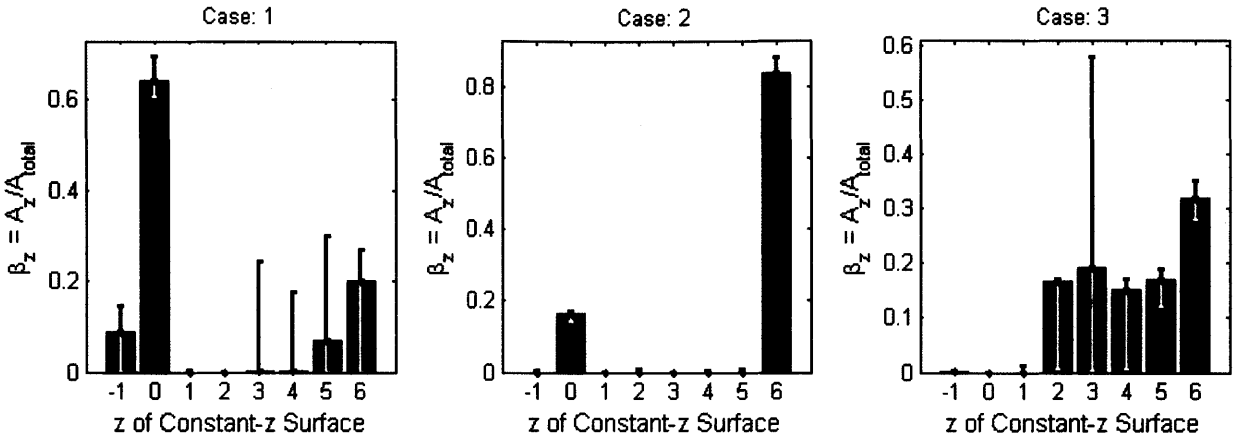

Figure 54. Histograms showing fraction of total surface made up of constant-z surfaces and empty space (z = -1) found after fitting the experimental data. Error bars indicate 95% confidence intervals.

Table 13. Calculated quantities from each data set case and amine group molecular structures.

Case	θ	Best-Fit K	95% CI for K (LB, UB)*	(C:N)/0.5	η = (C:N)/(C:N)	Amine Group
1	0.42	7.1	(4.9, 10.9)	0.39	0.61	
2	0.88	1.7	(1.4, 1.8)	0.42	0.95	
3	0.79	0.11	(0.09, 0.12)	0.11	0.85	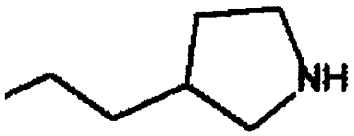

*** = 95% confidence intervals (lower bound, upper bound) calculated using bootstrap methods, 500 resamples**

9.1.5 Discussion

Interpreting Fitted Experimental Data

The discrepancy in the range that the model can fit could possibly be attributed to the added role that physisorption plays in the first case, as the pore sizes are significantly smaller (~4 A) than those of the latter two cases (~25 A). The study containing the first case also tested an adsorbent on

titania substrate,and titania itself was found to have strong interactions with CO_2, so this case was omitted from the fitting.

From the plots in Figure 54, one can see the presence of large error bars. This is partly due to the fact that the adsorption curves of the constant-z surfaces resemble each other in shape, so a z = 4 surface is close to a linear combination of other constant-z surfaces, for example. It should be noted when interpreting the fitted data that the resulting z-histogram only represents one possible effective surface that, under the assumptions of the model, would generate the same adsorption isotherm. There are a multitude of surface configurations that also give close to the same adsorption isotherm, and they represent local minima in the fitting process.

From Table 13, one can observe the variation in fitted K-values for each case. Despite the large error bars for the composition of the effective surface, the corresponding K-value range is relatively narrow, which makes it a useful first approximation to the actual equilibrium constant that accounts for the requirement of adjacent amine groups. The value of this model is that the K-values obtained have a clear physical meaning that, if all the model's assumptions are correct, is equal to the equilibrium constant described by Eq. (39). Although not carried out in this work, these values can be directly compared to theoretical calculations.

As one might expect, the K-values are not exactly the same, but they are within two orders of magnitude of each other. The main cause of variation from this limited set of data appears to be amine type, as the secondary amine PyrPS K-value is roughly one or two orders of magnitude below that of the primary amines. This may be due to lower flexibility and increased steric hindrance of the PyrPS, which decreases the strength of attractive interactions in the product pair. Similar conclusions by Zelenak et al. were obtained from experiment showing a primary amine (3-aminopropylsilane) to have slightly higher amine efficiencies than a secondary amine (3-(methylamino)propylsilane).[131]

The differences in K-value between cases 1 and 2 could be due to differences in pore size or other substrate characteristics. Smaller pore sizes would increase the interaction energy between CO_2 and the substrate, thus increasing the apparent K-value.

Recommendations for Adsorbents

As mentioned previously, the amine type may significantly affect the equilibrium constant. Given the limited data set, primary amines appear to have higher equilibrium constants than secondary or bulky amines. Besides issues of flexibility and steric hindrance, another factor in determining the effective equilibrium constant is the rotational energy barrier of the amine. If this energy is low, like for APS, then it can react with nearest neighbors in any direction with equal probability. On the other hand, high rotational barriers means that given its current orientation, it can only react to a significant extent with z nearest neighbors, where z is less than z_{max}. By lowering the effective z_{max}, even a completely covered surface will appear as a z = 2 surface in terms of adsorption characteristics (see Figure 51), for example. This reasoning recommends less bulky and more rotationally free amines, since these characteristics increase the number of apparent amine pairs available to adsorb CO_2.

Another important factor is the silanol group density on the surface, since this density puts a limit on the maximum amine density possible and can affect the equilibrium constant. For example, although the substrate materials for cases 1 and 2 were silica-based, the densities of silanol groups on which the amines are grafted onto can vary anywhere from 0.7 – 6 silanol groups/nm^2 depending on the preparation method.[132] For lower densities of silanol groups, the K-value might be expected to decrease because the nearest neighbors will be farther apart on average, which could make it more difficult for the amine groups to react with each other, as it requires more alkyl chain flexibility. Most experimental work on CO_2 adsorbents do not individually characterize the silanol densities, so it is difficult to make comparisons, but from this model's assumptions, a higher silanol density on the substrate would be expected to increase both the amine loading limit and the apparent K-value.

In addition, the use of longer amine groups may allow more separated amine groups to react more favorably due to decreased bending strain. This could effectively make a formerly z = 0 surface into a z = 6 surface by increasing the area of reactivity, although the effect is diminished once larger surface densities are used. Another possibility that has already been tried is the use of polyamines to increase the amine loading beyond the silanol group content.[112, 133-134]

Applying the Model to Constrained Surface Configurations

An interesting application of this model, besides fitting data, is in screening potential adsorbents based on surface configurations that are constrained to follow certain rules. In other words, if one can model how amines will arrange in space, the model can offer a first estimate of the adsorbent efficiency. For instance, amine polymers, especially polyethylinimine (PEI), are used ubiquitously in the literature for CO_2 adsorption, as summarized by Choi et al.[102] In this example, a general amine polymer was analyzed for two cases: 1) all parts of the polymer are grafted to the surface and 2) a polymer that is physically impregnated into the porous structure[135] or a polymer produced from direct polymerization on the surface[136]. The first case can be modeled as a polymer in two dimensions, and the second as a polymer in three dimensions. Self-avoiding random walk simulations on a lattice[137] (a triangular lattice for the 2-D simulation and a simple cubic lattice for the 3-D simulation) were performed in both cases using 1000 repetitions to approximate the average z-histogram for the polymers as a function of number of monomers and fraction of tertiary amines, as shown in Figure 55. The amine efficiency was calculated from the average z-histogram, and from typical values of $K = 1$ bar^{-1} and $P_{CO2} = 0.12$ bar, using Eq. (47), where the CO_2:N ratio = $\theta_{CO2}/\theta_{amine,0}$; under these conditions, the maximum CO_2:N ratio is 0.18. It was assumed that each monomer in the simulation contained one amine, and the next monomer attached onto the amine of the previous monomer, as in polyethylenimine (PEI).[102] Thus, a linear monomer consists of all secondary amines, except for the unreacted end, and a branched polymer contains the ratio n+1:m:n of primary:secondary:tertiary amines, assuming no cross-linking occurs.

From Figure 55, one can see that as the fraction of tertiary amines increases (branching increases), the amine efficiency decreases. Despite more amines being closer together as branching increases, a larger proportion of amines are tertiary, and thus, less reactive. Tertiary amines can only accept a hydrogen from an adjacent, primary or secondary amine group; they cannot become the carbamate group. Therefore, while tertiary amines can be effective partners with primary and secondary amines for CO_2 uptake, adjacent tertiary amines are not effective for reacting with CO_2. This concept is illustrated in Figure 56. Therefore, linear polymers (zero fraction of tertiary amines) would seem to have the best amine efficiency under this simple model. In addition, polymers constrained on a plane appear to have higher efficiencies compared to the corresponding 3-D polymer with the same size and fraction of tertiary amines.

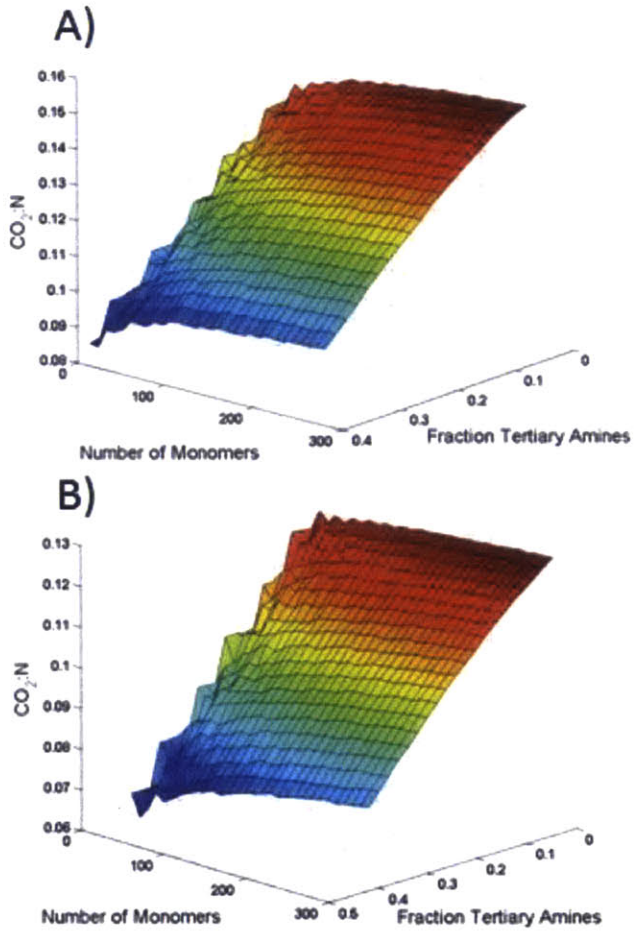

Figure 55. Amine efficiency of a 2D (A) and 3D (B) self-avoiding random-walk polymer as a function of the number of monomers and the fraction of tertiary amines.

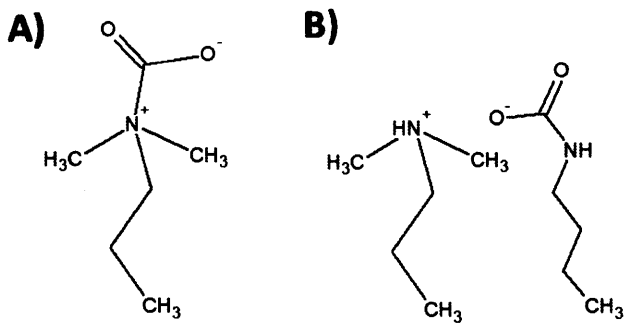

Figure 56. (A) shows the result of a tertiary amine reacting with CO_2, which is assumed to be unlikely under anhydrous conditions, and (B) shows how a tertiary amine can be the proton acceptor when paired with a primary or secondary amine.

It is of interest to see if experimental data supports this conclusion that more branching leads to lower amine efficiencies, and vice versa. Table 14 separates several adsorbent studies based on whether highly branched polymers (PEI) or linear amine molecules (DEA and TEPA) were used, using amine efficiencies (CO_2:N ratios) of amine-impregnated silica adsorbents compiled by Choi et al.[102]. For physical impregnation, these molecules can be thought of as 3D random walk polymers to a first approximation. Although different supports were used, the temperatures and pressures were the same for all studies. One sees that amine efficiencies for linear amine molecules (which contain only primary and secondary amines) are roughly 50% higher than highly-branched PEI molecules. Although these efficiencies are not directly comparable to those of Figure 55B, since those simulations were performed for K = 1 bar^{-1} and P_{CO2} = 0.12 bar, it illustrates a probable reason behind large decreases in amine efficiency when moving to highly branched amine polymers.

Table 14. Summary of amine efficiencies for amine-impregnated silicas (adapted from Choi et al.[102])

Amine*[Ref.]	**Support**	**T (K)**	**P_{CO2} (bar)**	**(CO_2:N)**
PEI[138]	proprietary inorganic support	348	1	0.26
PEI[135]	MCM-41	348	1	0.17
PEI[139]	KIT-6	348	1	0.26
PEI[140]	MCM-41	348	1	0.17
			Average (CO_2:N)	**0.215**
TEPA[141]	SBA-15	348	1	0.3

DEA/TEPA[142]	SBA-15	348	1	0.37
			Average (CO_2:N)	**0.335**

PEI = polyethylenimine, TEPA = tetraethylenepentamine, DEA = diethanolamine

Another route toward densely packed amine structures may be to wrap amine polymers around a nanostructured scaffold such as carbon nanotubes (CNTs) in a cylindrical helix shape. This model gives qualitative recommendations for the pitch of the helix and quantitative predictions of the expected amine efficiency for wrapped CNTs. As the pitch (width between consecutive loops) becomes large, such that amines on adjacent loops cannot react, the surface looks like a z = 2 surface, which has an amine efficiency of 0.12 at K = 1 bar^{-1} and P_{CO2} = 0.12 bar. However, once the pitch decreases such that adjacent loops can react with each other, the apparent number of nearest neighbors increases significantly, making the structure react as a z = 6 surface, which has an amine efficiency of 0.18, a 50% increase, under the same conditions. In addition, the overall CO_2 uptake per nanotube (same area) for a tightly wrapped polymer over a loosely wrapped polymer would be roughly 3 times greater or more, depending on how loosely wrapped (in terms of pitch distance) the polymer is. From these examples, we demonstrate how this model could allow a more rational approach toward adsorbent synthesis.

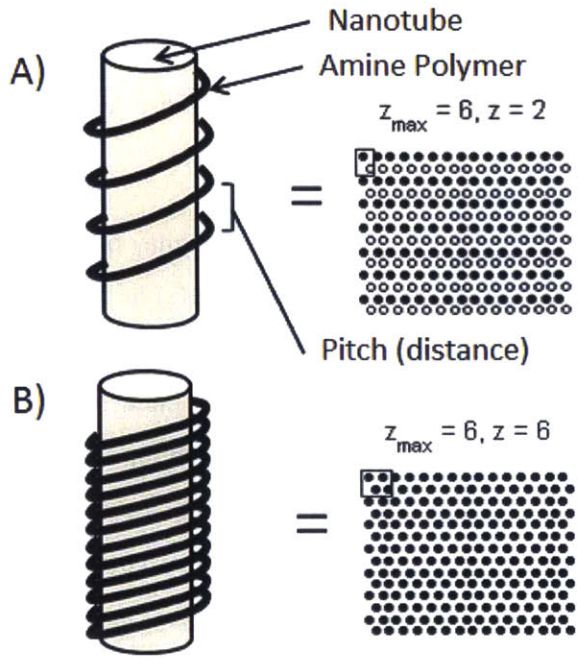

Figure 57. Schematic of amine-wrapped nanotubes and their corresponding constant-z surfaces for (A) high-pitch and (B) low-pitch cases.

A New Measure of Amine Efficiency

In using this model in experimental work, it is suggested that a new quantity be reported concerning amine efficiency:

$$(57)\ \eta = \frac{\left(CO_2 : N\right)_{actual}}{\left(CO_2 : N\right)_{ideal}} = \frac{\theta_{CO_2,actual}}{\theta_{CO_2,ideal}}$$

where

$$(58)\ \left(CO_2 : N\right)_{ideal} = \max\left[\sum_{z=0}^{z_{max}} h_z\left(K \cdot P_{CO_2}\right) \cdot \frac{\alpha_z}{\theta_z}\right]$$

This factor η provides a measure of amine efficiency that compares the experimental CO_2 uptake with the maximum ideal uptake at the same P_{CO2} and K as the experiment when the optimal surface configuration of amines is used. The value of K is determined either from fitting adsorption data to the model or using a previously calculated value. The reason for this quantity is that most

researchers report $(CO_2:N)_{actual}$ and explicitly or implicitly compare it with the ideal stoichiometric value of 0.5, as if the reaction were irreversible. This new measure of amine efficiency gives a more realistic estimate of how efficiently amines are being used, because it compares the actual value to the maximum attainable value at the same pressure, under this model's assumptions, taking into account the unique chemistry occurring at the surface. Therefore, the quantity is pressure-independent and more easily comparable. It is possible that η could be greater than 1 due to limitations of the model, and this would give the extent of other contributions to CO_2 uptake. The values of η were calculated for the data sets fitted, as shown in Table 14 at an industrially relevant low CO_2 pressure of 12 kPa.[143] One can see that if $(CO_2:N)_{actual}$ were compared to 0.5, the efficiencies look rather low. However, in terms of what could possibly be attained, given the amine type (a certain K-value) and amine loading ($\theta_{amine,0}$), the adsorbents are fairly close to the optimal value, in terms of surface configuration.

9.1.6 Conclusions

In this study, a new isotherm equation was proposed which describes the adsorption of dimers onto a surface, where the active groups on which dimers can be adsorbed onto can be of an arbitrary configuration. This model was applied to CO_2 adsorbents, where a CO_2 molecule adsorbs onto two adjacent amine groups, and amine groups are covalently grafted onto the surface of the porous substrate. By functionalizing the results of a small number of Monte Carlo simulations, an adsorption isotherm equation was proposed which can accurately predict the adsorption characteristics of an arbitrary surface given the surface's z-histogram (which can be computed or estimated fairly easily), the initial surface fraction of amine groups, and the equilibrium constant of the reaction of CO_2 with two adjacent amine groups.

This model was then used to fit experimental data in the literature at low pressures, where only chemisorption would be expected to be significant. The resulting fitted parameters gave the equilibrium constant that corresponds to the actual reaction occurring at the molecular level as well as parameters that can be used to visualize the effective surface configuration of amines on the surface. In addition, the model was used to predict the range of uptake values that can be obtained through varying the surface configuration. Under the most relevant values of pressure and

equilibrium constant, a fully filled surface is expected to give the highest CO_2 capacity. The model was further applied to amine polymers and nanostructured materials to give recommendations for more efficient materials. A new quantity to describe amine efficiency was introduced which gives the CO_2 uptake normalized by that expected given an ideal surface configuration. It is hoped that this study will provide a fundamental model of CO_2 adsorption that highlights the role that surface configuration plays and points toward ways of exploiting this unique chemistry.

9.2 The Structubent: A Nanocomposite Solution for Compressed Natural Gas Storage

9.2.1 Introduction

Natural gas is expected to be the fastest-growing energy source over the next three decades, with consumption predicted to increase 64% from 2010 to 2040.[144] Natural gas has also been cited as a possible bridge fuel from coal and oil to cleaner, renewable forms of energy.[145] However, natural gas, unlike oil, presents more difficulties in storage and transportation due to its gaseous state. Depending on the economic situation, natural gas recovered at a well may be 1) flared, or burned at the site of the well, if there are no economically accessible markets or for safety reasons,[146] 2) taken by pipeline across land to an end-user,[147] 3) up-converted to liquid fuels in a gas-to-liquid (GTL) process,[148] 4) cooled to liquefied natural gas (LNG) for long-distance transport, usually overseas,[149] or 5) pressurized to form compressed natural gas (CNG) for transport.[150]

Overseas bulk transport of natural gas has typically relied on liquefaction of the gas to achieve higher energy density. But LNG has several disadvantages, including the high, initial energy requirement for cooling to cryogenic temperatures (-162 C), the persistent boil-off gas needed to keep the LNG cold making long-term storage not possible, and the high costs for LNG plants and cryogenic storage tanks. The reason LNG continues to dominate compared to CNG is the fact that the higher energy density, approximately 2.5 times that of CNG compressed to 200 bar (assuming pure methane), overcomes these economic hurdles.

Alternatives to LNG include CNG and adsorbent natural gas (ANG), where natural gas is stored in an adsorbent bed. CNG is the more mature technology, and smaller tanks are used for vehicular fuel storage mainly in trucks and light-duty vehicles under a working pressure of 200 or 250 bar. There are currently four different types of CNG tanks (I through IV), with type 1 being the heaviest and most inexpensive, being constructed entirely out of steel or aluminum, and type 4 being the lightest and most expensive, consisting of a composite wrap with an inner, gas-tight plastic liner.[151] Meanwhile, there has been several research studies looking into natural gas storage using

adsorbents which could potentially achieve similar storage capacities at lower working pressures (35 bar is the standard, which allows for single-stage compression), thus decreasing refueling costs and improving safety.[152]

The novel concept we are proposing is a combined adsorbent-compressed natural gas system, wherein the adsorbent not only adsorbs natural gas, but contributes to the structural integrity of the vessel itself; thus we refer to it as a structubent. The structubent material can be a pure adsorbent material embedded in a structural material, where the structural material would be a porous polymeric matrix in order to allow methane diffusion into the adsorbent, as shown in Figure 58.

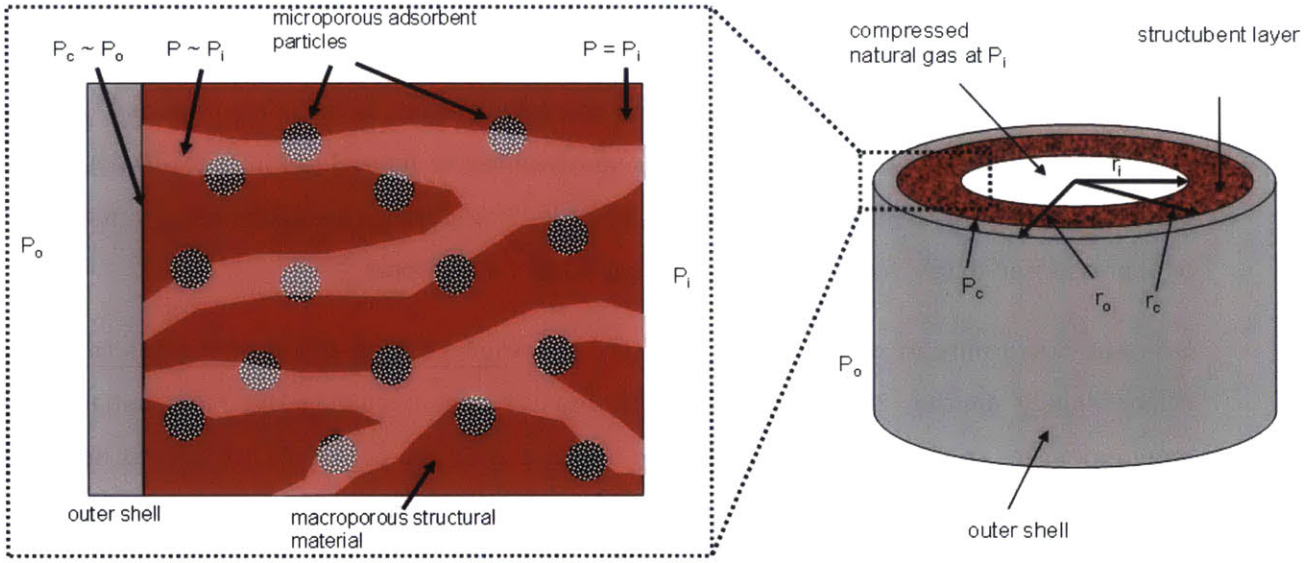

Figure 58. Schematic of proposed structubent concept for compressed natural gas storage. Microporous methane adsorbent particles can be embedded inside an annulus of structural matrix with some volume fraction, ε. It is assumed here that the structural material is macroporous, thus ensuring that adsorption takes place at the internal pressure, P_i. However, the radial thickness of the structural matrix is such that the contact pressure, P_c between the shell material and structubent layer is essentially the outer, atmospheric pressure, P_o.

9.2.2 Results and Discussion

To begin, we seek to optimize two figures of merit for compressed natural gas storage tanks: 1) the volume specific capacity (moles of methane stored per total vessel volume per unit length of

cylinder) and 2) the mass specific capacity (moles of methane stored per empty vessel mass per unit length of cylinder). There are several design parameters and material properties that can vary in the following analysis of structubent-based CNG vessels, as indicated in Table 15. To reduce the number of degrees of freedom in the problem, certain parameters will be fixed depending on the feasibility of actually varying them in the real world. This analysis assumes the existence of composite reinforcing particles that can simultaneously act as high surface area adsorbents for gases permeating the otherwise permeable composite matrix.

Table 15. List of design parameters and material properties for structubent-based CNG vessels.

Parameters	Symbol	Units
Vessel outer radius	r_o	[m]
Vessel inner radius	r_i	[m]
Outer shell density	ρ_{outer}	[m]
Outer shell ultimate tensile strength (UTS)	UTS_{outer}	[MPa]
Outer shell modulus	E_{outer}	[MPa]
Matrix thickness	t_{matrix}	[m]
Matrix density	ρ_{matrix}	[kg/m^3]
Matrix UTS	UTS_{matrix}	[MPa]
Matrix modulus	E_{matrix}	[MPa]
Maximum methane adsorption capacity	w_{max}	[mg-methane/g-adsorbent]
Langmuir constant for adsorption isotherm	K	[1/MPa]
Adsorbent UTS	UTS_{ads}	[MPa]
Adsorbent density	ρ_{ads}	[kg/m^3]
Volume fraction of adsorbent particles inside structural matrix	ϵ	--
Internal working pressure	P_i	[MPa]
Maximum stress ratio for vessel	A	--

Mechanical Constraint

We can first determine the feasibility of the structubent concept by finding the parameters of a structubent layer such that using the structubent design would increase the specific capacities over the baseline case of just using another structural material for support. We will assume that there is

only a single layer comprising the vessel, and that layer is of a thickness to just satisfy the safety criteria.

Although there are several standards that dictate slightly different safety criteria for pressure vessels, usually the safety factor is defined as the minimum burst ratio, $\alpha = \frac{P_{burst}}{P_i}$, which is just the ratio of burst pressure, P_{burst}, to the actual internal working pressure, P_i. This safety factor can also vary by the type of material, but a typical value we will use in the following analysis is 3.0.[151] Burst pressures can be determined experimentally or by finite element analysis, and there have been numerous relationships developed that attempt to predict the burst pressure, P_{burst}. Of these relationships, the simplest is the Barlow equation shown in Eq. (59) which provides reasonable accuracy.[153] Here, σ_{UTS} is the ultimate tensile strength of the material, r_o is the outer radius, and r_i is the inner radius. After combining this equation with the minimum burst ratio, we can obtain the maximum inner radius (or minimum thickness) of the walls to satisfy this safety factor (Eq. (60)).

$$(59)\ P_{burst} = \frac{\sigma_{UTS}\left(r_o - r_i\right)}{r_i}$$

$$(60)\ r_{i,\max} = \frac{r_o \sigma_{UTS}}{\alpha\left(P_i - P_o\right) + \sigma_{UTS}}$$

Volume Specific Capacity

With this constraint on the inner radius, we can express the volume specific capacity per unit length of the cylinder, $C_{vol,base}$, of the baseline case where there is no structubent (e.g. the pressure vessel is just a steel shell), as shown in Eq. (61). The amount of methane stored is given by the inner volume of the vessel (πr_i^2) divided by the molar volume of methane at the working temperature and pressure, $v_{EOS}(T,P_i)$. The molar volume of compressed methane, assuming the stored natural gas is 100% methane, was obtained using the Peng-Robinson equation.[154]

The volume specific capacity for the structubent case can be expressed assuming that the structubent material experiences the internal methane pressure all throughout the layer.

Furthermore, we assume the structubent follows a Langmuir adsorption isotherm, where the number of moles adsorbed per unit volume is expressed as: $n_{ads} = \frac{n_{\max} K P_i}{1 + K P_i}$. The Langmuir isotherm fits the adsorption data very well for a variety of adsorbents.[155-156] It should be noted that the value of $r_{i,max}$ is different between the base case and structubent case, as $\sigma_{UTS,base}$ is not necessarily equal to $\sigma_{UTS,struct}$.

$$(61)\ C_{vol,base} = \frac{N_{void}}{V} = \frac{\pi \cdot r_{i,\max}^2 / v_{EOS}(T, P_i)}{\pi \cdot r_o^2}$$

$$(62)\ C_{vol,struct} = \frac{N_{void} + V_{struct} \cdot n_{struct}}{V} = \frac{\pi \cdot r_{i,\max}^2 / v_{EOS}(T, P_i) + \pi \cdot \left(r_o^2 - r_{i,\max}^2\right) \frac{n_{\max,struct} K P_i}{1 + K P_i}}{\pi \cdot r_o^2}$$

The ratio of these volumetric capacities, after simplification and substitution of the relation for $r_{i,max}$, is given by Eq. (63).

(63)

$$\beta_{vol} = \frac{C_{vol,struct}}{C_{vol,base}} = \frac{\left(\sigma_{UTS,base} + \alpha P_{\text{int}} - \alpha P_o\right)^2 \left(\alpha \left(P_{\text{int}} - P_o\right) \left(\frac{n_{\max,struct} K P_{\text{int}}}{1 + K P_{\text{int}}} v_{EOS}(T, P_{\text{int}}) \right) \left(\alpha P_{\text{int}} - \alpha P_o + 2\sigma_{UTS,struct}\right) + \sigma_{UTS,struct}^2 \right)}{\sigma_{UTS,base}^2 \left(\alpha P_{\text{int}} - \alpha P_o + \sigma_{UTS,struct}\right)^2}$$

$$= \frac{\left(\sigma_{UTS,base} + \alpha P_{\text{int}} - \alpha P_o\right)^2 \left(\alpha \left(P_{\text{int}} - P_o\right) \lambda(T, P_{\text{int}}) \left(\alpha P_{\text{int}} - \alpha P_o + 2\sigma_{UTS,struct}\right) + \sigma_{UTS,struct}^2\right)}{\sigma_{UTS,base}^2 \left(\alpha P_{\text{int}} - \alpha P_o + \sigma_{UTS,struct}\right)^2}$$

When $\beta_{vol} > 1$, then it makes sense to employ the structubent design from a performance perspective optimizing volume specific capacity. One notices the presence of the term, $\lambda(T,P_{int})$, which is the ratio of the molar densities of methane adsorbed in the structubent and compressed methane at a specific pressure, $\lambda(T,P_{int}) = n_{struct}/n_{void} = \left(\frac{n_{\max,struct} K P_{\text{int}}}{1 + K P_{\text{int}}} v_{EOS}(T, P_{\text{int}}) \right)$. Because volume specific capacities do not depend on density, the capacity ratio is not a function of the densities in any way. We can plot β_{vol} as a function of the ultimate tensile strength of the structubent layer,

$\sigma_{UTS,struct}$, and the ratio of molar densities, $\lambda = n_{ads}/n_{void}$, as shown in Figure 59. In this figure we look at two internal pressures: 3.5 MPa (35 bar) and 20 MPa (200 bar). The lower pressure has been used as the testing pressure for adsorbent natural gas storage studies, as this is roughly the pressure achievable by single-stage compression, and adsorbents reach saturation at lower pressures.

There are a few important observations. The first is that, as expected, the β_{vol} ratio increases as λ increases, and the cross-over point at which it is favorable to have a structubent design is around $n_{ads}/n_{void} \sim 1$. The reason for this is that when the structubent layer reaches the same molar density as that of compressed natural gas, β_{vol} reduces to $r_o^2/r_{i,max,base}^2 \sim 1$; essentially, one is adding a small amount of volume, equal to the volume of the base shell, to store methane upon switching to the structubent design. The second observation which may be counter-intuitive, is that increasing the strength of the structubent layer actually decreases the capacity of the structubent vessel versus the baseline case when $n_{ads}/n_{void} > \sim 1$ (or more accurately, $r_o^2/r_{i,max,base}^2$). The reason for this result is that as you increase the structubent layer strength, you need less of it to satisfy the mechanical constraint. And because the structubent layer actually has a greater molar density than compressed methane, you actually decrease the relative advantage of the structubent design as you use less structubent material. If one were optimizing for the highest volume specific capacity, then it would actually make sense to either use no structubent at all (if $n_{ads}/n_{void} < \sim 1$) and have the vessel constructed entirely of structubent if $n_{ads}/n_{void} > \sim 1$ if one were purely optimizing volume specific capacities.

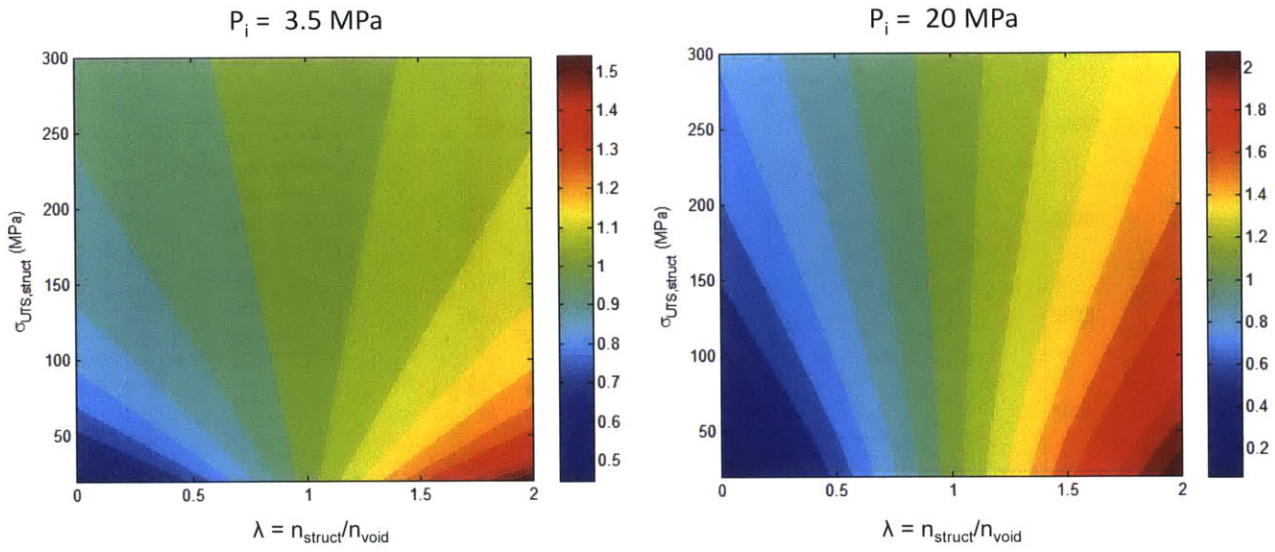

Figure 59. Ratio of volume specific capacities, β_{vol}, as a function of the structubent layer ultimate tensile strength, $\sigma_{UTS,struct}$, and the ratio of molar densities at the specified pressure, n_{struct}/n_{void}. Other conditions used are P_{int} = 20 MPa, P_o = 0.1 MPa, and α = 3.0.

At minimum, to have an increase in volume specific capacity, there must exist adsorbents that have higher molar densities than that of compressed methane, since incorporating adsorbents into a structural matrix will only decrease their adsorption molar density. Figure 60 shows data from some carbon-based and zeolite methane adsorbents compared with compressed natural gas at the same pressures. Adsorbents generally do better at lower pressures but reach saturation quickly, which is why most adsorbent-based natural gas storage studies are carried out at lower pressures (usually 3.5 MPa) with the economic benefit that this pressure is achievable by single-stage compressors.

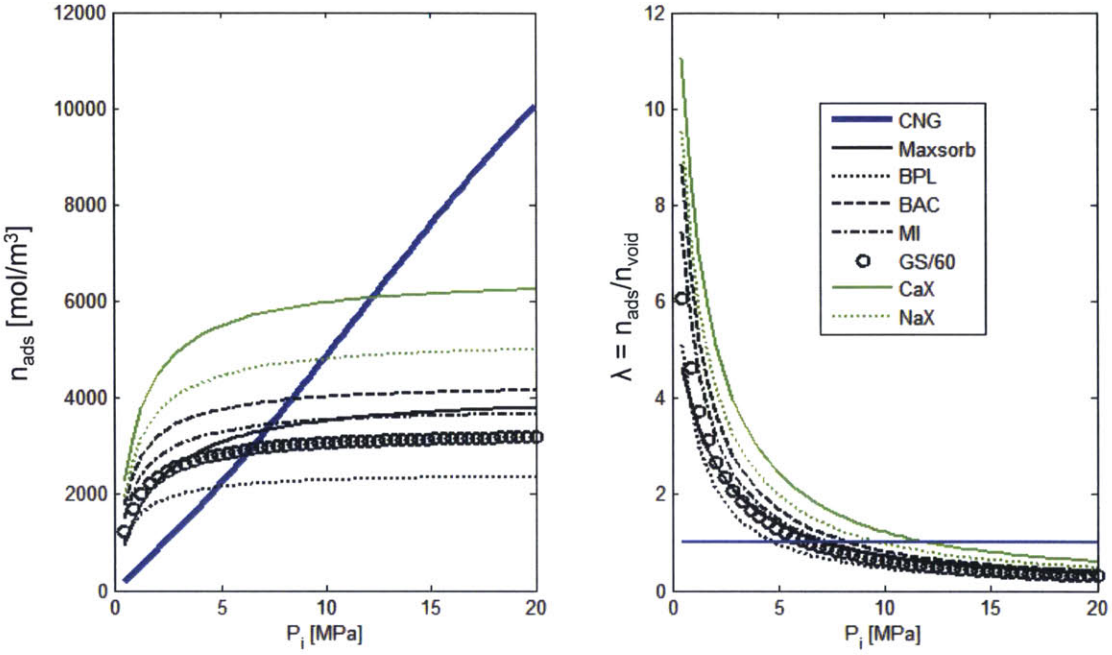

Figure 60. Plots of n_{ads} and n_{ads}/n_{void} as a function of P_i. For reference, liquid methane at atmospheric pressure has a molar density of around 26,000 mol/m^3.

Mass Specific Capacity

The volume specific capacity optimization is somewhat trivial, as it requires an adsorbent or structubent layer with a molar density much higher than that of compressed natural gas. Another important figure of merit to consider is the mass specific capacity per unit length of the cylinder, C_{mass}, which is the moles of methane stored divided by the mass of the empty vessel. For the baseline case of an inert shell material, the amount of methane stored is given by the inner volume of the vessel divided by the molar volume of methane at the working temperature and pressure, $v_{EOS}(T,P)$. The empty mass is given by the volume of the shell multiplied by the density of the shell material, ρ_{base}.

$$(64)\ C_{mass,base} = \frac{N_{void}}{W_{base}} = \frac{\pi \cdot r_{i,\max}^2 / v_{EOS}\left(T, P_i\right)}{\pi \cdot \left(r_o^2 - r_{i,\max}^2\right) \cdot \rho_{base}}$$

The mass specific capacity for the structubent case is written in Eq. (65).

$$(65)\ C_{mass,struct} = \frac{N_{void} + V_{struct} \cdot n_{struct}}{W_{struct}} = \frac{\pi \cdot r_{i,\max}^2 / v_{EOS}(T,P_i) + \pi \cdot \left(r_o^2 - r_{i,\max}^2\right) \frac{n_{\max,struct} KP_i}{1+KP_i}}{\pi \cdot \left(r_o^2 - r_{i,\max}^2\right) \cdot \rho_{struct}}$$

The ratio of the two mass specific capacities yield can be simplified to Eq. (66). When $\beta_{mass} > 1$, then it makes sense to employ the structubent design from a performance perspective optimizing mass specific capacity.

(66)

$$\beta_{mass} = \frac{C_{mass,struct}}{C_{mass,base}} = \frac{\left(\frac{\rho_{base}}{\rho_{struct}}\right)\left(2\sigma_{UTS,base} + \alpha P_{\text{int}} - \alpha P_o\right)\left(\alpha\left(P_{\text{int}} - P_o\right)\left(\frac{n_{\max,struct} KP_{\text{int}}}{1+KP_{\text{int}}} v_{EOS}(T,P_{\text{int}})\right)\left(2\sigma_{UTS,struct} + \alpha P_{\text{int}} - \alpha P_o\right) + \sigma_{UTS,struct}^2\right)}{\sigma_{UTS,base}^2\left(\alpha P_{\text{int}} - \alpha P_o + 2\sigma_{UTS,struct}\right)}$$

$$= \frac{\gamma\left(2\sigma_{UTS,base} + \alpha P_{\text{int}} - \alpha P_o\right)\left(\alpha\left(P_{\text{int}} - P_o\right)\lambda(T,P_{\text{int}})\left(2\sigma_{UTS,struct} + \alpha P_{\text{int}} - \alpha P_o\right) + \sigma_{UTS,struct}^2\right)}{\sigma_{UTS,base}^2\left(\alpha P_{\text{int}} - \alpha P_o + 2\sigma_{UTS,struct}\right)}$$

Looking at this expression, we see that this ratio depends on two important parameters: 1) the ratio of base and structubent densities, $\gamma = \rho_{base}/\rho_{struct}$, and, as before, 2) the ratio of the molar densities of methane adsorbed in the structubent and compressed methane at a specific pressure, $\lambda(T,P_{int})$ $=n_{struct}/n_{void} = \left(\frac{n_{\max,struct} KP_{\text{int}}}{1+KP_{\text{int}}} v_{EOS}(T,P_{\text{int}})\right)$.

The β_{mass} is plotted in Figure 61 as a function of γ and λ at several different values of $\sigma_{UTS,struct}$. Each combination of γ, λ, and $\sigma_{UTS,struct}$ represent some idealized structubent layer that happens to have this combination of physical and mechanical properties. These plots show that, as expected, increasing λ, γ and $\sigma_{UTS,struct}$ have the effect of increasing β_{mass}. It is interesting to note that as the structubent layer increases in strength, the effect of increasing λ decreases. This effect occurs

because less structubent layer is needed, therefore there is a smaller increase in total moles stored in the vessel as the structubent layer molar density increases.

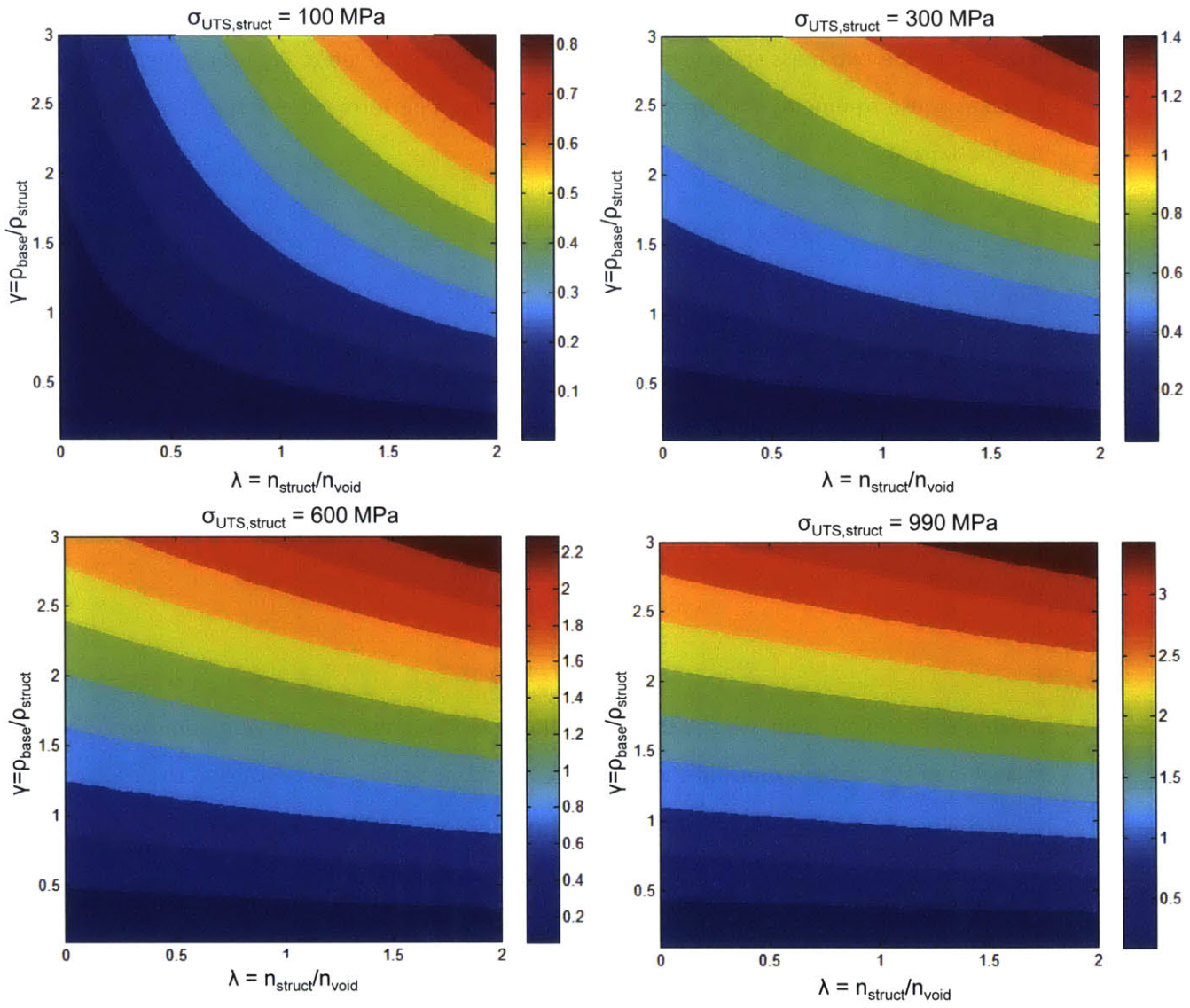

Figure 61. The ratio of mass specific capacities for the structubent and baseline designs, where a value > 1 means the structubent design offers an enhancement over the baseline case, which is a steel vessel ($\sigma_{UTS,base}$ = 990 MPa). This ratio is plotted against the density ratio and molar density ratio for different values of $\sigma_{UTS,struct}$. Other conditions used are P_{int} = 20 MPa, P_o = 0.1 MPa, T = 298K, and α = 3.0.

Thus, we observe that it is possible to obtain significant enhancements over the baseline case of a steel pressure vessel, and the previous plots indicate the conditions, namely γ and λ, that are required to make the structubent concept feasible. The next step is to determine potentially achievable values for γ and λ from real-world materials.

Analysis of Current Adsorbent and Composite Properties

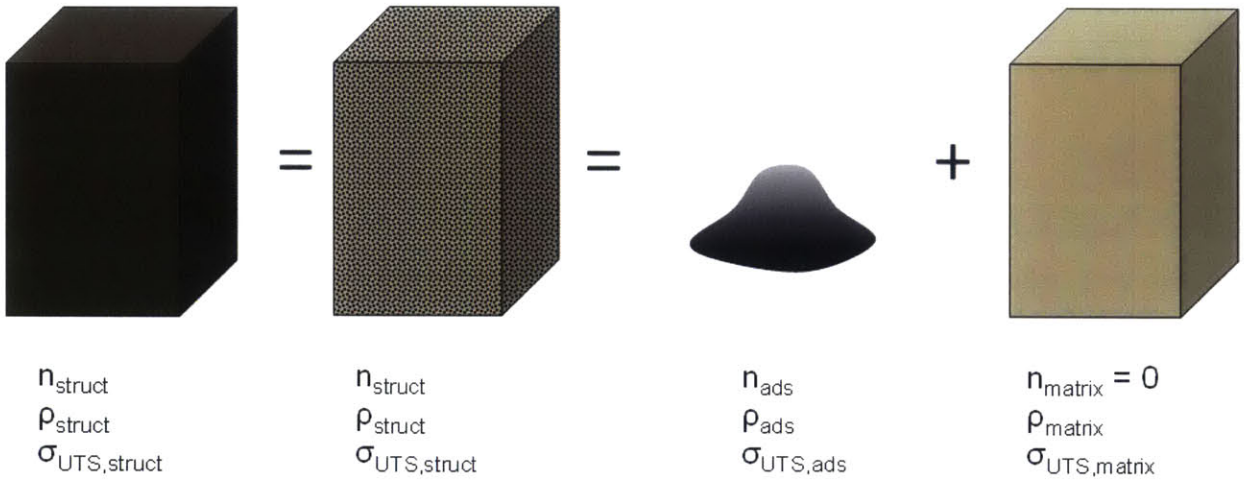

Figure 62.The structubent layer can be abstracted as a homogeneous layer with overall adsorbent and mechanical properties, but the layer itself must be made up of adsorbent particles and a support material, each with their own adsorbent and mechanical properties.

Before, we were considering the structubent layer itself as an adsorbent, but in reality, it would be a composite consisting of a matrix material and an adsorbent material. Thus, we can substitute in the following relationships (Eq. (67)-(69)) into Eq. (66) to get the ratio of mass specific capacities as a function of the volume fraction of adsorbent in the matrix, ϵ for specific potential adsorbents and matrix materials. The matrix and adsorbent material properties used are listed in Table 16 and Table 17.

$$(67)\ \gamma = \frac{\rho_{struct}}{\rho_{base}} = \frac{\varepsilon\rho_{ads} + (1-\varepsilon)\rho_{matrix}}{\rho_{base}}$$

(68) $$\lambda = n_{struct} / n_{void} = \left(\frac{\varepsilon n_{\max,ads} K P_{\text{int}}}{1 + K P_{\text{int}}} \right) v_{EOS}(T, P_{\text{int}})$$

(69) $$\sigma_{UTS,struct} = \varepsilon \sigma_{UTS,ads} + (1-\varepsilon)\sigma_{UTS,matrix}$$

Table 16. Table of matrix materials considered to construct the structubent layer in order of increasing $\sigma_{UTS,matrix}$.

Matrix Index	*Common Name*	*Type*	*Density (g/mL)*	*$\sigma_{UTS,matrix}$ (MPa)*	*E_{matrix} (MPa)*	*References*
1		Epoxy	1.00	4.00	118.00	[157]
2		Polymethylmethacrylate (PMMA)	1.18	24.20	750.00	[158]
3		Polypropylene (PP)	0.91	33.00	1344.00	[159-160]
4	SC-15	Epoxy	1.14	60.00	2500.00	[161]
5	Nylon 6/6	Polyamide	1.14	85.50	2826.90	
6		Polyimide	1.40	100.00	2500.00	[162]

Table 17. Table of adsorbent materials considered to construct the structubent layer in order of decreasing w_{max}.

Adsorbent Index	*Common Name*	*Type*	*Particle Density (g/mL)*	*Fitted Langmuir Constant, K (MPa^{-1})*	*Fitted Maximum Adsorption, w_{max} (mg/g)*	*$\sigma_{UT,matrix}$ (MPa)*	*References*
1	Kansai Maxsorb	Carbon	0.29	0.60	244.98	?	[155]
2	Sutcliffe GS/60	Carbon	0.60	1.18	157.07	?	[155]
3	Barnebey MI	Carbon	0.71	1.32	132.57	?	[155]
4	Kureha BAC	Carbon	0.90	1.44	117.14	?	[155]

5	CaX	Zeolite	1.00	1.05	105.35	?	[156]
6	Calgon BPL	Carbon	0.75	1.48	89.35	?	[155]
7	NaX	Zeolite	1.00	1.19	83.71	?	[156]

Figure 63 and Figure 64 are constructed using Eqs. (66) and (63) to compute β_{mass} and β_{vol} for each combination of adsorbent and matrix material. It is assumed that $\epsilon = 0.4$, which is a relatively high volume fraction of adsorbent particles. Experimental studies of synthesizing composite materials typically only use $\epsilon = 0.01$-0.05, as the goal is to strengthen the composite material with as little particulate as possible, so there are fewer studies looking at high loading of filler materials. There is precedent though, as rubber tires consist of up to 39 wt% carbon black, which increases the mechanical properties.[163] For constructing a structubent, it is ideal to have much higher volume fractions so that the volume specific capacity is not decreased too significantly. However, there are major hurdles in creating composite materials with high filler material fractions, especially since there is increased likelihood of macroscopic aggregation and phase segregation which can diminish overall mechanical properties. The enhancement of mechanical properties depends on the strength of the adsorbent particle-matrix interfacial bonds, which in itself is subject of much research.[164] Another assumption is that the rule of mixtures applies to calculating the composite density and ultimate tensile strengths.

One observes that for some matrix/adsorbent material combinations, there can be significant enhancements up to 40% over the baseline case in terms of the mass specific capacity, especially at lower pressures (Figure 64). Furthermore, at lower pressures, because adsorbent uptake is higher relative to CNG, the volume specific capacity is kept relatively the same compared to the baseline case of a steel cylinder. Another observation is that while λ is relatively low (0.15-0.25), the ratio of densities, γ, is quite high (6-12) indicating that the structubent layer is much lighter than steel, which allows it to achieve good specific capacities despite the structubent layer having lower molar densities relative to standard CNG.

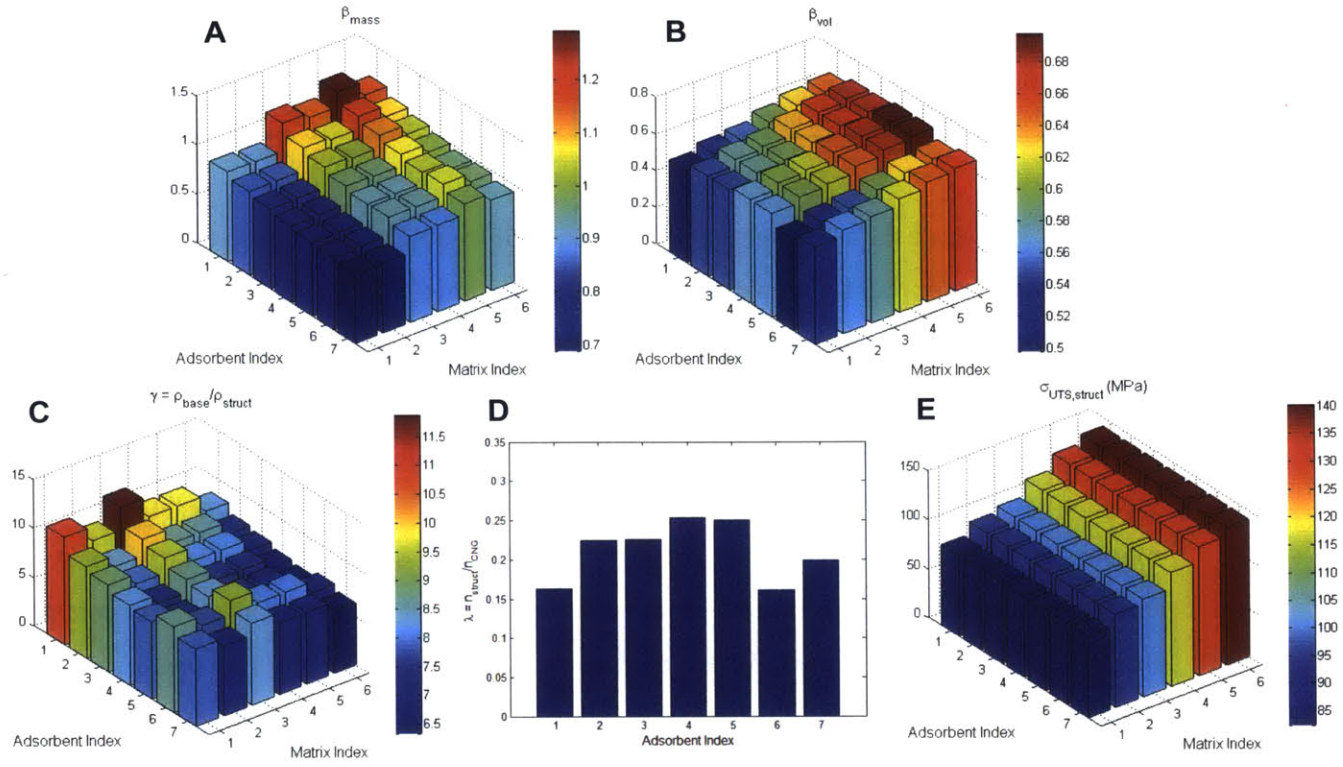

Figure 63. Structubent figures of merit at 20 MPa, ϵ = 0.4, and $\sigma_{UTS,ads}$ = 200 MPa compared to a steel CNG cylidner. (A) Ratio of mass specific methane capacities as a function of combining specific adsorbents and matrix materials together. The indices of materials correspond with those in Table 16 and Table 17. (B) Ratio of volume specific capacities. (C) Ratios of densities of baseline material and composite structubent layer. (D) Ratio of molar densities of composite structubent layer for each adsorbent material. (E) Ultimate tensile strength of the composite structubent layer for each adsorbent/matrix material combination.

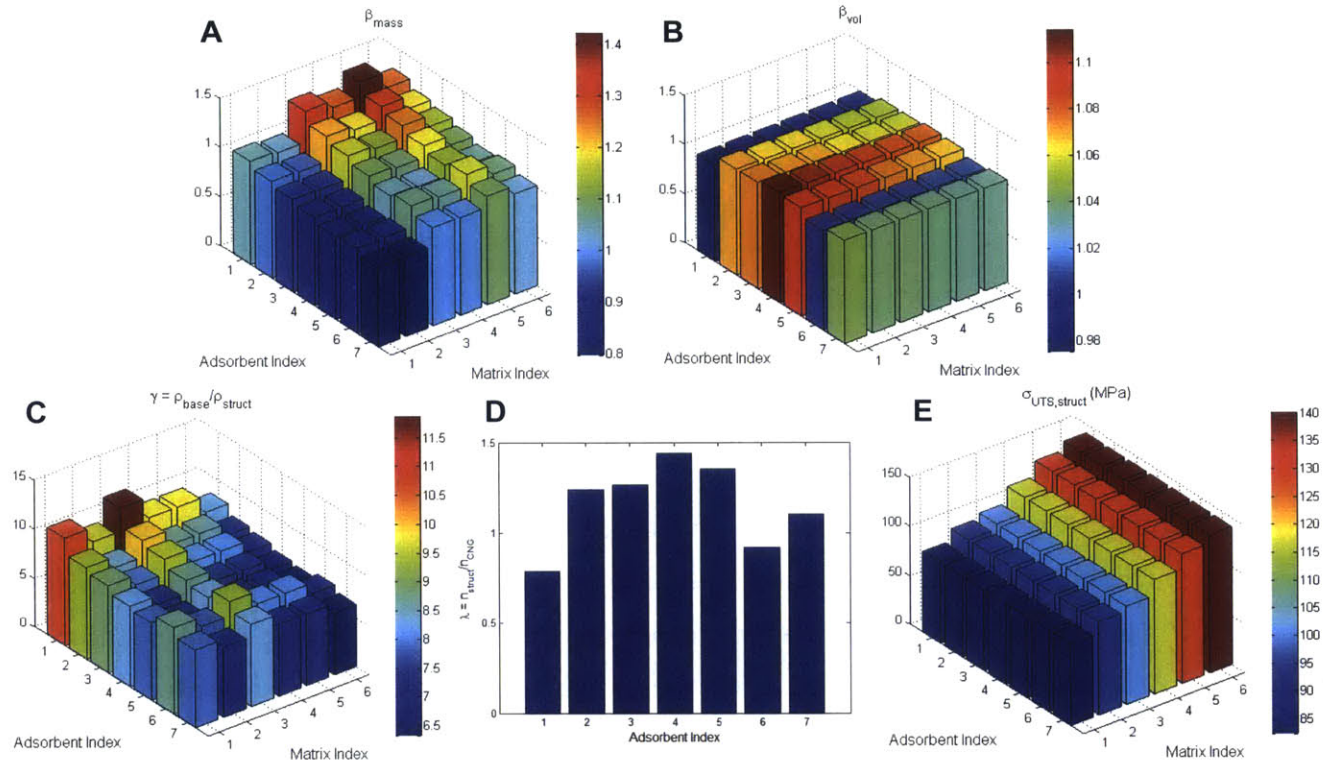

Figure 64. Structubent figures of merit at 3.5 MPa, ϵ = 0.4, and $\sigma_{UTS,ads}$ = 200 MPa compared to a steel CNG cylidner. (A) Ratio of mass specific methane capacities as a function of combining specific adsorbents and matrix materials together. The indices of materials correspond with those in Table 16 and Table 17. (B) Ratio of volume specific capacities. (C) Ratios of densities of baseline material and composite structubent layer. (D) Ratio of molar densities of composite structubent layer for each adsorbent material. (E) Ultimate tensile strength of the composite structubent layer for each adsorbent/matrix material combination.

A simplification of this model is the fact that we assume the adsorbent particles experience the internal pressure of methane at all points in the structubent layer, and that there is only a structubent layer making up the pressure vessel. This type of geometry would result in a leaky pressure vessel, as methane diffuses out of the structubent layer, although the structubent layer itself would remain well under the maximum burst ratio. Real implementation of this concept would require a very thin gastight layer, such as a thin layer of metal, to be adhered to the structubent layer. Emerging barrier materials such as graphene or other 2D composite fillers could also be utilized. The continuous, non-void regions of the structubent material would bear essentially all of the hoop stress, and the interfacial pressure between the structubent layer and outer shell would be close to atmospheric pressure, allowing the outer shell to be quite thin. However, the void regions of the structubent layer, at equilibrium, would be all at the internal pressure due to diffusion of

methane though the matrix. The sealing of multiple layers of materials and composites is not trivial, but possible. For example, carbon-fiber layers used in current composites are employed alongside a gastight liner on the inside of the pressure vessel.

9.2.3 Conclusion

In conclusion, we have introduced a new concept that may be enabling for compressed natural gas (CNG) transportation. The combination of methane adsorbent filler particles for the formation of a polymer composite shell allows for the unique engineering of a combination of constraints on the CNG problem. We show that it is possible to increase specific capacity by utilizing a combination of mechanical reinforcement of a lower density composite layer, and increased volumetric capacity of that layer for methane. This work derives the appropriate figures of merit for such materials, relating critical material properties to increased capacity. The structubent concept may find application to other gas storage problems.

References

1. Branton, D.; Deamer, D. W.; Marziali, A.; Bayley, H.; Benner, S. A.; Butler, T.; Di Ventra, M.; Garaj, S.; Hibbs, A.; Huang, X.; Jovanovich, S. B.; Krstic, P. S.; Lindsay, S.; Ling, X. S.; Mastrangelo, C. H.; Meller, A.; Oliver, J. S.; Pershin, Y. V.; Ramsey, J. M.; Riehn, R.; Soni, G. V.; Tabard-Cossa, V.; Wanunu, M.; Wiggin, M.; Schloss, J. A., The Potential and Challenges of Nanopore Sequencing. *Nat Biotech* **2008,** *26* (10), 1146-1153.
2. Manrao, E. A.; Derrington, I. M.; Laszlo, A. H.; Langford, K. W.; Hopper, M. K.; Gillgren, N.; Pavlenok, M.; Niederweis, M.; Gundlach, J. H., Reading DNA at Single-Nucleotide Resolution with a Mutant Mspa Nanopore and Phi29 DNA Polymerase. *Nat Biotech* **2012,** *30* (4), 349-353.
3. Deamer, D. W.; Branton, D., Characterization of Nucleic Acids by Nanopore Analysis. *Accounts of chemical research* **2002,** *35* (10), 817-825.
4. Clarke, J.; Wu, H.-C.; Jayasinghe, L.; Patel, A.; Reid, S.; Bayley, H., Continuous Base Identification for Single-Molecule Nanopore DNA Sequencing. *Nat Nano* **2009,** *4* (4), 265-270.
5. Storm, A. J.; Chen, J. H.; Ling, X. S.; Zandbergen, H. W.; Dekker, C., Fabrication of Solid-State Nanopores with Single-Nanometre Precision. *Nature Materials* **2003,** *2* (8), 537-540.
6. Li, J.; Stein, D.; McMullan, C.; Branton, D.; Aziz, M. J.; Golovchenko, J. A., Ion-Beam Sculpting at Nanometre Length Scales. *Nature* **2001,** *412* (6843), 166-169.
7. Li, N.; Yu, S.; Harrell, C. C.; Martin, C. R., Conical Nanopore Membranes. Preparation and Transport Properties. *Analytical Chemistry* **2004,** *76* (7), 2025-2030.
8. Siwy, Z.; Heins, E.; Harrell, C. C.; Kohli, P.; Martin, C. R., Conical-Nanotube Ion-Current Rectifiers: The Role of Surface Charge. *Journal of the American Chemical Society* **2004,** *126* (35), 10850-10851.
9. Siwy, Z.; Trofin, L.; Kohli, P.; Baker, L. A.; Trautmann, C.; Martin, C. R., Protein Biosensors Based on Biofunctionalized Conical Gold Nanotubes. *Journal of the American Chemical Society* **2005,** *127* (14), 5000-5001.
10. Kresge, C. T.; Leonowicz, M. E.; Roth, W. J.; Vartuli, J. C.; Beck, J. S., Ordered Mesoporous Molecular Sieves Synthesized by a Liquid-Crystal Template Mechanism. *Nature* **1992,** *359* (6397), 710-712.
11. Davis, M. E.; Lobo, R. F., Zeolite and Molecular Sieve Synthesis. *Chemistry of Materials* **1992,** *4* (4), 756-768.
12. Vallet-Regi, M.; Rámila, A.; del Real, R. P.; Pérez-Pariente, J., A New Property of Mcm-41: Drug Delivery System. *Chemistry of Materials* **2000,** *13* (2), 308-311.
13. Geim, A. K.; Novoselov, K. S., The Rise of Graphene. *Nat Mater* **2007,** *6* (3), 183-191.
14. Schneider, G. g. F.; Kowalczyk, S. W.; Calado, V. E.; Pandraud, G. g.; Zandbergen, H. W.; Vandersypen, L. M. K.; Dekker, C., DNA Translocation through Graphene Nanopores. *Nano Letters* **2010,** *10* (8), 3163-3167.
15. TraversiF; RaillonC; Benameur, S. M.; LiuK; KhlybovS; TosunM; KrasnozhonD; KisA; RadenovicA, Detecting the Translocation of DNA through a Nanopore Using Graphene Nanoribbons. *Nat Nano* **2013,** *8* (12), 939-945.
16. Holt, J. K.; Park, H. G.; Wang, Y.; Stadermann, M.; Artyukhin, A. B.; Grigoropoulos, C. P.; Noy, A.; Bakajin, O., Fast Mass Transport through Sub-2-Nanometer Carbon Nanotubes. *Science* **2006,** *312* (5776), 1034-1037.
17. Hinds, B. J.; Chopra, N.; Rantell, T.; Andrews, R.; Gavalas, V.; Bachas, L. G., Aligned Multiwalled Carbon Nanotube Membranes. *Science* **2004,** *303* (5654), 62-65.

18. Fornasiero, F.; Park, H. G.; Holt, J. K.; Stadermann, M.; Grigoropoulos, C. P.; Noy, A.; Bakajin, O., Ion Exclusion by Sub-2-Nm Carbon Nanotube Pores. *Proceedings of the National Academy of Sciences* **2008,** *105* (45), 17250-17255.
19. Lee, C. Y.; Choi, W.; Han, J.-H.; Strano, M. S., Coherence Resonance in a Single-Walled Carbon Nanotube Ion Channel. *Science* **2010,** *329* (5997), 1320-1324.
20. Zhu, Y.; Granick, S., Limits of the Hydrodynamic No-Slip Boundary Condition. *Physical Review Letters* **2002,** *88* (10), 106102.
21. Majumder, M.; Chopra, N.; Hinds, B. J., Effect of Tip Functionalization on Transport through Vertically Oriented Carbon Nanotube Membranes. *Journal of the American Chemical Society* **2005,** *127* (25), 9062-9070.
22. Javadpour, F., Nanopores and Apparent Permeability of Gas Flow in Mudrocks (Shales and Siltstone). *Journal of Canadian Petroleum Technology* **2009,** *48* (8), 16-21.
23. Mann, D. J.; Halls, M. D., Water Alignment and Proton Conduction inside Carbon Nanotubes. *Physical Review Letters* **2003,** *90* (19), 195503.
24. H, C. W., Means for Counting Particles Suspended in a Fluid. Google Patents: 1953.
25. Ito, T.; Sun, L.; Henriquez, R. R.; Crooks, R. M., A Carbon Nanotube-Based Coulter Nanoparticle Counter. *Accounts of chemical research* **2004,** *37* (12), 937-45.
26. Keshavarzi, T.; Sohrabi, R.; Mansoori, G. A., An Analytic Model for Nano Confined Fluids Phase-Transition: Applications for Confined Fluids in Nanotube and Nanoslit. *Journal of Computational and Theoretical Nanoscience* **2006,** *3* (1), 134-141.
27. Mataz, A.; Gregory, B. M., Effects of Confinement on Material Behaviour at the Nanometre Size Scale. *Journal of Physics: Condensed Matter* **2005,** *17* (15), R461.
28. Javadpour, F., Nanopores and Apparent Permeability of Gas Flow in Mudrocks (Shales and Siltstone). *Journal of Canadian Petroleum Technology* **2003**, 1-6.
29. Hilder, T. A.; Hill, J. M., Modeling the Loading and Unloading of Drugs into Nanotubes. *Small* **2009,** *5* (3), 300-308.
30. Zalba, B.; Marín, J. M.; Cabeza, L. F.; Mehling, H., Review on Thermal Energy Storage with Phase Change: Materials, Heat Transfer Analysis and Applications. *Applied Thermal Engineering* **2003,** *23* (3), 251-283.
31. Kim, S.; Jinschek, J. R.; Chen, H.; Sholl, D. S.; Marand, E., Scalable Fabrication of Carbon Nanotube/Polymer Nanocomposite Membranes for High Flux Gas Transport. *Nano Letters* **2007,** *7* (9), 2806-2811.
32. Fornasiero, F.; In, J. B.; Kim, S.; Park, H. G.; Wang, Y.; Grigoropoulos, C. P.; Noy, A.; Bakajin, O., Ph-Tunable Ion Selectivity in Carbon Nanotube Pores. *Langmuir* **2010,** *26* (18), 14848-14853.
33. Zhu, F.; Schulten, K., Water and Proton Conduction through Carbon Nanotubes as Models for Biological Channels. *Biophysical Journal* **2003,** *85* (1), 236-244.
34. Choi, W.; Lee, C. Y.; Ham, M.-H.; Shimizu, S.; Strano, M. S., Dynamics of Simultaneous, Single Ion Transport through Two Single-Walled Carbon Nanotubes: Observation of a Three-State System. *Journal of the American Chemical Society* **2010,** *133* (2), 203-205.
35. Koga, K.; Gao, G. T.; Tanaka, H.; Zeng, X. C., Formation of Ordered Ice Nanotubes inside Carbon Nanotubes. *Nature* **2001,** *412* (6849), 802-805.
36. Dresselhaus, M. S.; Dresselhaus, G.; Saito, R.; Jorio, A., Raman Spectroscopy of Carbon Nanotubes. *Physics Reports* **2005,** *409* (2), 47-99.
37. Shimizu, S.; Choi, W.; Abrahamson, J. T.; Strano, M. S., New Concepts in Molecular and Energy Transport within Carbon Nanotubes: Thermopower Waves and Stochastically Resonant Ion Channels. *physica status solidi (b)* **2011**.

38. Jorio, A.; Saito, R.; Hafner, J. H.; Lieber, C. M.; Hunter, M.; McClure, T.; Dresselhaus, G.; Dresselhaus, M. S., Structural (N, M) Determination of Isolated Single-Wall Carbon Nanotubes by Resonant Raman Scattering. *Physical Review Letters* **2001,** *86* (6), 1118-1121.
39. Brown, S. D. M.; Jorio, A.; Corio, P.; Dresselhaus, M. S.; Dresselhaus, G.; Saito, R.; Kneipp, K., Origin of the Breit-Wigner-Fano Lineshape of the Tangential G-Band Feature of Metallic Carbon Nanotubes. *Physical Review B* **2001,** *63* (15), 155414.
40. Jorio, A.; Souza Filho, A. G.; Dresselhaus, G.; Dresselhaus, M. S.; Swan, A. K.; Ünlü, M. S.; Goldberg, B. B.; Pimenta, M. A.; Hafner, J. H.; Lieber, C. M.; Saito, R., G-Band Resonant Raman Study of 62 Isolated Single-Wall Carbon Nanotubes. *Physical Review B* **2002,** *65* (15), 155412.
41. Choi, W.; Ulissi, Z. W.; Shimizu, S. F. E.; Bellisario, D. O.; Ellison, M. D.; Strano, M. S., Diameter-Dependent Ion Transport through the Interior of Isolated Single-Walled Carbon Nanotubes. *Nat Commun* **2013,** *4*.
42. Bezrukov, S. M.; Vodyanoy, I.; Parsegian, V. A., Counting Polymers Moving through a Single Ion Channel. *Nature* **1994,** *370* (6487), 279-281.
43. Kasianowicz, J. J.; Robertson, J. W. F.; Chan, E. R.; Reiner, J. E.; Stanford, V. M., Nanoscopic Porous Sensors. *Annual Review of Analytical Chemistry* **2008,** *1* (1), 737-766.
44. Ulissi, Z. W.; Shimizu, S.; Lee, C. Y.; Strano, M. S., Carbon Nanotubes as Molecular Conduits: Advances and Challenges for Transport through Isolated Sub-2 Nm Pores. *The Journal of Physical Chemistry Letters* **2011,** *2* (22), 2892-2896.
45. Powell, M. R.; Cleary, L.; Davenport, M.; Shea, K. J.; Siwy, Z. S., Electric-Field-Induced Wetting and Dewetting in Single Hydrophobic Nanopores. *Nature Nanotechnology* **2011,** (October), 1-5.
46. Dekker, C., Solid-State Nanopores. **2007,** *2* (4), 209-215.
47. Hou, X.; Zhang, H.; Jiang, L., Building Bio-Inspired Artificial Functional Nanochannels: From Symmetric to Asymmetric Modification. *Angewandte Chemie International Edition* **2012**, n/a-n/a.
48. Sakmann, B.; Neher, E., Patch Clamp Techniques for Studying Ionic Channels in Excitable Membranes. *Annual Review of Physiology* **1984,** *46* (1), 455-472.
49. Sachs, F.; Qin, F., Gated, Ion-Selective Channels Observed with Patch Pipettes in the Absence of Membranes: Novel Properties of a Gigaseal. *Biophysical journal* **1993,** *65* (3), 1101-7.
50. Grzywna, Z. J.; S. Liebovitch, L.; Siwy, Z., A Dual Mode Mechanism of Conductance through Fine Porous Membranes. *Journal of Membrane Science* **1998,** *145* (2), 253-263.
51. Chen, C.-C.; Zhou, Y.; Baker, L. A., Scanning Ion Conductance Microscopy. *Annual Review of Analytical Chemistry* **2011**.
52. Behrends, J. C.; Fertig, N., Planar Patch Clamping. In *Patch Clamp Analysis*, 2 ed.; Walz, W., Ed. Humana Press: 2007.
53. Lev, A. A.; Korchev, Y. E.; Rostovtseva, T. K.; Bashford, C. L.; Edmonds, D. T.; Pasternak, C. A., Rapid Switching of Ion Current in Narrow Pores: Implications for Biological Ion Channels. *Proceedings of the Royal Society of London. Series B: Biological Sciences* **1993,** *252* (1335), 187-192.
54. Pasternak, C. a.; Bashford, C. L.; Korchev, Y. E.; Rostovtseva, T. K.; Lev, A. a., Modulation of Surface Flow by Divalent Cations and Protons. *Colloids and Surfaces A: Physicochemical and Engineering Aspects* **1993,** *77* (2), 119-124.
55. Lisensky, G. C.; Campbell, D. J.; Beckman, K. J.; Calderon, C. E.; Doolan, P. W.; Rebecca, M. O.; Ellis, A. B., Replication and Compression of Surface Structures with Polydimethylsiloxane Elastomer. *Journal of Chemical Education* **1999,** *76* (4), 537.
56. Merkel, T. C.; Bondar, V. I.; Nagai, K.; Freeman, B. D.; Pinnau, I., Gas Sorption, Diffusion, and Permeation in Poly(Dimethylsiloxane). *Journal of Polymer Science Part B: Polymer Physics* **2000,** *38* (3), 415-434.

57. Randall, G. C.; Doyle, P. S., Permeation-Driven Flow in Poly(Dimethylsiloxane) Microfluidic Devices. *Proceedings of the National Academy of Sciences of the United States of America* **2005,** *102* (31), 10813-10818.
58. Peter, C.; Hummer, G., Ion Transport through Membrane-Spanning Nanopores Studied by Molecular Dynamics Simulations and Continuum Electrostatics Calculations. *Biophysical Journal* **2005,** *89* (4), 2222-2234.
59. Ho, C.; Qiao, R.; Heng, J. B.; Chatterjee, A.; Timp, R. J.; Aluru, N. R.; Timp, G., Electrolytic Transport through a Synthetic Nanometer-Diameter Pore. *Proceedings of the National Academy of Sciences of the United States of America* **2005,** *102* (30), 10445-10450.
60. Smeets, R. M. M.; Keyser, U. F.; Krapf, D.; Wu, M.-Y.; Dekker, N. H.; Dekker, C., Salt Dependence of Ion Transport and DNA Translocation through Solid-State Nanopores. *Nano Letters* **2006,** *6* (1), 89-95.
61. Buyukdagli, S.; Manghi, M.; Palmeri, J., Ionic Capillary Evaporation in Weakly Charged Nanopores. *Physical Review Letters* **2010,** *105* (15), 158103.
62. Powell, M. R.; Sullivan, M.; Vlassiouk, I.; Constantin, D.; Sudre, O.; Martens, C. C.; Eisenberg, R. S.; Siwy, Z. S., Nanoprecipitation-Assisted Ion Current Oscillations. *Nat Nano* **2008,** *3* (1), 51-57.
63. Beckstein, O.; Sansom, M. S. P., Liquid-Vapor Oscillations of Water in Hydrophobic Nanopores. *Proceedings of the National Academy of Sciences of the United States of America* **2003,** *100* (12), 7063-8.
64. Allen, R.; Melchionna, S.; Hansen, J.-P., Intermittent Permeation of Cylindrical Nanopores by Water. *Physical Review Letters* **2002,** *89* (17), 2-5.
65. Serp, P.; Castillejos, E., Catalysis in Carbon Nanotubes. *ChemCatChem* **2010,** *2* (1), 41-47.
66. Beu, T. A., Molecular Dynamics Simulations of Ion Transport through Carbon Nanotubes. I. Influence of Geometry, Ion Specificity, and Many-Body Interactions. *The Journal of Chemical Physics* **2010,** *132* (16), 164513-15.
67. Hummer, G.; Rasaiah, J. C.; Noworyta, J. P., Water Conduction through the Hydrophobic Channel of a Carbon Nanotube. *Nature* **2001,** *414* (6860), 188-190.
68. Takaiwa, D.; Hatano, I.; Koga, K.; Tanaka, H., Phase Diagram of Water in Carbon Nanotubes. *Proceedings of the National Academy of Sciences* **2008,** *105* (1), 39-43.
69. Pascal, T. A.; Goddard, W. A.; Jung, Y., Entropy and the Driving Force for the Filling of Carbon Nanotubes with Water. *Proceedings of the National Academy of Sciences* **2011,** *108* (29), 11794-11798.
70. Green, M. L. H.; Tsang, S. C. Method of Opening and Filling Carbon Nanotubes. 6090363, 2000.
71. Tsang, S. C.; Chen, Y. K.; Harris, P. J. F.; Green, M. L. H., A Simple Chemical Method of Opening and Filling Carbon Nanotubes. *Nature* **1994,** *372* (6502), 159-162.
72. Wenseleers, W.; Cambré, S.; Čulin, J.; Bouwen, A.; Goovaerts, E., Effect of Water Filling on the Electronic and Vibrational Resonances of Carbon Nanotubes: Characterizing Tube Opening by Raman Spectroscopy. *Advanced Materials* **2007,** *19* (17), 2274-2278.
73. Mamontov, E.; Burnham, C. J.; Chen, S.-H.; Moravsky, A. P.; Loong, C.-K.; de Souza, N. R.; Kolesnikov, A. I., Dynamics of Water Confined in Single- and Double-Wall Carbon Nanotubes. *The Journal of Chemical Physics* **2006,** *124* (19), -.
74. Maniwa, Y.; Kataura, H.; Abe, M.; Suzuki, S.; Achiba, Y.; Kira, H.; Matsuda, K., Phase Transition in Confined Water inside Carbon Nanotubes. *Journal of the Physical Society of Japan* **2002,** *71* (12), 2863-2866.
75. Ghosh, S.; Ramanathan, K. V.; Sood, A. K., Water at Nanoscale Confined in Single-Walled Carbon Nanotubes Studied by Nmr. *EPL (Europhysics Letters)* **2004,** *65* (5), 678.
76. Hua, F.; Sun, Y.; Gaur, A.; Meitl, M. A.; Bilhaut, L.; Rotkina, L.; Wang, J.; Geil, P.; Shim, M.; Rogers, J. A.; Shim, A., Polymer Imprint Lithography with Molecular-Scale Resolution. *Nano Letters* **2004,** *4* (12), 2467-2471.

77. Li, H. D.; Yue, K. T.; Lian, Z. L.; Zhan, Y.; Zhou, L. X.; Zhang, S. L.; Shi, Z. J.; Gu, Z. N.; Liu, B. B.; Yang, R. S.; Yang, H. B.; Zou, G. T.; Zhang, Y.; Iijima, S., Temperature Dependence of the Raman Spectra of Single-Wall Carbon Nanotubes. *Applied Physics Letters* **2000,** *76* (15), 2053-2055.
78. Zhang, Y.; Son, H.; Zhang, J.; Kong, J.; Liu, Z., Laser-Heating Effect on Raman Spectra of Individual Suspended Single-Walled Carbon Nanotubes. *The Journal of Physical Chemistry C* **2007,** *111* (5), 1988-1992.
79. Zhang, Y.; Xie, L.; Zhang, J.; Wu, Z.; Liu, Z., Temperature Coefficients of Raman Frequency of Individual Single-Walled Carbon Nanotubes. *The Journal of Physical Chemistry C* **2007,** *111* (38), 14031-14034.
80. Longhurst, M. J.; Quirke, N., The Environmental Effect on the Radial Breathing Mode of Carbon Nanotubes. Ii. Shell Model Approximation for Internally and Externally Adsorbed Fluids. *The Journal of Chemical Physics* **2006,** *125* (18), -.
81. Sliwinska-Bartkowiak, M.; Jazdzewska, M.; Huang, L. L.; Gubbins, K. E., Melting Behavior of Water in Cylindrical Pores: Carbon Nanotubes and Silica Glasses. *Physical Chemistry Chemical Physics* **2008,** *10* (32), 4909-4919.
82. Kruk, M.; Jaroniec, M.; Sayari, A., Application of Large Pore Mcm-41 Molecular Sieves to Improve Pore Size Analysis Using Nitrogen Adsorption Measurements. *Langmuir* **1997,** *13* (23), 6267-6273.
83. Vroon, Z. A. E. P.; Keizer, K.; Gilde, M. J.; Verweij, H.; Burggraaf, A. J., Transport Properties of Alkanes through Ceramic Thin Zeolite Mfi Membranes. *Journal of Membrane Science* **1996,** *113* (2), 293-300.
84. Jahnert, S.; Vaca Chavez, F.; Schaumann, G. E.; Schreiber, A.; Schonhoff, M.; Findenegg, G. H., Melting and Freezing of Water in Cylindrical Silica Nanopores. *Physical Chemistry Chemical Physics* **2008,** *10* (39), 6039-6051.
85. Alba-Simionesco, C.; Coasne, B.; Dosseh, G.; Dudziak, G.; Gubbins, K. E.; Radhakrishnan, R.; Sliwinska-Bartkowiak, M., Effects of Confinement on Freezing and Melting. *Journal of Physics: Condensed Matter* **2006,** *18* (6), R15.
86. Jackson, C. L.; McKenna, G. B., The Melting Behavior of Organic Materials Confined in Porous Solids. *The Journal of Chemical Physics* **1990,** *93* (12), 9002-9011.
87. Lei, Y. A.; Bykov, T.; Yoo, S.; Zeng, X. C., The Tolman Length: Is It Positive or Negative? *Journal of the American Chemical Society* **2005,** *127* (44), 15346-15347.
88. Digilov, R. M., Semi-Empirical Model for Prediction of Crystal–Melt Interfacial Tension. *Surface Science* **2004,** *555* (1–3), 68-74.
89. Morishige, K.; Kawano, K., Freezing and Melting of Water in a Single Cylindrical Pore: The Pore-Size Dependence of Freezing and Melting Behavior. *The Journal of Chemical Physics* **1999,** *110* (10), 4867-4872.
90. Hugo, K. C., Confinement Effects on Freezing and Melting. *Journal of Physics: Condensed Matter* **2001,** *13* (11), R95.
91. Makkonen, L., On the Methods to Determine Surface Energies. *Langmuir* **2000,** (16), 7669-7672.
92. Findenegg, G. H.; Jähnert, S.; Akcakayiran, D.; Schreiber, A., Freezing and Melting of Water Confined in Silica Nanopores. *ChemPhysChem* **2008,** *9* (18), 2651-2659.
93. Kanda, H.; Miyahara, M.; Higashitani, K., Triple Point of Lennard-Jones Fluid in Slit Nanopore: Solidification of Critical Condensate. *The Journal of Chemical Physics* **2004,** *120* (13), 6173-6179.
94. Shin, J.-H.; Parlange, J.-Y.; Deinert, M. R., Scale Effects in the Latent Heat of Melting in Nanopores. *The Journal of Chemical Physics* **2013,** *139* (4), -.
95. Tolman, R. C., The Effect of Droplet Size on Surface Tension. *The Journal of Chemical Physics* **1949,** *17* (3), 333-337.

96. Turnbull, D., Formation of Crystal Nuclei in Liquid Metals. *Journal of Applied Physics* **1950,** *21* (10), 1022-1028.
97. Okui, N., Theoretical Aspect of Crystallization Temperature at Maximum Crystal Growth Rate. *Polym J* **1987,** *19* (11), 1309-1315.
98. Broughton, J. Q.; Gilmer, G. H., Molecular Dynamics of the Crystal–Fluid Interface. V. Structure and Dynamics of Crystal–Melt Systems. *The Journal of Chemical Physics* **1986,** *84* (10), 5749-5758.
99. Blagden, N.; de Matas, M.; Gavan, P. T.; York, P., Crystal Engineering of Active Pharmaceutical Ingredients to Improve Solubility and Dissolution Rates. *Advanced Drug Delivery Reviews* **2007,** *59* (7), 617-630.
100. O'Mahony, M.; Leung, A. K.; Ferguson, S.; Trout, B. L.; Myerson, A. S., A Process for the Formation of Nanocrystals of Active Pharmaceutical Ingredients with Poor Aqueous Solubility in a Nanoporous Substrate. *Organic Process Research & Development* **2014.**
101. Liu, H.; Nishide, D.; Tanaka, T.; Kataura, H., Large-Scale Single-Chirality Separation of Single-Wall Carbon Nanotubes by Simple Gel Chromatography. *Nat Commun* **2011,** *2*, 309.
102. Choi, S.; Drese, J. H.; Jones, C. W., Adsorbent Materials for Carbon Dioxide Capture from Large Anthropogenic Point Sources. *ChemSusChem* **2009,** *2* (9), 796-854.
103. Bottoms, R. R., Organic Bases for Gas Purification. *Industrial and Engineering Chemistry* **1931,** *23* (5), 501-504.
104. Deshmukh, R. D.; Mather, A. E., A Mathematical Model for Equilibrium Solubility of Hydrogen Sulfide and Carbon Dioxide in Aqueous Alkanolamine Solutions. *Chemical Engineering Science* **1981,** *36* (2), 355-362.
105. Frazier, H. D.; Kohl, A. L., Selective Absorption of Hydrogen Sulfide from Gas Streams. *Industrial and Engineering Chemistry* **1950,** *42* (11), 2288-2292.
106. Rao, A. B.; Rubin, E. S., A Technical, Economic, and Environmental Assessment of Amine-Based Co2 Capture Technology for Power Plant Greenhouse Gas Control. *Environmental Science and Technology* **2002,** *36* (20), 4467-4475.
107. Leal, O.; Bolivar, C.; Ovalles, C.; Garcia, J. J.; Espidel, Y., Reversible Adsorption of Carbon Dioxide on Amine Surface-Bonded Silica Gel. *Inorganica Chimica Acta* **1995,** *240* (1-2), 183-189.
108. Gray, M. L.; Hoffman, J. S.; Hreha, D. C.; Fauth, D. J.; Hedges, S. W.; Champagne, K. J.; Pennline, H. W., Parametric Study of Solid Amine Sorbents for the Capture of Carbon Dioxide. *Energy Fuels* **2009,** *23* (10), 4840-4844.
109. Zelenak, V.; Badanicova, M.; Halamova, D.; Cejka, J.; Zukal, A.; Murafa, N.; Goerigk, G., Amine-Modified Ordered Mesoporous Silica: Effect of Pore Size on Carbon Dioxide Capture. *Chemical Engineering Journal* **2008,** *144* (2), 336-342.
110. Serna-Guerrero, R.; Belmabkhout, Y.; Sayari, A., Modeling Co2 Adsorption on Amine-Functionalized Mesoporous Silica: 1. A Semi-Empirical Equilibrium Model. *Chemical Engineering Journal* **2010,** *161* (1-2), 173-181.
111. Masel, R. I., *Principles of Adsorption and Reaction on Solid Surfaces*. Wily-IEEE: 1996; p 804.
112. Hiyoshi, N.; Yogo, K.; Yashima, T., Adsorption Characteristics of Carbon Dioxide on Organically Functionalized Sba-15. *Microporous and Mesoporous Materials* **2005,** *84* (1-3), 357-365.
113. da Silva, E. F.; Svendsen, H. F., Computational Chemistry Study of Reactions, Equilibrium and Kinetics of Chemical Co2 Absorption. *8th International Conference on Greenhouse Gas Control Technologies - GHGT-8* **2007,** *1* (2), 151-157.
114. Dell'Amico, D. B.; Calderazzo, F.; Labella, L.; Marchetti, F.; Pampaloni, G., Converting Carbon Dioxide into Carbamato Derivatives. *Chemical Reviews* **2003,** *103* (1), 3857-3897.

115. Knofel, C.; Martin, C. l.; Hornebecq, V.; Llewellyn, P. L., Study of Carbon Dioxide Adsorption on Mesoporous Aminopropylsilane-Functionalized Silica and Titania Combining Microcalorimetry and in Situ Infrared Spectroscopy. *Journal of Physical Chemistry C* **2009,** *113* (52), 21726-21734.
116. Crooks, J. E.; Donnellan, J. P., Kinetics and Mechanism of the Reaction between Carbon Dioxide and Amines in Aqueous Solution. *J. Chem. Soc., Perkin Trans. 2* **1989**, 331-333.
117. Flory, P. J., Thermodynamics of High Polymer Solutions. *Journal of Chemical Physics* **1942,** *10* (1), 51-61.
118. Kasteleyn, P. W., The Statistics of Dimers on a Lattice, I. The Number of Dimer Arrangements on a Quadratic Lattice. *Physica* **1961,** *27* (12), 1209-1225.
119. Ramirez-Pastor, A. J.; Eggarter, T. P.; Pereyra, V. D.; Riccardo, J. L., Statistical Thermodynamics and Transport of Linear Adsorbates. *Physical Review B: Condensed Matter and Materials Physics* **1999,** *59* (16), 11027-11036.
120. Roma, F.; Ramirez-Pastor, A. J.; Riccardo, J. L., Multisite Occupancy Adsorption: Comparative Study of New Different Analytical Approaches. *Langmuir* **2003,** *19* (17), 6770-6777.
121. Roma, F.; Ramirez-Pastor, A. J.; Riccardo, J. L., A New Theoretical Approach to Multilayer Adsorption of Polyatomics. *Surface Science* **2005,** *583* (2-3), 213-228.
122. Nitta, T.; Kiriyama, H.; Shigeta, T., Monte Carlo Simulation Study for Adsorption of Dimers on Random Heterogeneous Surfaces. *Langmuir* **1997,** *13* (903), 908.
123. Ramirez-Pastor, A. J.; Riccardo, J. L.; Pereyra, V., Adsorption of Linear K-Mers on Heterogeneous Surfaces with Simple Topographies. *Langmuir* **2000,** *16* (2), 682-689.
124. Aranovich, G. L.; Erickson, J. S.; Donohue, M. D., Lattice Gas 2d/3d Equilibria: Chemical Potentials and Adsorption Isotherms with Correct Critical Points. *Journal of Chemical Physics* **2004,** *120* (11), 5208-5216.
125. Sips, R., On the Structure of a Catalyst Surface. *Journal of Chemical Physics* **1948,** *16* (5), 490-495.
126. Talu, O.; Myers, A. L., Rigorous Thermodynamic Treatment of Gas Adsorption. *AIChE Journal* **1988,** *34* (11), 1887-1893.
127. Other empirical equations that were attempted to fit the data included the Langmuir equation, the Toth equation, and the Freundlich equation.
128. For example, if the histogram shows that the all the amines have z = 2, and the z = 2 surface has a maximum density of 0.5, then the possible range of θamine,0 for the overall surface is from 0.5 to 0 (lower θamine,0 is always possible by adding in empty space). If the constant-z surface were more spread out, such that θz = 0.3, for example, then the range of θamine,0 would only be from 0.3 to 0. The difference in range of θamine,0also leads to the difference in ranges of θCO2 predicted.
129. Press, W. H.; Teukolsky, S. A.; Vetterling, W. T.; Flannery, B. P., Confidence Limits on Estimated Model Parameters. In *Numerical Recipes in Fortran 77: The Art of Scientific Computing*, 2 ed.; 1992; pp 684-694.
130. Kim, S.; Ida, J.; Guliants, V. V.; Lin, Y. S., Tailoring Pore Properties of Mcm-48 Silica for Selective Adsorption of Co2. *Journal of Physical Chemistry B* **2005,** *109* (13), 6287-6293.
131. Zelenak, V.; Halamova, D.; Gaberova, L.; Bloch, E.; Llewellyn, P., Amine-Modified Sba-12 Mesoporous Silica for Carbon Dioxide Capture: Effect of Amine Basicity on Sorption Properties. *Microporous and Mesoporous Materials* **2008,** *116* (1-3), 358-364.
132. Kozlova, S. A.; Kirik, S. D., Post-Synthetic Activation of Silanol Covering in the Mesostructured Silicate Materials Mcm-41 and Sba-15. *Microporous and Mesoporous Materials* **2010,** *133* (1-3), 124-133.

133. Langeroudi, E. G.; Kleitz, F.; Iliuta, M. C.; Larachi, F., Grafted Amine/Co2 Interactions in (Gas-)Liquid-Solid Adsorption/Absorption Equilibria. *Journal of Physical Chemistry C* **2009,** *113* (52), 21866-21876.
134. Zheng, F.; Tran, D. N.; Busche, B. J.; Fryxell, G. E.; Addleman, R. S.; Zemanian, T. S.; Aardahl, C. L., Ethylenediamine-Modified Sba-15 as Regenerable Co2 Sorbent. *Industrial & Engineering Chemistry Research* **2005,** *44* (9), 3099-3105.
135. Xu, X.; Song, C.; Andresen, J. M.; Miller, B. G.; Scaroni, A. W., Novel Polyethylenimine-Modified Mesoporous Molecular Sieve of Mcm-41 Type as High-Capacity Adsorbent for Co2 Capture. *Energy & Fuels* **2002,** *16* (6), 1463-1469.
136. Hicks, J. C.; Drese, J. H.; Fauth, D. J.; Gray, M. L.; Qi, G.; Jones, C. W., Designing Adsorbents for Co2 Capture from Flue Gas-Hyperbranched Aminosilicas Capable of Capturing Co2 Reversibly. *Journal of the American Chemical Society* **2008,** *130* (10), 2902-2903.
137. Kotelyanskii, M.; Theodorou, D. N., *Simulation Methods for Polymers*. CRC Press: 2004; p 602.
138. Satyapal, S.; Filburn, T.; Trela, J.; Strange, J., Performance and Properties of a Solid Amine Sorbent for Carbon Dioxide Removal in Space Life Support Applications. *Energy & Fuels* **2001,** *15* (2), 250-255.
139. Son, W.-J.; Choi, J.-S.; Ahn, W.-S., Adsorptive Removal of Carbon Dioxide Using Polyethyleneimine-Loaded Mesoporous Silica Materials. *Microporous and Mesoporous Materials* **2008,** *113* (1-3), 31-40.
140. Xu, X.; Song, C.; Andrésen, J. M.; Miller, B. G.; Scaroni, A. W., Preparation and Characterization of Novel Co2 "Molecular Basket" Adsorbents Based on Polymer-Modified Mesoporous Molecular Sieve Mcm-41. *Microporous and Mesoporous Materials* **2003,** *62* (1-2), 29-45.
141. Yue, M. B.; Chun, Y.; Cao, Y.; Dong, X.; Zhu, J. H., Co2 Capture by as-Prepared Sba-15 with an Occluded Organic Template. *Advanced Functional Materials* **2006,** *16* (13), 1717-1722.
142. Yue, M. B.; Sun, L. B.; Cao, Y.; Wang, Y.; Wang, Z. J.; Zhu, J. H., Efficient Co2 Capturer Derived from as-Synthesized Mcm-41 Modified with Amine. *Chemistry – A European Journal* **2008,** *14* (11), 3442-3451.
143. McCann, N.; Maeder, M.; Attalla, M., Simulation of Enthalpy and Capacity of Co2 Absorption by Aqueous Amine Systems. *Industrial & Engineering Chemistry Research* **2008,** *47* (6), 2002-2009.
144. *Annual Energy Outlook 2013*; U.S. Energy Information Administration: 2013.
145. Moniz, E. J.; Jacoby, H. D.; Meggs, A. J. M. *The Future of Natural Gas*; MIT: 2011.
146. Kearns, J.; Armstrong, K.; Shirvill, L.; Garland, E.; Simon, C.; Monopolis, J. *Flaring & Venting in the Oil & Gas Exploration & Production Industry*; International Association of Oil & Gas Producers: 2000.
147. Trench, C., J.; Miesner, T. O. *The Role of Energy Pipelines and Research in the United States*; Pipeline Research Council International, Inc.: 2006.
148. Wilhelm, D. J.; Simbeck, D. R.; Karp, A. D.; Dickenson, R. L., Syngas Production for Gas-to-Liquids Applications: Technologies, Issues and Outlook. *Fuel Processing Technology* **2001,** *71* (1–3), 139-148.
149. *World Lng Report*; International Gas Union: 2013.
150. Thomas, S.; Dawe, R. A., Review of Ways to Transport Natural Gas Energy from Countries Which Do Not Need the Gas for Domestic Use. *Energy* **2003,** *28* (14), 1461-1477.
151. Arab, J.; Amiri, M. J.; Hosseinabadi, A.; Torabi, A. *Natural Gas Vehicle Cylinder Safety and Inspection Requirements*; NGV Global: 2010.
152. Menon, V. C.; Komarneni, S., Porous Adsorbents for Vehicular Natural Gas Storage: A Review. *Journal of Porous Materials* **1998,** *5* (1), 43-58.
153. Xue, L.; Widera, G. E.; Sang, Z., Burst Analysis of Cylindrical Shells. *Journal of Pressure Vessel Technology* **2008,** *130* (1), 014502-014502.

154. Peng, D.-Y.; Robinson, D. B., A New Two-Constant Equation of State. *Industrial & Engineering Chemistry Fundamentals* **1976,** *15* (1), 59-64.
155. Quinn, D. F.; MacDonald, J. A.; Sosin, K. In *Mlcroporous Carbons as Adsorbents for Methane Storage*, San Diego, 1994; San Diego, pp 451-455.
156. Zhang, S.-y.; Talu, O.; Hayhurst, D. T., High-Pressure Adsorption of Methane in Nax, Mgx, Cax, Srx, and Bax. *J. Phys. Chem.* **1991,** (95), 1722-1726.
157. Allaoui, A.; Bai, S.; Cheng, H. M.; Bai, J. B., Mechanical and Electrical Properties of a Mwnt/Epoxy Composite. *Composites Science and Technology* **2002,** *62* (15), 1993-1998.
158. Tripathi, S.; Saini, P.; Gupta, D.; Choudhary, V., Electrical and Mechanical Properties of Pmma/Reduced Graphene Oxide Nanocomposites Prepared Via in Situ Polymerization. *J Mater Sci* **2013,** *48* (18), 6223-6232.
159. Lertwimolnun, W.; Vergnes, B., Influence of Compatibilizer and Processing Conditions on the Dispersion of Nanoclay in a Polypropylene Matrix. *Polymer* **2005,** *46* (10), 3462-3471.
160. Lapcik, L., Jr.; Jindrova, P.; Lapcikova, B., Effect of Talc Filler Content on Poly(Propylene) Composite Mechanical Properties. In *Engineering against Fracture*, Pantelakis, S.; Rodopoulos, C., Eds. Springer Netherlands: 2009; pp 73-80.
161. Malkina, O.; Mahfuz, H.; Sorge, K. D.; Rangari, V. K., Anisotropic Physical Properties of Sc-15 Epoxy Reinforced with Magnetic Nanofillers under Uniform Magnetic Field. *J Mater Sci* **2011,** *46* (11), 3982-3988.
162. Danev, G.; Assa, J.; Jivkov, I.; Strijkova, V.; Spassova, E., Polyimide-Matrix-Based Composite Materials. *Journal of Materials Science: Materials in Electronics* **2003,** *14* (10-12), 825-827.
163. Roy, C.; Chaala, A.; Darmstadt, H., The Vacuum Pyrolysis of Used Tires: End-Uses for Oil and Carbon Black Products. *Journal of Analytical and Applied Pyrolysis* **1999,** *51* (1–2), 201-221.
164. Hussain, F., Review Article: Polymer-Matrix Nanocomposites, Processing, Manufacturing, and Application: An Overview. *Journal of Composite Materials* **2006,** *40* (17), 1511-1575.